UNIVERSITY OF CALIFORNIA, SAN DIEGO

Force and shape coordination in amoeboid cell motility

A dissertation submitted in partial satisfaction of the
requirements for the degree
Doctor of Philosophy

in

Engineering Sciences (Engineering Physics)

by

Baldomero Alonso-Latorre

Committee in charge:

Professor Juan C. Lasheras, Chair
Professor Juan C. del Álamo, Co-Chair
Professor Richard A. Firtel, Co-Chair
Professor Shu Chien
Professor Eric Lauga
Professor Alison Marsden

2010

The dissertation of Baldomero Alonso-Latorre is approved, and it is acceptable in quality and form for publication on microfilm and electronically:

_____

_____

_____

_____
Co-Chair

_____
Co-Chair

_____
Chair

University of California, San Diego

2010

DEDICATION

To my parents, Consuelo and Ceferino, and to Vanessa.

EPIGRAPH

"As a rule, men worry more about what they can't see than about what they can."

by Gaius Julius Caesar.

TABLE OF CONTENTS

LIST OF FIGURES

LIST OF TABLES

a_k	Weight coefficient for principal component k ($\mathrm{pN}^{1/2}$ $\mu\mathrm{m}^{1/2}$)
a_b^s	Weight coefficient for principal component accounting for cell shape bending resulting from PCA on s (-)
a_0	Function for the calculation of E (-)
A_{cell}	Average cell area during the last three observations (pixels)
$A_{features}$	Area of features detected after application of threshold (pixels)
AF	Area flux ($\mu\mathrm{m}^2/\mathrm{s}$)
AF_{defor}	Area flux of deformation ($\mu\mathrm{m}^2/\mathrm{s}$)
AF_{trans}	Area flux of translocation ($\mu\mathrm{m}^2/\mathrm{s}$)
α	Wavenumber in x-direction
b	Vertical brightness field (-)
b_0	Function for the calculation of E (-)
β	Wavenumber in y-direction
c	Auxiliary function to transform p into s (-)
CPC	Canonical principal component
DIC	Differential interference contrast microscopy
d	Characteristic width of PSF (μm)
$d\widehat{\mathbf{u}}_{\alpha\beta}$	Derivative in z of $\widehat{\mathbf{u}}_{\alpha\beta}$ (-)
δ	Characteristic width of the location of fluorescent beads (μm)
δz	Indentation depth of tungsten carbide sphere (μm)
Δ	Spatial resolution of measured displacement field (μm)
Δz	Vertical separation between focal planes (μm)
ECM	Extracellular matrix
E	Young's modulus of the substrate (Pa)
E_0	Leading order of E (Pa)
E_1	Young's modulus of top substrate (Pa)
E_2	Young's modulus of bottom substrate (Pa)
E_r	Ratio of Young's moduli E_2/E_1 (-)
ϵ	Perturbation parameter or small positive parameter (-)
$\bar{\epsilon}$	Strain tensor (-)
η	Horizontal coordinate in cell-based reference frame (-)
k_{22}	Principal component above which t_{R0} becomes lower than 22 s (-)

f	Perturbation function (-)
$\mathbf{F}_{net}$	Net force exerted by the cell on the substrate (pN)
$\mathbf{F}_b$	Pole force at the back of the cell (pN)
$\mathbf{F}_f$	Pole force at the front of the cell (pN)
F_P	Average magnitude of the pole forces (pN)
F_R	Average magnitude of the force exerted by the cell (pN)
$\mathcal{F}$	Two dimensional Fourier transform
GFP	Green fluorescent protein
γ	Threshold for determination of the stages of the motility cycle
h	Substrate thickness (µm)
h_0	Vertical location of fluorescent beads plane (µm)
h_1	Thickness of top substrate (µm)
h_2	Thickness of bottom substrate (µm)
H	Polynomial fit to the histogram of I_0 (-)
I_{DIC}	Intensity field of DIC image (-)
I_{ave}	Averaged intensity field of all DIC images in experiment (-)
I_0	Intensity field after removal of static imperfections (-)
I_{max}	Intensity for maximum of I_0 (-)
I_1	Inferior limit of the intensity region to determine threshold I_{thr} (-)
I_2	Superior limit of the intensity region to determine threshold I_{thr} (-)
I_{thr}	Threshold intensity for cell segmentation (-)
L	Cell length (µm)
L_B	Length and width of box enclosing the cell for computation of traction stresses (µm)
L_x	Length of the computational box for the analytical durotaxis assay (µm)
L_{max}	Local maximum of cell length (µm)
L_{min}	Local minimum of cell length (µm)
λ	Step length of the motility cycle (µm)
λ_k	Principal value of component k or average contribution of principal component k to U_S (pN µm)
Λ	Parameter for the calculation of E (-)
$mlcE^-$	Essential light chain null
$mhcA^-$	Heavy chain null
MyoII	Protein myosin II

N	Number of cells (-)
N_B	Vertical distribution of fluorescent beads (-)
ν	Relative contribution of principal component k to U_S (-)
PCA	Principal component analysis
PSF	Point spread function (-)
p	p-value (-)
p	Function describing cell shape (-)
pav	Average p (-)
$Phase$	Stage of the motility cycle (-)
ϕ	Angle between cell longitudinal axis and x-axis of laboratory reference frame (rad)
$\boldsymbol{\psi}$	Principal function or component of composite function $\mathbf{w}$ (-)
$\boldsymbol{\varphi}$	Principal function or component of $\boldsymbol{\theta}$ (-)
$\widehat{\boldsymbol{\varphi}}_{\alpha\beta}$	Fourier coefficients of $\boldsymbol{\varphi}$ (-)
$Q_{\alpha\beta}$	Lower-triangular matrix for Cholesky decomposition of $A_{\alpha\beta}$ ($\mathrm{Pa}^{1/2}$ $\mu\mathrm{m}^{-1/2}$)
r_{f-g}	Correlation coefficient between arbitrary functions f and g (-)
R	Radius of tungsten carbide sphere (µm)
R_T	Frobenius norm of the transfer function between $\widehat{\mathbf{u}}_{\alpha\alpha}/E$ and $\widehat{\boldsymbol{\tau}}_{\alpha\alpha}$ ($\mu\mathrm{m}^{-1}$)
R_f	Auto-correlation function of arbitrary function f (-)
R_{f-g}	Cross-correlation function between arbitrary functions f and g (-)
s	Continuous function describing cell shape (-)
S_0	Size of first structuring element (pixels)
S_1	Size of second structuring element (pixels)
σ	Poisson's ratio (-)
σ_1	Poisson's ratio of the top substrate (-)
σ_2	Poisson's ratio of the bottom substrate (-)
t	Time (s)
$talA^-$	Talin A null
t_{min}	Instant of time associated with the nearest local maximum in cell length (s)
t_{max}	Instant of time associated with the nearest local minimum in cell length (s)
t_{R0}	Estimated time for loss of temporal correlation in $a_k(t)$
T	Period of the motility cycle (s)
T_i	Duration of phase i of the motility cycle (s)
$T_{\alpha\beta}$	Transfer function between $\widehat{\mathbf{u}}_{\alpha\beta}$ and $\widehat{\boldsymbol{\tau}}_{\alpha\beta}$ (Pa/µm)

$\bar{\tau}$	Stress tensor (Pa)
τ_{ik}	Stress tensor (Einstein's notation) (Pa)
$\boldsymbol{\tau}$	Stress vector field at substrate free surface (τ_{zx},τ_{zy},τ_{zz}) (Pa)
$\widehat{\boldsymbol{\tau}}_{\alpha\beta}$	Fourier coefficients of $\boldsymbol{\tau}$ (Pa)
$\boldsymbol{\theta}$	Strain energy-square root (pN$^{1/2}$ µm$^{1/2}$)
$\widehat{\boldsymbol{\theta}}_{\alpha\beta}$	Fourier coefficients of the strain energy-square root (pN$^{1/2}$ µm$^{1/2}$)
u	Horizontal displacement in the x-direction (µm)
$\mathbf{u}$	Displacement vector field (µm)
u_{ik}	Strain tensor (Einstein's notation) (-)
$\widehat{u}_{\alpha\beta}$	Fourier coefficients of u (µm)
$\widehat{\mathbf{u}}_{\alpha\beta}$	Fourier coefficients of $\mathbf{u}$ (µm)
U_S	Strain energy exerted on the substrate (pN µm)
U_S^k	Strain energy exerted on the substrate with principal component k (pN µm)
v	Horizontal displacement in the y-direction (µm)
$\widehat{v}_{\alpha\beta}$	Fourier coefficients of v (µm)
V	Cell centroid velocity (µm/s)
w	Vertical displacement (µm)
$\mathbf{w}$	Composite function of both $\boldsymbol{\theta}$ (pN$^{1/2}$ µm$^{1/2}$) and s (-)
W	Apparent weight of tungsten carbide sphere used (µm)
WT	Wild type
x	Horizontal coordinate parallel to the substrate free surface in laboratory reference frame (µm)
x_c	x-coordinate of cell centroid (µm)
ξ	Horizontal coordinate in cell-based reference frame (-)
χ	Principal function or component associated to $\boldsymbol{\varphi}$ (-)
$\boldsymbol{\Xi}$	Traction force equivalent to $\boldsymbol{\varphi}$ (pN)
y	Horizontal coordinate parallel to the substrate free surface in laboratory reference frame (µm)
y_c	y-coordinate of cell centroid (µm)
z	Vertical coordinate perpendicular to the substrate free surface (µm)
z_1	Vertical location of measurement plane (µm)

ACKNOWLEDGEMENTS

This once-in-a-life-time opportunity would have not been possible without the impulse from my mentors in Universidad Carlos III de Madrid. I specially thank Professor Antonio L. Sánchez, who at the end of my college education in Spain opened the gates of science for me without reservations.

Thanks to Professor Juan C. Lasheras for the support and confidence that he deposited in me when he gave me the opportunity to join his research group at UCSD. Professor Lasheras is as well responsible for the turn in my career direction from classical fluid mechanics to biophysics, cell mechanics in particular, a research area which by the time I started my graduate work was merely a stem of the flourishing garden it currently is at Professor Lasheras' group. Most specially, I would like to express my gratitude to Juan not only for his wise professional guidance, but for his personal support, so important at crucial times.

Thanks to Professor Juan C. del Álamo, with whom I have had the fortune to work during an important part of my period at UCSD. I have constantly learnt, and keep learning, from his rigorous, talented, and ambitious scientific spirit. It has been my pleasure not only to work with Juanca, but to develop a friendship through good and bad times which I am sure we will continue nurturing in the future.

Thanks to Professor Javier Rodriguez-Rodriguez, an extremely talented scientist with whom I collaborated during my first year in graduate school in the project which would eventually develop into my thesis, sharing unforgettable moments, both at the lab and out of it.

This adventure at the frontier between engineering and biology would not have been possible without Professor Richard A. Firtel and Dr. Ruedi Meili in the Section of Cell and Developmental Biology at UCSD. The collaboration between Professors Lasheras and Firtel laid the foundations of this dissertation, and the work of Dr. Meili was fundamental to consolidate it. This multidisciplinary environment has been in itself paramount in my education as a graduate student, since it has taught me how vital for the success of such a collaboration is the establishment of a bridge, of a common ground between disciplines.

Thanks to Professor Gaudenz Danuser, initially a member of my thesis committee, although eventually logistical problems precluded him from attending my PhD defense. He offered me honest counsel at times when I needed it. Our discussions have always been an absolute pleasure, his insightful advice always so clear and helpful.

From purely the personal side, many people have my gratitude. I am really glad to say that they are far too numerous, and that naming all of them would require an additional chapter in this dissertation. The years in San Diego have given me the chance to develop friendships with people of very different origins and cultures, something which has tremendously enriched this period and have made it a absolutely life-changing experience. I felt really welcome since the day I landed, and it was extremely easy to feel in family, a family who cared for me at difficult times, for which I will always be grateful. When time has come all I have tried is to deliver back to all the newcomers the same kind of treatment, the same friendship that I was offered upon my arrival. I hope to have done this right, and to have created such a strong bond with them as the one I had with those who received me. I would like to mention in particular one person, Javier Urzay Lobo, fellow graduate student and true friend with whom I had the luck to share almost everything during these handful of years so important in our personal development. I am truly glad to have his friendship, which I ambition to maintain forever.

Everything that I am I owe it to my parents. I grew up according to their values: effort, responsibility, honesty, kindness. I cannot think of better parents anybody could have, and I profoundly thank them for having pushed so hard in every aspect, demanding excellence in every step, trying to make the best out of me. Every day I struggle for you to be proud. I am your son, and thus I am you. Therefore, this is your work as well, and to you is dedicated.

And finally, thank you, Vanessa, my light, my heart, my soul, my reason. Thank you for your constant and unconditional support, for your patience in the distance, for your faith, for your stubborness. Thank you for being the way you are, the way I could not conceive anybody could be before I met you. For all of that and for much more, because you are part of me and because I love you, I dedicate my work to you.

La Jolla, California. November 1, 2010.

Chapters 2 and 3, in part, have been published in the *Proceedings of the National Academy of Sciences of the United States of America*, "Spatio-temporal analysis of eukaryotic cell motility by improved force cytometry," by J. C. del Álamo, R. Meili, B. Alonso-Latorre, J. Rodriguez-Rodriguez, A. Aliseda, R. A. Firtel, and J. C. Lasheras (2007) 104:13343-13348, and in the *Conference Proceedings of the IEEE Engineering in Medicine and Biology Society*, "Distribution of traction forces associated with shape changes during amoeboid cell migration," by B. Alonso-Latorre, R. Meili, E. Bastounis, J. C. del Álamo, R. A. Firtel, and J. C. Lasheras (2009) 2009:3346-3349. The thesis author is a co-author in the first publication and the primary investigator in the last publication.

Chapter 3, in part, have been published in *Molecular Biology of the Cell*, "Myosin II is essential for the spatiotemporal organization of traction forces during cell motility," by R. Meili, B. Alonso-Latorre, J. C. del Álamo, R. A. Firtel, J. C. and Lasheras (2010) 21:405-417, and has been accepted for publication in the *International Journal of Transport Phenomena*, "Distribution of traction forces and intracellular markers associated with shape changes during amoeboid cell migration," by J. C. Lasheras, B. Alonso-Latorre, R. Meili, E. Bastounis, J. C. del Álamo, and R. A. Firtel (2010). The thesis author is the primary investigator in these publications.

Chapter 4, in part, have been submitted for publication in the *Biophysical Journal*, "An oscillatory contractile pole-force mode dominates the traction forces exerted by migrating amoeboid cells," by B. Alonso-Latorre, J. C. del Álamo, R. Meili, R. A. Firtel, and J. C. Lasheras (2010). The thesis author is the primary investigator in this publication.

Chapter 2, in part, is in preparation for submission for publication, "Three-dimensional traction cytometry in amoeboid cells," by J. C. del Álamo, R. Meili, B. Alonso-Latorre, B. Álvarez, R. A. Firtel, and J. C. Lasheras (2011). The thesis author is a co-author in this publication.

Chapters 2 and 5, in part, are currently in preparation for submission for publication, "Advanced Fourier traction cytometry techniques for mechanotransduction studies," by B. Alonso-Latorre, J. C. del Álamo, R. Meili, R. A. Firtel, and J. C. Lasheras (2011). The thesis author is the primary investigator in this publication.

Experiments were performed by Dr. R. Meili in the Section of Cell and Developmental Biology, University of California, San Diego. This investigation was partially funded by the U.S. National Institutes of Health.

VITA

September, 2003	Ingeniero Superior Industrial, Departmento de Ingeniería Térmica y de Fluidos, Universidad Carlos III de Madrid, Spain.
2003	VKI Award (9-month Pre-doctoral Training Grant) awarded by the von Karman Institute for Fluid Dynamics, Rhode-St-Genèse, Belgium.
June, 2004	Research Master in Fluid Dynamics (former "Diploma Course", equivalent to Master of Science), Department of Environmental and Applied Fluid Dynamics, von Karman Institute for Fluid Dynamics, Rhode-St-Genèse, Belgium.
2004-2005	Teaching Assistant, Departmento de Ingeniería Térmica y de Fluidos, Universidad Carlos III de Madrid, Spain.
2005-2007	Teaching Assistant, Department of Mechanical and Aerospace Engineering, University of California San Diego, USA.
2005-2010	Graduate Research Assistant, Department of Mechanical and Aerospace Engineering, University of California San Diego, USA.
June, 2008	Master of Science in Aerospace Engineering, Department of Mechanical and Aerospace Engineering, University of California San Diego, USA.
March, 2009	Student Research Achievement Award in the Category of Cell Motility, 53^{rd} Annual Meeting of the Biophysical Society, Boston, MA, USA.
June, 2009	Award to the Outstanding Graduate Student, Department of Mechanical and Aerospace Engineering, University of California San Diego, USA.
December, 2010	Doctor of Philosophy in Engineering Physics, Department of Mechanical and Aerospace Engineering, University of California San Diego, USA.

PUBLICATIONS

del Álamo J. C., Meili R., **Alonso-Latorre B.**, Rodriguez-Rodriguez J., Aliseda A., Firtel R. A., and Lasheras J. C., 2007. "Spatio-temporal analysis of eukaryotic cell motility by improved force cytometry," *Proc. Natl. Acad. Sci. U.S.A.*, 104:13343-13348.

Alonso-Latorre B., Meili R., Bastounis E., del Álamo J. C., Firtel R. A., and Lasheras J. C., 2009. "Distribution of traction forces associated with shape changes during amoeboid cell migration," *Conf. Proc. IEEE Eng. Med. Biol. Soc.*, 2009:3346-3349.

Meili R.†, **Alonso-Latorre B.**†, del Álamo J. C., Firtel R. A., and Lasheras J. C., 2010. "Myosin II is essential for the spatiotemporal organization of traction forces during cell motility," *Molecular Biology of the Cell*, 21:405-417. †Co-first authors.

Lasheras J. C., **Alonso-Latorre B.**, Meili R., Bastounis, E., del Álamo J. C., and Firtel R. A., 2010. "Distribution of traction forces and intracellular markers associated with shape changes during amoeboid cell migration," *International Journal of Transport Phenomena*, (In Press).

Alonso-Latorre B., del Álamo J. C., Meili R., Firtel R. A., and Lasheras J. C., 2010. "An oscillatory contractile pole-force mode dominates the traction forces exerted by migrating amoeboid cells," *Biophysical Journal*, (Submitted).

Alonso-Latorre B., del Álamo J. C., Meili R., Firtel R. A. and Lasheras J. C., 2011. "Advanced Fourier traction cytometry techniques for mechanotransduction studies," (In Preparation).

del Álamo J. C., Meili R., **Alonso-Latorre B.**, Álvarez B., Firtel R. A., and Lasheras J. C., 2011. "Three-dimensional traction cytometry in amoeboid cells," (In Preparation).

INVITED SEMINARS

Alonso-Latorre B., "Protein Myosin-II is essential for the spatiotemporal organization of traction forces during cell motility," Division of Epithelial Biomedicine, Department of Basic Science, CIEMAT (National Center for Energetic, Environmental and Technological Research), Madrid, Spain, July 2, 2010.

Alonso-Latorre B., "The mechanics of the motility cycle of amoeboid cells," Division of Biological Soft Matter, Department of Biomolecular Systems, FOM Institute AMOLF (Foundation for Fundamental Research on Matter, Institute for Atomic and Molecular Physics), Amsterdam, The Netherlands, October 12, 2010.

Alonso-Latorre B., "Force and shape in amoeboid cell migration," Department of Physical Chemistry, Institute Curie, Paris, France, October 14, 2010.

Alonso-Latorre B., "The mechanics of amoeboid motility over surfaces," Section of Cardiovascular Cellular Engineering, Hydrodynamics Laboratory (LadHyX), École Polytechnique, Palaiseau, France, October 15, 2010.

FIELDS OF STUDY

Major Field: **Engineering Physics**

Studies in Biomechanics
Professors Gaudenz Danuser, Geert W. Schmid-Schönbein and Juan C. Lasheras.

Studies in Medical Imaging
Professor Thomas Liu.

Studies in Microscopy Techniques
Professors Mark Ellisman, Maryann E. Martone, James Bouwer and Gina E. Sosinsky.

Studies in Fluid Mechanics
Professor Forman A. Williams, Stefan G. Llewellyn Smith and Sutanu Sarkar.

Studies in Environmental Fluid Dynamics
Professor Laurence Armi.

Studies in Gas Dynamics
Professors Forman A. Williams and Yousef M. Bahadori.

Studies in Applied Mathematics
Professors Glenn Ierley, William R. Young and Daniel Tartakovsky.

ABSTRACT OF THE DISSERTATION

Force and shape coordination in amoeboid cell motility

by

Baldomero Alonso-Latorre

Doctor of Philosophy in Engineering Sciences (Engineering Physics)

University of California, San Diego, 2010

Professor Juan C. Lasheras, Chair
Professor Juan C. del Álamo, Co-Chair
Professor Richard A. Firtel, Co-Chair

Cell motility plays an essential role in many physiological and pathological processes, yet we still lack information about the spatio-temporal coordination between regulatory biochemical processes and mechanics of cell migration. This dissertation has investigated the mechanics of amoeboid cell migration through intensive analysis of the traction forces exerted and shapes adopted by single *Dictyostelium discoideum* cells migrating chemotactically, focusing on wild-type (WT) and contractility-defective cells lacking either protein myosin II ($mhcA^-$) or the myosin II essential light chains ($mlcE^-$).

We have developed an improved traction force cytometry method to calculate cell traction stresses which considers the finite thickness of the substrate. We have shown that the strain energy exerted by locomoting cells on the substrate evolves quasi-periodically and correlates with cell length, and thus it can be used as a quantitative indicator of the cell motility cycle. The periodicity (T) of the oscillations in the traction forces correlates strongly with the average velocity of migration (V) of cells according to the hyperbolic law $V\,T{=}\lambda$, where the constant λ is independent of the strain analyzed and corresponds to the average distance a cell travels per cycle.

Given the quasi-periodic character of both cell length and strain energy, we have performed a phase statistical analysis to obtain a spatio-temporal representation of the canonical motility cycle divided into four phases: protrusion, contraction, retraction, and

relaxation. This analysis has elucidated the role that protein myosin II plays in enhancing the kinetics of the four stages of the cycle and in controlling the spatial distribution of the traction forces regulating that process.

We have used principal component analysis to dissect the mechanics of locomotion of amoeboid cells into a reduced set of dominant components of cellular traction forces and shape changes. The dominant traction force component accounts for 40% of the strain energy performed by these cells, and its temporal evolution correlates with the quasi-periodic variations of cell length and strain energy exerted on the substrate.

Finally, we have developed two analytic assays for the calculation of cell traction stresses in configurations of interest to further understand the mechanosensing machinery of cells.

Chapter 1

Introduction

Cell migration is central to many physiological processes, including wound healing, immune response, or embryonic development [1–4]. Wound healing and the response of the immune system comprises a series of stages, including platelet activation, vasodilatation, and a clotting cascade leading to the formation of a fibrin and fibronectin plug, across which neutrophils, macrophages, fibroblasts, and epidermal cells migrate to complete the healing of a tissue [5]. During embryonic development, layers of cells migrate to establish the foundations of tissues and organs [6]. These developmental processes take place throughout our whole life, with different types of cells being renewed on a daily basis.

Likewise, the deregulation of cell migration contributes very importantly to serious pathological processes, such as tumor invasion, vascular diseases, or mental retardation [7–9]. The invasion and metastasis of tumor cells entails a complicated array of biochemical processes tightly coupled with changes in the cell cytoskeletal structure which eventually lead to migration of cancer cells from their primary site, reaching the blood or lymph vessels, and metastasizing in distant organ sites [10]. Vascular diseases, such as atherosclerosis, derive from the formation of lesions in the endothelium, which leads to the accumulation over time of fats, cholesterol, platelets, cellular debris and calcium in the artery wall. As the lesion continues developing, chemoattractant signals trigger the migration of smooth muscle cells into the intima, contributing to the stiffening of the vascular vessels [11]. In the case of mental retardation, it may arise as the result of defective motion and establishment of projections to form synapses by neuronal cells during brain development [12]. As these examples depict, many of the harmful effects derive from subtle misregulation of motility rather than from its outright absence. Quantitative characterization of these deficiencies may help to improve treatment of such conditions through precise targeting of

cellular motility. Furthermore, understanding and controlling cell migration is important for tissue engineering, a discipline which requires a detailed understanding of cell-matrix interactions, which are fundamental for attachment, growth, proliferation, and, very importantly, migration of cell cultures, a key component in the development of tissue constructs [3, 5].

Cell locomotion has been extensively studied using the shape of the cell as readout, a challenging task, given that cells are plastic and dynamic objects. Wessels and Soll [13–21] developed a framework for the 2D and 3D analysis of morphological changes during cell locomotion, which enabled them to track the motion of amoeboid cells [1] through the observation of the time evolution of descriptors such as the length of the cell or the velocity of the centroid of the cell. An additional problem is the substantial level of variability in the properties of individual cells [22]. A common way to ameliorate this problem is to select a limited number of cells that can represent the population. However, the identification of such "prototypical" cells is subjective and is often lacking statistical validation. A few different groups have developed techniques to face this inherent condition of cell motility, such as the work by Machacek and Danuser [23], which identified different protrusion phenotypes using level set methods, or the works by Killich et al. [24] and Keren et al. [22], which used Principal Component Analysis (PCA) (also known as Karhunen-Loève decomposition or Proper Orthogonal Decomposition) to quantify cell shape changes of migrating *Dictyostelium discoideum* cells and epithelial fish keratocytes respectively.

The quantification of the traction stresses is essential to the better understanding of how the cell regulates adhesion, morphology and migration. However, because of experimental complexity, there are still important open questions regarding the mechanical actions of migrating cells on the extracellular matrix (ECM). The development of a variety of traction force cytometry techniques in the last 20-30 years is being one of the keys to answer those questions. Harris et al. [25] first identified qualitatively the nature of the stresses exerted by cells on the ECM through the observation of the wrinkling patterns cells induced over a thin layer of silicone rubber substratum. Other approaches contemplate the use of a substrate seeded with micropillars, where the force applied to each one is directly proportional to the displacement of its tip [26, 27]. Dembo et al. [28] and Peterson [29] first described the use of thick elastic substrates to calculate the traction stresses exerted by cells attached to the surface, to be obtained from measurements of the displacement field induced in the substrate. For the calculation of the traction stresses Dembo et al. [28] and

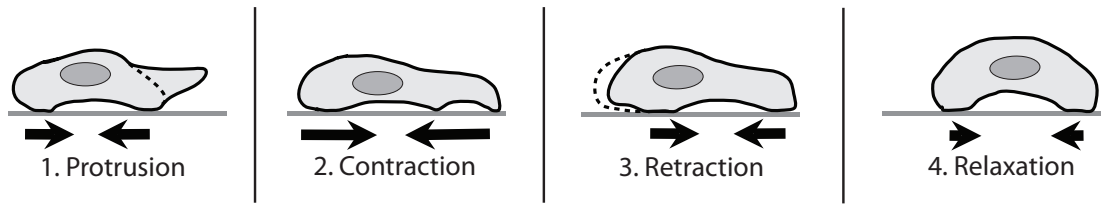

Figure 1.1: Sketch of the different stages of the amoeboid motility cycle. (1) Protrusion: through actin polymerization in the cell leading edge, and formation of new attachments; (2) Contraction: increase in the contractile forces exerted by the cell on the substrate; (3) Retraction: the cell releases or breaks the attachments at its posterior part and retracts through myosin-mediated actin filament contraction; (4) Relaxation: stage prior to the beginning of a new motility cycle.

Peterson [29] used a boundary element method which expressed the classical solution of the equation of static equilibrium for a homogeneous, semi-infinite medium found by Boussinesq [30], involving the inversion of a large system of equations in real space, and thus proving computationally very expensive. Using a similar experimental configuration, Schwarz et al. [31] developed an approach consisting in the reconstruction of the traction forces from the application of discrete point forces, which in turn requires experimental knowledge of the location of the adhesion sites, to be obtained from fluorescence data on proteins localizing to focal adhesions (e.g., vinculin or paxillin) [27, 31] or by reflection interference contrast microscopy [32]. Butler et al. [33] developed Fourier traction force cytometry, which took advantage of the fact that the inversion of Boussinesq's solution is trivial in Fourier space, thus greatly accelerating the calculation of the traction stresses, and allowing to analyze long recordings of the traction forces exerted by migrating cells. Traction force cytometry techniques using deformable substrates have been applied to study the traction stresses exerted by many types of cells, including locomoting keratocytes [28], fibroblasts [29] and *Dictyostelium discoideum* [34–36].

Cell migration over surfaces requires the orchestrated integration of transient signalling events and changes in cytoskeletal structure and its mechanical interaction with the substrate through adhesion regions [4]. Amoeboid motility is a prototypic model of it, which has been most extensively studied in lymphocytes [37, 38], and *Dictyostelium* [39–43]. *Dictyostelium* is a valuable model system for the investigation of cell motility with extensive similarities to higher eukaryotes, in particular to leukocytes [44]. Despite the complexity of the various chemical, biological, and mechanical processes involved in eukaryotic cell motility, it has been suggested that cells perform a limited repertoire of motions during their

migration: protrusion of the leading edge, formation of new adhesions near the front, cell contraction, and release or breakage of the rear adhesions [1] (see Fig 1.1). The exact nature and sequence of events making possible this motility cycle are not fully understood yet.

The establishment of inherent polarity of motile cells has been studied extensively. Upon encountering chemotactic molecules, cells reorganize into a "front", which promotes forward motion, and a "back", which promotes the retraction of the cell body. This polarity comprises the distribution of structural proteins as well as concentration gradients of activated intermediary signaling molecules such as PI3K, Ras, Rho, or Rac [4], which control various cytoskeletal elements. One less clear aspect is how the initial cellular polarity is generated from weak external or internal cues, and subsequently maintained and coordinated on the cellular level. Similarly, we lack reliable information about the changes in the physical properties of the cell that result from this coordinated regulation. Further understanding requires accurate measurements of these properties as the cell moves and interacts with the substrate under controlled conditions. This requirement is especially challenging in the case of *Dictyostelium* cells because their relatively small size and fast migration speeds demand high temporal and spatial resolutions.

After the polarity of the cell is established, cell migration is driven by the coordination between the protrusion of the cell front and the retraction of the cell back, which can basically be conceptualized as the balance between the turnover of filamentous actin (F-actin) at the front of the cell and the contractile activity of the F-actin-directed motor protein myosin II (MyoII) at the back [45–47]. The actin cytoskeleton is the basic machinery necessary for protrusion. Actin filaments (Fig. 1.2a) are polarized structures made out of actin monomers, presenting a fast-growing "barbed" (plus) end and a slow-growing "pointed" (minus) end, thus providing the basic drive for protrusion. Actin filaments can basically form filopodia, thin parallel bundles of actin filaments actin as sensors to explore the surrounding environment [48], or lamellipodia, broad dendritic structures providing the basis for cell protrusion and movement [49, 50]. In lamellipodia, actin filaments form a branched network which pushes the membrane forward. The Arp2/3 complex induces the nucleation of new actin filaments from the sides of pre-existing ones, and is the origin for the broad growth of the whole lamellipodia structure [51]. Arp2/3 complex is itself activated by Wasp/Wave molecules, upstream receivers of Cdc42 and Rac [52, 53]. Actin filament length is regulated by capping proteins, and the mechanical properties of F-actin are modulated by actin binding and cross-linking proteins [2, 54, 55], among them MyoII.

In order to achieve advancement, protrusions need to attach and stabilize to a

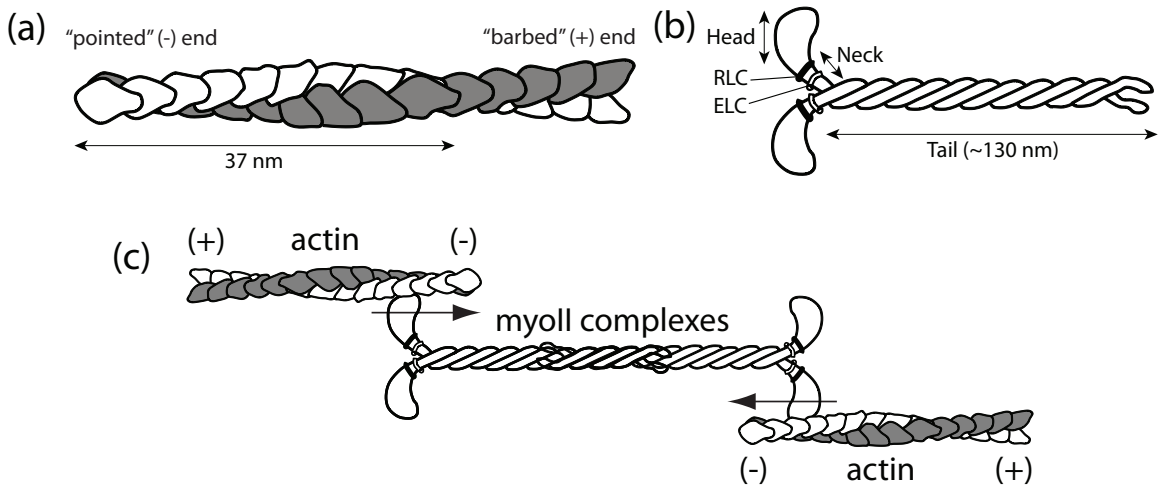

Figure 1.2: (a) Structure of an actin filament. It is composed of two helical coils of actin monomers (5 nm diameter), presenting a fast-growing "barbed" (plus) end and a slow-growing "pointed" (minus) end. (b) Structure of protein myosin II. It includes two tail domains formed by two α-helical coiled coils, ending in two globular motor domains (heads). Two light chains, essential (ELC) and regulatory (RLC), wrap around the neck of each myosin II heavy chain, and contribute to the regulation of the motor activity of protein myosin II. (c) Bipolar complexes of myosin II form by interaction of antiparallel coiled coil tail domains. The head domains attach to actin filaments, interconnecting them. The motor activity of myosin II derives from hydrolysis of ATP, leading to the rotation of the myosin heads, and thus sliding actin filaments with respect to each other.

certain degree in order to allow to pull the back of the cell forward through the contractile activity of MyoII. The interaction of the cell with the substrate is achieved through integrins in mammalian cells [56, 57], or integrin-like proteins in *Dictyostelium* [58], which enable and mediate the cell to adhere to the substrate surface. This integrins (or integrin-like-proteins in *Dictyostelium*) link to the actin cytoskeleton via intermediate proteins, such as talin, vinculin, and kinases, acting as traction sites and mechanosensors [59–61]. The specific mechanism by which this mechanosensing function takes place is still unclear and is currently being studied intensively [62, 63]. An effective turnover of the adhesions is needed for effective migration, requiring the stabilization of adhesions at the front and the break or disassembly of adhesions at the back. The specific mechanisms by which this adhesion assembly/disassembly take place, as well as its mechanosensing function, are still poorly understood. However, it is clear that they require a precise spatio-temporal regulation [59, 64].

The cycle is closed with the disassembly or break of adhesions at the back of the cell and its retraction, leading to cell translocation. MyoII (Fig. 1.2b) plays as well a crucial

role in retraction, since its contractile motor activity leads to the development of tension between adhesion sites prior to its disassembly. The MyoII complex contains two heavy chains (MhcA) [65], two regulatory light chains (MlcR) [66], and two essential light chains (MlcE) [67–69]. MyoII motor activity is regulated by phosphorylation of the regulatory light chain [70] and requires the essential light chain [71, 72]. The MyoII complexes can assemble into antiparallel bundles with motor head groups at both ends. These bipolar filaments bind and crosslink actin filaments (Fig. 1.2c) to form a cortical meshwork that increases in density from the front to the rear of the cell [73]. This cytoskeletal structure is important for the mechanical stiffness of the cell (cortical tension) [74] and can also generate the contractile forces required for efficient cell motility [14, 75]. In addition to motors, translocation requires cell-substrate adhesions to transmit traction forces to the substrate [76, 77].

In migrating wild-type (*WT*) *Dictyostelium* amoebae, both the substrate contact area and the traction forces are coupled to the specific phase of the migration cycle [34, 35, 78, 79]. This dissertation as well as other works have shown that the traction forces have a defined spatial organization, with a region of rearward directed stresses near the front and a region with forward directed stresses near the back [35, 47, 79, 80]. The proper spatiotemporal coordination of traction forces is likely an important determinant of migration speed, as previously suggested [34, 81] and also supported by the results in this dissertation. The magnitude of the traction forces is important for motility on highly adhesive substrates and in environments in which cells are unable to move if they cannot develop sufficiently large contractile forces for rear detachment [75]. Thus, the mechanisms that control the spatiotemporal organization and strength of these forces play essential roles in the regulation of cell movement.

1.1 Outline of the Dissertation

In Chapter 2, we present the experimental methodology used for the experiments carried out for this Dissertation. We present an exact, computationally efficient solution of the elastostatic equation based on Fourier expansions that expresses the tractions explicitly as functions of the deformations, which supposes an further improvement over the Fourier traction force cytometry technique developed by Butler et al. [33]. This solution takes into account the finite thickness of the substrate, which increases the accuracy of the Boussinesq solution and allows for non-zero net forces. We further refine the solution by considering

the effect of the distance between the measurement plane and the surface of the substrate.

In Chapter 3, we use this improved method to study the dynamics of *WT* and mutant *Dictyostelium* cells moving up a chemoattractant gradient, showing that their migration is composed of a repetitive sequence of canonical steps. Our analysis shows that the temporal evolution of cell length and the strain energy exerted on the substrate present a quasi-periodic evolution, and that the period of the strain energy strongly correlates with the mean migration velocity of the cells, even for mutants with adhesion and contractility defects. Using a phase-average analysis of the cell migration cycle, we have compared the motility characteristics of *WT* and mutant strains with impaired MyoII function, addressing the role that both the cross-linking and motor properties of MyoII plays in each of the stages of the motility cycle.

In Chapter 4, we obtain a statistically significant characterization of the relationship between traction forces and cell morphology in migrating amoeboid cells, using PCA as primary tool. We identify 5 canonical traction force patterns or strain energy components which explain most of the mechanical work exerted on the substrate by *WT* cells. We show that the most important component, accounting for the contraction of the substrate from front and back towards the center of the cell, is responsible for the largest proportion of strain energy and its temporal evolution correlates with that of the strain energy and the length of the cell, both of them surrogate indicators of the motility cycle of the cell. We also use this technique to identify the most relevant strain energy components in two mutant strains with contractility defects.

In Chapter 5, we present two Fourier traction force cytometry assays considering experimental situations of relevance for the study of the mechanotransduction machinery of cells. The first of them considers a substrate composed of two layers of different thickness and mechanical properties. The second one considers a semi-infinite substrate with a smooth spatial gradient of Young's modulus, which can be used for the study of durotaxis.

Finally, in Chapter 6, general conclusions and specific suggestions for future work are given.

Chapter 2

Experimental Methods and Fourier Traction Force Cytometry for Finite Substrates

This chapter describes the experimental methods used in this Dissertation, which include cell culture and microscopy of *Dictyostelium* cells, cell segmentation techniques for image analysis of cell shape, and the development of a Fourier traction force cytometry technique to calculate the traction stresses exerted by cells which takes into account the effect of the finite substrate thickness, as opposed to the commonly used technique which considers an infinitely thick substrate [33]. We compare the discrepancies between the 2D version of this technique (which assumes negligible vertical stresses at the substrate free surface) and the 3D version (which requires the measurement of the vertical displacements, and in turn provides with the vertical stresses at the surface). We study as well the influence of the substrate Poisson's ratio of the substrate in the calculation of the traction stresses.

2.1 Materials and Methods

2.1.1 *Dictyostelium* culture and microscopy

Dictyostelium cells were grown under axenic conditions in HL5 growth medium in tissue culture plates. We used wild type (WT) cells (Ax3), essential light chain null cells ($mlcE^{-}$) [67], myosin II null cells ($mhcA^{-}$) [82], and talin A null cells ($talA^{-}$) (obtained from M. A. Titus, University of Minnesota, Minneapolis, MN). Aggregation competent cells

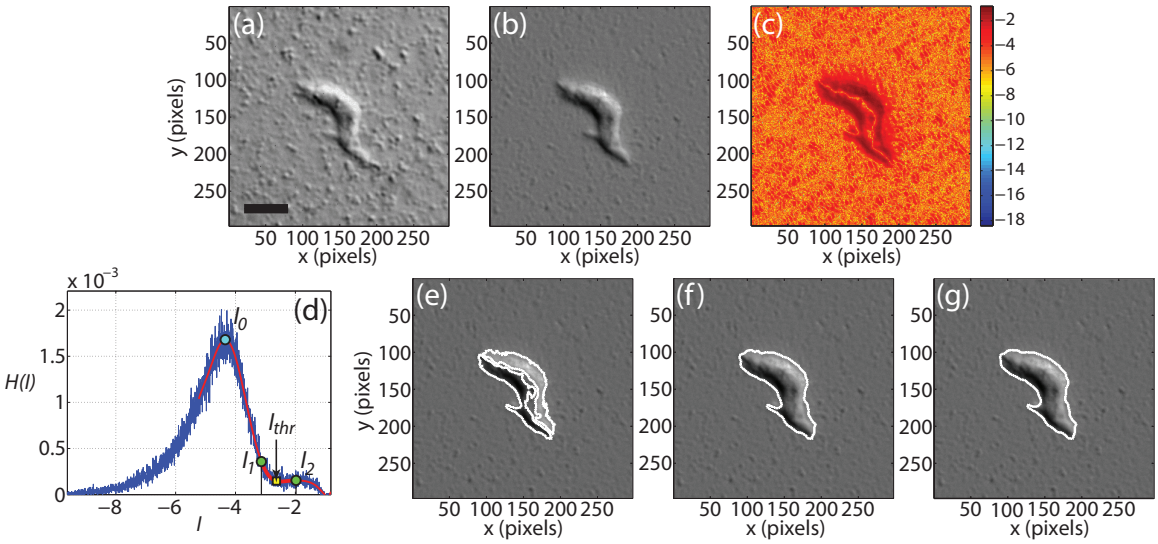

Figure 2.1: Cell shape segmentation. (a) Instantaneous DIC image of a *WT* cell. (b) Image resulting after removing static imperfections of DIC image in panel (a). (c) $I(x, y)$, natural logarithm of the absolute value of the image in panel (b). (d) Probability density function (PDF) of $I(x, y)$ (blue line); $H(I)$, polynomial fit to that PDF (red line); I_{max}, location of the global maximum of $H(I)$ (cyan dot); I_1 and I_2 (green dots) define the region of $H(I)$ whose centroid provides the instantaneous threshold I_{thr} for the detection of the cell shape (yellow square). (e) Features detected (white contours) after application to image in panel (c) of threshold I_{thr}. (f) Cell shape (white contour) resulting from application of dilation/filling/erosion with structuring element of size $S_0 = 6$ pixels to features in panel (e). (g) Detected cell shape (white contour) after application of dilation/filling/erosion with structuring element of size S_1 ($S_1 = 10$ pixels is determined applying Eq. 2.3) to features in panel (f). Scale-bar in panel (a) represents 10 µm and ≈ 60 pixels. Background image in panels (e-g) is the same as in panel (b).

were prepared by pulsing a 5×106 cells/ml suspension in Na/K phosphate buffer (9.6 mM KH_2PO_4, 2.4 mM Na_2HPO_4, pH 6.3) with cAMP to a concentration of 30 nM every 6 min for 6 h. Cells were seeded onto the gelatin substrate and allowed to adhere. A drawn glass capillary mounted on a micromanipulator served as the source of chemoattractant (150 µM cAMP in an Eppendorf femtotip, Eppendorf, Germany). For the image acquisition we used a Nikon TE300 inverted microscope with high numerical aperture lenses and a cooled CCD camera (HQ CoolSnap, Roper Scientific). The microscope was also equipped with a Z-axis drive. A PC running the Metamorph software packet controlled the entire setup including filter wheels.

2.1.2 Cell shape segmentation

Cells outlines were determined from differential interference contrast (DIC) images captured using a 40x lens at 2 s intervals for *WT*, $mlcE^{-}$ and $talA^{-}$ cells and at 4 sec intervals for $mhcA^{-}$. Image processing was performed with MATLAB (Mathworks Inc, Natick, MA). The quality of these images for cell shape segmentation was not optimal in all the cases because the image needed to be focused on the plane where the fluorescent beads were placed, which differed slightly (≈ 0.4 µm) from the free surface of the substrate. Therefore, it was necessary to develop a custom procedure to perform the cells shape segmentation. The procedure used is schematized in Fig. 2.1 and consists of the following five steps:

- Static imperfections in the original DIC image (Fig. 2.1 A) are removed

$$I_0(x,y) = \frac{I_{DIC}(x,y) - I_{ave}(x,y)}{I_{ave}(x,y) + \epsilon}, \tag{2.1}$$

  where $I_{DIC}(x,y)$ is the intensity field of the original DIC image (Fig. 2.1 A), $I_{ave}(x,y)$ is the average intensity field of all the images in the experiment, $I_0(x,y)$ is the resulting intensity field (Fig. 2.1 B), and ϵ is a very small positive number ($\epsilon = 10^{-6}$) to avoid dividing by zero.

- We then take the natural logarithm of the absolute value of $I_0(x,y)$, $I(x,y)$ (Fig. 2.1 C), and apply a threshold I_{thr} to it, extracting the meain features characterizing the cell shape. A robust value of I_{thr} providing accurate results is given by the centroid of $H(I)$, the polynomial fit to the histogram of $I(x,y)$, in the interval $[I_1, I_2]$ (Fig. 2.1 D)

$$I_{thr} = \frac{\int_{I_1}^{I_2} H(I)\, I\, dI}{\int_{I_1}^{I_2} H(I)\, dI}, \tag{2.2}$$

  where I_2 is either the intensity at which $H(I)$ reaches its local maximum with zero derivative for $I > I_{max}$ or, in its absence, the intensity at which $|dH(I)/dt|$ reaches a local minimum for $I > I_1$. I_{max} is the intensity for the absolute maximum of $H(I)$, and I_1 is the intensity at which $H(I)$ presents maximum curvature in the interval $[I_{max}, I_2^{(i-1)}]$ (where $I_2^{(i-1)}$ is the value of I_2 the previous instant of time). To ensure the smooth temporal evolution of the threshold applied, I_{thr} at each instant of time is finally chosen as the average of the ten most recent thresholds.

- The features detected after application of threshold I_{thr} (Fig. 2.1 E) are coalesced using a custom procedure of image dilation/filling/erosion with a structuring element of small size

S_0 ($S_0 = 4 - 6$ pixels $\approx 0.7 - 1$ µm $< 5\%$ of the characteristic cell size, Fig. 2.1).detected in the previous step (see Fig. 2.1 F).

- The finally determined cell shape is obtained after a second procedure of image dilation/filling/erosion is applied (Fig. 2.1 G) using a structuring element whose size S_1 is determined using the semi-empirical relationship

$$S_1(pixels) = 80 \cdot A_{cell}/A_{features} - (80 - S_0(pixels)), \tag{2.3}$$

where A_{cell} is the average area of the cell in the three previous observations, and $A_{features}$ is the area of the features obtained after the initial dilation/filling/erosion in step 3, so that the ratio $A_{cell}/A_{features}$ is typically larger than 1. The foundations for the determination of the size of the structuring element S_1 are in *percolation theory* [83], a mathematical theory which studies the behavior of connected clusters in a random graph, with applications in areas such as physics, chemistry and material science.

From the cell shape determined, centroid coordinates (x_c, y_c) and principal axes of each cell are calculated using standard MATLAB functions. Front and back of the cell are determined as the two parts in which the cell is divided by its minor axis of inertia, with the front pointing towards the direction of motion. The front can be defined as

$$\xi = [(x - x_c)cos\phi(t) + (y - y_c)sin\phi(t)][(dx_c/dt)cos\phi(t) + (dy_c/dt)sin\phi(t)] > 0, \tag{2.4}$$

where ϕ is the angle between the x axis and the cell major axis.

2.1.3 Gelatin gel fabrication

A 25 mm glass coverslip was mounted to a stainless steel ring using silicon grease (Dow Corning, Midland, Michigan). About 250 µl of a 4% solution of Nabisco Knox gelatin was added and chilled on ice for 1 h. A 1:50 dilution of a 2% carboxylate modified yellow-green latex beads with 0.1 µm diameter (Fluospheres, Molecular Probes, Eugene, Oregon) was added on top of the solidified gelatin for 15 sec. The gels were air dried for 10 min after aspiration of the beads. The gels were melted by briefly placing them on a hot plate and chilled on ice for an additional hour. Before using, they were thoroughly washed with buffer. The resulting gels were between 100 and 200 µm thick in the middle of the dish. The elastic behavior of the gelatin substrate was verified by checking in all cases that the deformation energy in any fixed region of the substrate that is crossed by a cell returns to its baseline after the cell exits the region (see Fig. 2.2).

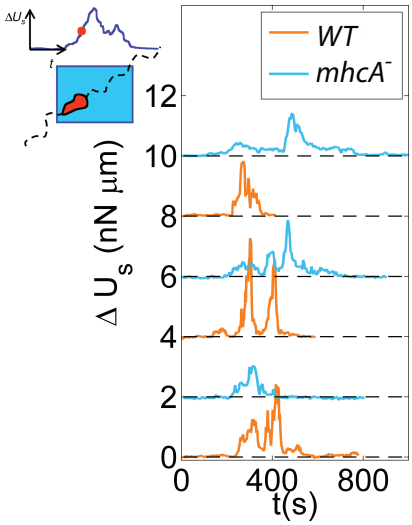

Figure 2.2: Elastic recovery of the gelatin gels used in our experiments. Each curve shows a time history of the deformation energy of in square domain of the substrate that is crossed by a cell. The initial value of the energy has been subtracted so that $\Delta U_S(t) = U_S(t) - U_S(0)$ and the baseline level is $\Delta U_S = 0$. The curves have been stacked in the Y axis with a separation of 2 nN µm between each two of them. The data come from different cells and different gel preparations. Initially, the domain is empty and the deformation energy is at its baseline. When the cell enters the domain, the deformation energy rises and it finally returns to its baseline after the cell leaves the domain.

2.1.4 Determination of horizontal substrate deformation

The substrate deformation field was obtained from the lateral displacements of 0.1-µm fluorescent latex beads embedded in the gel. The lateral displacements were determined by comparing each instantaneous image with a reference image of relaxed substrate. The comparison was performed by dividing the instantaneous and reference images into interrogation windows and computing the cross-correlation between each pair of interrogation windows. This procedure was performed using custom correlation procedures written in MATLAB (The Mathworks, Natick, MA). An ensemble average of the correlation between each image and several reference images (typically 3) increased the signal-tonoise ratio and allowed us to reduce the size of the interrogation window to 16×16 pixels (compare to the 64×64 pixels used in [33]), leading to a Nyquist spatial resolution of 1.37 µm. The average signal-to-noise ratio was ≈ 20. Fig. 2.3e shows the fluorescent marker-particles in a region containing a migrating *WT* cell and Fig. 2.3f shows the corresponding displacement field. The arrows indicate the absolute value and orientation of the displacements. The magnitude of the displacements is also mapped by the shaded contours and is typically of

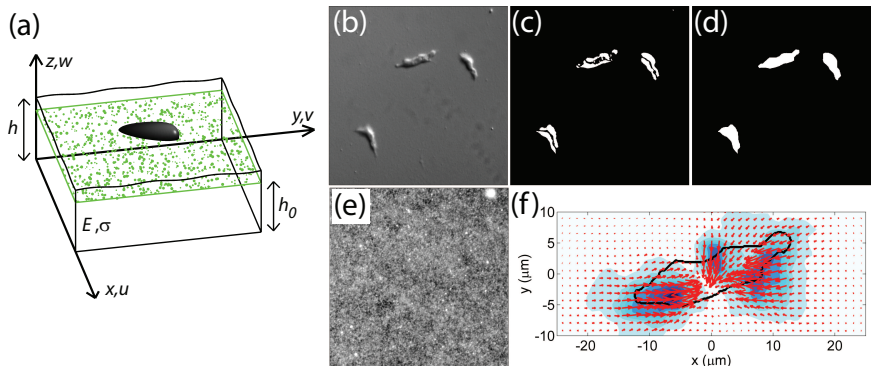

Figure 2.3: Illustration of the traction cytometry method. (a) Sketch of the experimental configuration. (b) Example of a raw DIC image used for cell contour identification. (c) The same DIC image corrected with the session average and a threshold applied to select the most intense regions. (d) Final cell contours obtained. (e) Example of a GFP image used to determine the deformation of the substrate. (f) Displacement field obtained for a crawling Dictyostelium cell. The arrows indicate the intensity and direction of the vector data. The color contours indicate their intensity.

the order of 0.1 µm.

2.1.5 Measurement of the Young's modulus of the gel

The Young's modulus was determined by measuring the static indentation depth δz of a tungsten carbide sphere ($R = 150$ µm, $W = 1.898$ µN, Hoover Precision, East Gramby, CT, USA) slowly deposited on the substrate. Dimitriadis et al. [84] found the following equation relating the Young's modulus, E, of a slab of gel of thickness h, the indentation depth δz and the radius R and apparent weight W of the sphere,

$$E = \frac{3}{4}\frac{W(1-\sigma^2)}{R^{1/2}\delta z^{3/2}}\Big[1 - \frac{2a_0}{\pi}\Lambda + \frac{4{a_0}^2}{\pi^2}\Lambda^2 - \frac{8}{\pi^3}\left({a_0}^3 + \frac{4\pi^2}{15}b_0\right)\Lambda^3 + \frac{16a_0}{\pi^4}\left({a_0}^3 + \frac{3\pi^2}{5}b_0\right)\Lambda^4\Big]^{-1} \tag{2.5}$$

where $\Lambda = \sqrt{R\,\delta z}/h$, the material Poisson ratio is assumed $\sigma = 0.3$ [85], and the constants a_0 and b_0 are functions of σ

$$a_0 = -\frac{1.2876 - 1.4678\sigma + 1.3442\sigma^2}{1-\sigma}, b_0 = \frac{0.6387 - 1.0277\sigma + 1.5164\sigma^2}{1-\sigma} \tag{2.6}$$

We determined δz as the depth where the beads displaced by the carbide sphere come into focus in a z-stack of images with a distance between focal planes of $\Delta z = 0.4$µm. The in-focus beads were detected using the SOBEL function in MATLAB. The statistical distribution of the Young's moduli of the gels in our experiments presents an average of 920 Pa and a standard deviation of 570 Pa.

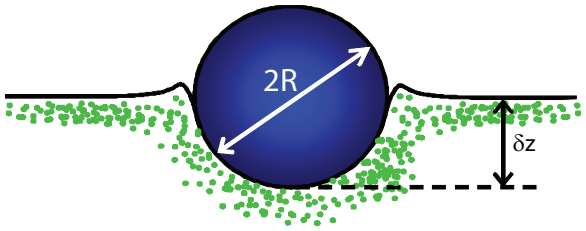

Figure 2.4: Measurement of the Young's modulus of the gel, calculated from the indentation δz of a tungsten ball of radius R in the substrate.

2.1.6 Determination of the average distance, $h-h_0$, between the displacement marker particles and the free surface of the substrate

To estimate the average distance between the substrate free surface and the layer at which the fluorescent beads are primarily located, $h-h_0$, we used z-stacks with $\Delta z = 0.4$ µm recording the cells in the DIC channel and the marker-particles in the fluorescent channel. The free surface of the gel was defined as the plane where the cell outlines have a maximum number of in-focus pixels. The average depth of the markers was determined to maximize the number of in-focus beads using the SOBEL function in MATLAB (Mathworks Inc, Natick, MA) and an interpolation procedure that yields resolutions finer than Δz. The gaps recorded in our experiments ranged from 0 to 0.4 µm. We have used the conservative value $h - h_0 = 0.4$ µm in the calculation of the forces.

Distortion of the vertical position of the marker particles due to image blurring

As we show in Figs. 2.6-2.7 (in Chapter 3), the distance between the displacement marker particles and the free surface of the substrate has an important effect on the fine-scale features of the measured traction forces. In our experiments, this distance could be easily defined by selecting the focal plane where the marker particles are imaged. However, the light generated by out-of-focus particles "leaked" into the selected focal plane and introduced uncertainties in the vertical position of the displacement markers. Hence, the focal plane had to be selected carefully to avoid systematic errors in the vertical position of the marker particles. Fig. 2.5a sketches this phenomenon. The intensity of a spherical marker in an xz image obtained with a Z-stack is more similar to a "blurred hourglass" than to an ideal circle. The blurring of the imaged marker particles leads to an apparent profile of particles (red line in Fig. 2.5a) much more spread than their actual distribution (blue line in Fig. 2.5a). This effect can be represented mathematically as the convolution of the ideal image with the point-spread function (PSF) of the marker particles [86]. Here,

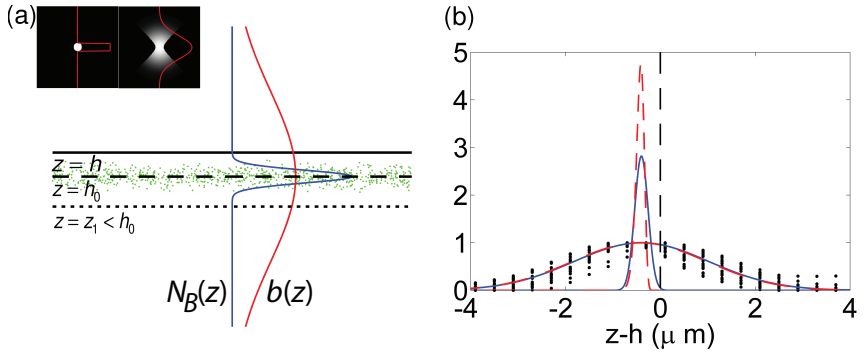

Figure 2.5: Distortion of the vertical position of the marker particles used to measure the traction forces due to image blurring. (a) Sketch of this phenomenon. The intensity of a spherical marker in an xz image obtained with a Z-stack is more similar to a "blurred hourglass" than to an ideal circle. This leads to an apparent profile of particles ($b(z)$, red line) that is much more spread than their actual distribution ($N_B(z)$, blue line). The peak of the intensity profile coincides with the average of $N_B(z)$, so that the systematic error in the vertical position of the markers is cancelled when the focal plane selected to visualize the marker particles is $z = h_0$. If the focal plane $z = z_1 \neq h_0$ was selected, most of the information of particle displacements would be coming from particles at a different vertical position. (b) The black circles are intensity profiles coming from squares of size 40 μm in our gels, represented as a function of $z - h$. The color curves represent our model equations for $N_B(z)$ and $b(z)$. The solid, blue curves have been obtained using a Normal distribution with $\mu = -0.4$ and $\sigma = 0.2$ μm. The dashed, red curves have been obtained using a Log-Normal distribution with $\mu = -1$ and $\sigma = 0.2$ μm. In both cases, the PSF is a Gaussian with a $1/e$ radius of 2 μm.

we are only concerned with distortions of the brightness field, $b(z)$, in the vertical direction

$$b(z) = \int_0^h N_B(\zeta)\mathrm{PSF}(z - \zeta)\, d\zeta, \tag{2.7}$$

where $N_B(\zeta)$ is the distribution of beads along z. The shape of the PSF along the vertical axis is rather complex [87, 88] but for our purposes it can be roughly modeled as a Gaussian as we will show below. To first approximation, the shape of $N_B(\zeta)$ is irrelevant for our estimations provided that $N_B(\zeta)$ is much narrower than the PSF. Fig. 2.5b shows that this condition is fulfilled in our experiments. The black circles in that figure represent profiles of the fluorescence intensity coming from the marker particles as a function of $z - h$. The intensity profile penetrates around 2 μm into the subspace $z > 0$, where there are no beads, indicating that the PSF is indeed much wider than the distribution of beads. We have chosen $N_B(\zeta)$ to be a Normal distribution centered at $z = h_0$ to provide simple analytical estimations but similar results have been obtained numerically for other distributions, including more realistic cases where $N_B(\zeta > 0) = 0$. Using the functions

proposed above we have that

$$b(z) \approx \frac{e^{\frac{-h_0^2}{\delta^2}}}{\pi\delta d}\int_{-\infty}^{\infty}\exp\left[-\frac{(\zeta-h_0)^2}{\delta^2}\right]\exp\left[-\frac{(\zeta-z)^2}{d^2}\right]d\zeta = \frac{e^{-\frac{h_0^2}{\delta^2}}e^{\frac{(z-h_0)^2}{\delta^2+d^2}}}{\sqrt{\pi}\sqrt{\delta^2+d^2}}, \tag{2.8}$$

which becomes

$$b(z) \propto e^{-\frac{(z-h_0)^2}{d^2}} \tag{2.9}$$

in the limit $d >> \delta$ when $N_B(\zeta)$ tends to a Dirac delta. This result indicates that the brightness distribution is approximately equal to the PSF with its origin at the average position of the marker particles. The brightness distribution shown in Fig. 2.5b supports this idea. Eq. 2.9 implies that the marker particles have to be imaged at the plane where their fluorescence brightness is maximum in order to cancel systematic errors in their vertical location. This can be understood simply by observing the diagram in Fig. 2.5a. If a focal plane $z = z_1 \neq h_0$ was selected, most of the information of particle displacements would be coming from particles at a different vertical position. In our experiments, we have always imaged the marker particles at the plane where their brightness is maximum to minimize the systematic errors in their vertical position.

2.1.7 Calculation of traction forces

We computed the stress field $\boldsymbol{\tau} = (\tau_{zx}, \tau_{zy})_{z=h}$ applied on the substrate surface by a cell by solving the elasticity equation of equilibrium for a linear, homogeneous, isotropic, 3D body of finite thickness h. Fig. 2.3a shows a sketch of the problem configuration. The boundary conditions are no slip, $\mathbf{u} = (u, v, w) = 0$, at the bottom of the substrate, $z = 0$, and the measured lateral displacements u^{h_0} and v^{h_0} at the average vertical position of the beads, $z = h_0 \leq h$. We assume periodicity in the horizontal directions. The remaining boundary condition derived from the similar densities of the cells and their surrounding buffer as well as the predominant horizontal orientation of contractile fibers of the cytoskeleton, which suggest that the vertical tensile stresses on the surface of the substrate, $\tau_{zz}(z = h)$, are negligible. We therefore apply the boundary condition $\tau_{zz}(z = h) = 0$. We solve analytically the elastostatic equation using Fourier series,

$$\boldsymbol{\tau}(x, y, z) = \sum_{\alpha=-\infty}^{\infty}\sum_{\beta=-\infty}^{\infty}\widehat{\boldsymbol{\tau}}_{\alpha\beta}(z)\,\exp(\mathrm{i}\alpha x)\,\exp(\mathrm{i}\beta x) \tag{2.10}$$

$$\mathbf{u}(x, y, z) = \sum_{\alpha=-\infty}^{\infty}\sum_{\beta=-\infty}^{\infty}\widehat{\mathbf{u}}_{\alpha\beta}(z)\,\exp(\mathrm{i}\alpha x)\,\exp(\mathrm{i}\beta x) \tag{2.11}$$

where α and β are the x and y wavenumbers, $\widehat{\boldsymbol{\tau}}_{\alpha\beta}$ and $\widehat{\mathbf{u}}_{\alpha\beta}$ are the complex Fourier coefficients of $\boldsymbol{\tau}$ and $\mathbf{u}$. The latter are functions of the vertical coordinate and are linearly related to the Fourier coefficients of the horizontal displacements measured at $z = h_0$, $\widehat{u}^{h_0}_{\alpha\beta}$ and $\widehat{v}^{h_0}_{\alpha\beta}$. A detailed mathematical derivation of the solution is developed in Section 2.2 and 2.2.1. This solution provides the 3 components of the displacement vector and the 9 components of the stress tensor at all positions inside the three-dimensional domain. We are interested in the tangential stresses at $z = h$, which can be expressed in Fourier space as

$$\begin{bmatrix} \widehat{\tau_{xz}}_{\alpha\beta}(h) \\ \widehat{\tau_{yz}}_{\alpha\beta}(h) \end{bmatrix} = T_{\alpha\beta} \begin{bmatrix} \widehat{u}^{h_0}_{\alpha\beta} \\ \widehat{v}^{h_0}_{\alpha\beta} \end{bmatrix}_{\alpha\beta} \tag{2.12}$$

The first $N_x \times N_y$ Fourier coefficients of $\mathbf{u}^{h_0}(x, y)$ were computed using a fast Fourier transform (FFT) algorithm after tapering this function with a two-dimensional Hanning window to ensure its periodicity and thus suppress the Gibbs error [89, 90]. The tapering window was a square of size (L_B) equal to 3 times the major axis of the cell centered at the centroid of the cell. This was the only information about the geometry of the cell that was required to compute the stresses with our method, which is advantageous because determining the cellular area in contact with the substrate is difficult. When L_B was larger than the distance from the center of the cell to the boundary of the image, we instead set L_B equal to that distance. The size of the tapering window and the spatial resolution Δ of the displacement field determine $N = L_B/\Delta$. When N was not suitable for the FFT we used the immediate higher number and set the Fourier coefficients to zero for indexes greater than N. The tapering also minimized the disturbances caused by neighboring cells. The net force $\mathbf{F}_{net}$ exerted on the surface of the substrate is balanced by a force of equal strength and opposite sign applied on its base, given by

$$\mathbf{F} = \frac{E\, {L_B}^2\, \widehat{\mathbf{u}}^{h_0}_{00}}{2(1+\sigma)h_0}, \tag{2.13}$$

where E is the Young's modulus of the gel and $\widehat{\mathbf{u}}^{h_0}_{00}$ is the average displacement vector at $z = h_0$. It is useful to decompose this net force into the sum of the pole forces exerted at the front and back halves of the cell, $\mathbf{F}_f$ and $\mathbf{F}_b$ (see panels on the right of Figs. 2.7b-c), where

$$\mathbf{F}_f = \iint_{\xi>0} \boldsymbol{\tau}(x, y, h)\, dxdy, \tag{2.14}$$

where $\boldsymbol{\tau}(x, y, h)$ is a vector containing the traction stress field exerted at the substrate free substrate. The integral for $\xi < 0$ (see Eq. 2.4) yields $\mathbf{F}_b$. The strain energy or mechanical

work U_S that the cells exert on the substrate is given by

$$U_S = \frac{1}{2}\iiint \bar{\tau}\cdot\bar{\epsilon}\,dxdydz = \frac{L_x L_y}{2}\sum_{\alpha=-\infty}^{\infty}\sum_{\beta=-\infty}^{\infty}\hat{\bar{\tau}}_{\alpha\beta}\cdot\hat{\bar{\epsilon}}_{\alpha\beta}\,dz, \tag{2.15}$$

where $\bar{\tau}$ and $\bar{\epsilon}$ are the stress and strain field tensors respectively. If displacements and stresses decay to zero at the boundaries of the domain, then the strain energy U_S can be simply calculated as the area integral

$$U_S = \frac{1}{2}\int_A \boldsymbol{\tau}(z=h)\cdot\mathbf{u}(z=h)\,dxdy \tag{2.16}$$

where $\mathbf{u}(z=h)$ are the displacement vector field at the substrate free surface. The power exerted by the cell to deform the substrate is then calculated as the time rate of change of U_S.

2.2 Solution of the elastostatic equation in a substrate of finite thickness

We consider a cell moving on the free surface of a linearly elastic substrate of finite thickness h. We adopt a cartesian coordinate system with the x and y axes parallel to the base of the substrate, which is located at $z = 0$. When the cell adheres to the elastic substrate and migrates, it induces a displacement field $\mathbf{u} = (u, v, w)$ whose lateral components are measured on a given horizontal plane by seeding the substrate with particle-markers and tracking their displacements (Section 2.1.4). The measurement plane is located some finite distance from the surface, $z = h_0$. Fig. 2.3a sketches this configuration.

The equations governing the displacement field are

$$\nabla^2\mathbf{u} + \frac{\nabla(\nabla\cdot\mathbf{u})}{(1-2\,\sigma)} = 0. \tag{2.17}$$

The boundary conditions can be partially set up by imposing zero displacements at the base of the substrate,

$$\mathbf{u}(x, y, 0) = 0, \tag{2.18}$$

since the solid glass beneath the substrate is infinitely rigid. We need a second set of boundary conditions to solve this equation. In Sections 2.2.1, 2.2.2, and 2.2.3 we will discuss several possibilities, depending on our experimental configuration and needs.

We sought the solution of Eq. 2.17 in term of the Fourier series of the displacements $\mathbf{u}(x, y, z)$

$$\mathbf{u}(x, y, z) = \sum_{\alpha=-\infty}^{\infty}\sum_{\beta=-\infty}^{\infty}\hat{\mathbf{u}}_{\alpha\beta}(z)\,\exp(\mathrm{i}\alpha x)\,\exp(\mathrm{i}\beta x) \tag{2.19}$$

where α and β are the wavenumbers in the x and y directions, and $\widehat{\mathbf{u}}_{\alpha\beta}$ are the Fourier coefficients of $\mathbf{u}$. Introducing Eq. 2.19 into Eq. 2.17 we obtain the following first-order homogeneous ordinary differential equation

$$\frac{d}{dz}\begin{bmatrix} \widehat{u}_{\alpha\beta} \\ \widehat{v}_{\alpha\beta} \\ \widehat{w}_{\alpha\beta} \\ d\widehat{u}_{\alpha\beta}/dz \\ d\widehat{v}_{\alpha\beta}/dz \\ d\widehat{w}_{\alpha\beta}/dz \end{bmatrix} = \frac{d}{dz}\begin{bmatrix} \widehat{\mathbf{u}}_{\alpha\beta} \\ d\widehat{\mathbf{u}}_{\alpha\beta} \end{bmatrix} = A_{\alpha\beta}\begin{bmatrix} \widehat{\mathbf{u}}_{\alpha\beta} \\ d\widehat{\mathbf{u}}_{\alpha\beta} \end{bmatrix} \tag{2.20}$$

where matrix $A_{\alpha\beta}$ is

$$A_{\alpha\beta} = \begin{bmatrix} 0 & 0 & 0 & 1 & 0 & 0 \\ 0 & 0 & 0 & 0 & 1 & 0 \\ 0 & 0 & 0 & 0 & 0 & 1 \\ \frac{2\alpha^2(1-\sigma)+\beta^2(1-2\sigma)}{1-2\sigma} & \frac{\alpha\beta}{1-2\sigma} & 0 & 0 & 0 & \frac{-\mathrm{i}\alpha}{1-2\sigma} \\ \frac{\alpha\beta}{1-2\sigma} & \frac{2\beta^2(1-\sigma)+\alpha^2(1-2\sigma)}{1-2\sigma} & 0 & 0 & 0 & \frac{-\mathrm{i}\beta}{1-2\sigma} \\ 0 & 0 & \frac{(\alpha^2+\beta^2)(1-2\sigma)}{1-2\sigma} & \frac{-\mathrm{i}\alpha}{1-2\sigma} & \frac{-\mathrm{i}\beta}{1-2\sigma} & 0 \end{bmatrix} \tag{2.21}$$

Matrix $A_{\alpha\beta}$ has two generalized eigenvalues, $\lambda = \pm k = \pm\sqrt{\alpha^2+\beta^2}$, with algebraic multiplicity equal to 3 and geometric multiplicity equal to 2. The matrix of generalized eigenvectors is

$$P_{\alpha\beta} = \begin{bmatrix} \alpha^2 & \mathrm{i}\alpha & -\beta/k & \mathrm{i} & \mathrm{i}\alpha & \alpha\beta \\ \alpha\beta & \mathrm{i}\beta & \alpha/k & 0 & \mathrm{i}\beta & \beta^2 \\ -\mathrm{i}\alpha k & 4k(1-\sigma) & 0 & -\alpha/k & -4k(1-\sigma) & \mathrm{i}\beta k \\ \alpha^2 k & 0 & -\beta & -\mathrm{i}k & 0 & -\alpha\beta k \\ \alpha\beta k & 0 & \alpha & 0 & 0 & -k\beta^2 \\ -\mathrm{i}\alpha k^2 & k^2(3-4\sigma) & 0 & \alpha & k^2(3-4\sigma) & -\mathrm{i}\beta k^2 \end{bmatrix} \tag{2.22}$$

and its associated Jordan form is

$$J_{\alpha\beta} = P_{\alpha\beta}^{-1}\, A_{\alpha\beta}\, P_{\alpha\beta} = \begin{bmatrix} k & -\mathrm{i}k/\alpha & 0 & 0 & 0 & 0 \\ 0 & k & 0 & 0 & 0 & 0 \\ 0 & 0 & k & 0 & 0 & 0 \\ 0 & 0 & 0 & -k & 0 & 0 \\ 0 & 0 & 0 & 0 & -k & 0 \\ 0 & 0 & 0 & 0 & \mathrm{i}k/\beta & -k \end{bmatrix}. \tag{2.23}$$

The solution of the differential equation Eq. 2.20 is

$$\begin{bmatrix} \widehat{\mathbf{u}}_{\alpha\beta} \\ d\widehat{\mathbf{u}}_{\alpha\beta} \end{bmatrix} = P_{\alpha\beta}\, \exp\left(J_{\alpha\beta}\left(z\right)\right)\, P_{\alpha\beta}^{-1} \begin{bmatrix} \widehat{\mathbf{u}}^0_{\alpha\beta} \\ d\widehat{\mathbf{u}}^0_{\alpha\beta} \end{bmatrix} = P_{\alpha\beta}\, \exp\left(J_{\alpha\beta}\left(z\right)\right)\, P_{\alpha\beta}^{-1} \begin{bmatrix} \mathbf{0} \\ d\widehat{\mathbf{u}}^0_{\alpha\beta} \end{bmatrix} \tag{2.24}$$

where $\widehat{\mathbf{u}}^0_{\alpha\beta}$ and $d\widehat{\mathbf{u}}^0_{\alpha\beta}$ are the boundary values of $\widehat{\mathbf{u}}_{\alpha\beta}$ and $d\widehat{\mathbf{u}}_{\alpha\beta}$ at $z = 0$. The solution in Eq. 2.24 can be rewritten as

$$\begin{bmatrix} \widehat{\mathbf{u}}_{\alpha\beta} \\ d\widehat{\mathbf{u}}_{\alpha\beta} \end{bmatrix} = \begin{bmatrix} \mathbf{U_0} & \mathbf{V_0} & \mathbf{W_0} \\ \mathbf{dU_0} & \mathbf{dV_0} & \mathbf{dW_0} \end{bmatrix} \begin{bmatrix} d\widehat{\mathbf{u}}^0_{\alpha\beta} \end{bmatrix} \tag{2.25}$$

with

$$\begin{bmatrix} \mathbf{U_0} \\ \mathbf{dU_0} \end{bmatrix} = \begin{bmatrix} -1/4\,\frac{\alpha^2 z\cosh(k\,z)}{k^2(-1+\sigma)} - 1/4\,\frac{\left(3\,\alpha^2-4\,\alpha^2\sigma+4\,\beta^2-4\,\beta^2\sigma\right)\sinh(k\,z)}{k^3(-1+\sigma)} \\ -1/4\,\frac{\alpha\,\beta\,z\cosh(k\,z)}{k^2(-1+\sigma)} + 1/4\,\frac{\alpha\,\beta\,\sinh(k\,z)}{k^3(-1+\sigma)} \\ \frac{1/4\,i\sinh(k\,z)z\alpha}{(-1+\sigma)k} \\ -1/4\,\frac{(4\,k-4\,k\,\sigma)\cosh(k\,z)}{(-1+\sigma)k} - 1/4\,\frac{\alpha^2 z\sinh(k\,z)}{(-1+\sigma)k} \\ -1/4\,\frac{\alpha\,\beta\,z\sinh(k\,z)}{(-1+\sigma)k} \\ \frac{1/4\,iz\alpha\,\cosh(k\,z)}{-1+\sigma} + \frac{1/4\,i\alpha\,\sinh(k\,z)}{(-1+\sigma)k} \end{bmatrix}, \tag{2.26}$$

$$\begin{bmatrix} \mathbf{V_0} \\ \mathbf{dV_0} \end{bmatrix} = \begin{bmatrix} -1/4\,\frac{\alpha\,\beta\,z\cosh(k\,z)}{k^2(-1+\sigma)} + 1/4\,\frac{\alpha\,\beta\,\sinh(k\,z)}{k^3(-1+\sigma)} \\ -1/4\,\frac{\beta^2 z\cosh(k\,z)}{k^2(-1+\sigma)} - 1/4\,\frac{\left(3\,\beta^2-4\,\beta^2\sigma+4\,\alpha^2-4\,\alpha^2\sigma\right)\sinh(k\,z)}{k^3(-1+\sigma)} \\ \frac{1/4\,i\sinh(k\,z)z\beta}{k\,(-1+\sigma)} \\ -1/4\,\frac{\alpha\,\beta\,z\sinh(k\,z)}{k\,(-1+\sigma)} \\ -1/4\,\frac{(4\,k-4\,k\,\sigma)\cosh(k\,z)}{k\,(-1+\sigma)} - 1/4\,\frac{\beta^2 z\sinh(k\,z)}{k\,(-1+\sigma)} \\ \frac{1/4\,iz\beta\,\cosh(k\,z)}{-1+\sigma} + \frac{1/4\,i\beta\,\sinh(k\,z)}{k\,(-1+\sigma)} \end{bmatrix}, \tag{2.27}$$

and

$$\begin{bmatrix} \mathbf{W_0} \\ \mathbf{dW_0} \end{bmatrix} = \begin{bmatrix} \frac{1/2\,i\alpha\,z\sinh(k\,z)}{k\,(-1+2\,\sigma)} \\ \frac{1/2\,i\beta\,z\sinh(k\,z)}{k\,(-1+2\,\sigma)} \\ 1/2\,\frac{z\cosh(k\,z)}{-1+2\,\sigma} + 1/2\,\frac{(-3+4\,\sigma)\sinh(k\,z)}{k\,(-1+2\,\sigma)} \\ \frac{1/2\,i\alpha\,z\cosh(k\,z)}{-1+2\,\sigma} + \frac{1/2\,i\alpha\,\sinh(k\,z)}{k\,(-1+2\,\sigma)} \\ \frac{1/2\,i\beta\,z\cosh(k\,z)}{-1+2\,\sigma} + \frac{1/2\,i\beta\,\sinh(k\,z)}{k\,(-1+2\,\sigma)} \\ 1/2\,\frac{(-2+4\,\sigma)\cosh(k\,z)}{-1+2\,\sigma} + 1/2\,\frac{k\,z\sinh(k\,z)}{-1+2\,\sigma} \end{bmatrix}. \tag{2.28}$$

The Fourier coefficients of the z-derivative of the displacements at $z = 0$, $d\widehat{\mathbf{u}}^0_{\alpha\beta}$, can be determined using additional boundary conditions, which will depend on the type of experiments performed. As already indicated, different possibilities for these boundary conditions are explored in Sections 2.2.1, 2.2.2 and 2.2.3.

2.2.1 Calculation of 2D traction stresses: horizontal displacements at a plane are known and tensile stresses at substrate free surface are negligible

In case we measure the horizontal displacements at $z = h_0 \leq h$ from images of the fluorescent markers at that plane (see Section 2.1.6), the boundary conditions can be partially set as

$$u(x, y, h_0) = u^{h_0}(x, y)\,,\; v(x, y, h_0) = v^{h_0}(x, y), \tag{2.29}$$

where u^{h_0} and v^{h_0} are the measured horizontal displacements.

The remaining boundary condition we used is that the vertical stresses on the substrate free surface are zero,

$$\tau_{zz}(x, y, h) = 0. \tag{2.30}$$

This is in principle a reasonable assumption since the weight of the cell is negligibly small due to the similar densities of the cells and their surrounding buffer fluid, and because the force-generating elements of the cytoskeleton have a predominant horizontal orientation. This is the configuration for the traction force cytometry experiments analyzed in Section 3.

To impose Eq. 2.30, we use the constitutive law that relates the Fourier coefficients of the vertical tensile stresses to those of the displacements,

$$\widehat{\tau_{zz}}_{\alpha\beta}(h) = \frac{E}{(1+\sigma)(1-2\sigma)}\left[i\sigma\left(\alpha\widehat{u}_{\alpha\beta}(h) + \beta\widehat{v}_{\alpha\beta}(h)\right) + \frac{d\widehat{w}_{\alpha\beta}}{dz}(h)\right]. \tag{2.31}$$

Evaluating Eq. 2.25 at $z = h_0$ and h, and using the above expression to impose the boundary condition in Eq. 2.30, we obtain the following 3×3 linear system of equations,

$$B_{\alpha\beta}\begin{bmatrix} d\widehat{u}^0_{\alpha\beta} \\ d\widehat{v}^0_{\alpha\beta} \\ d\widehat{w}^0_{\alpha\beta} \end{bmatrix} = \begin{bmatrix} \widehat{u}^{h_0}_{\alpha\beta} \\ \widehat{v}^{h_0}_{\alpha\beta} \\ 0 \end{bmatrix} \tag{2.32}$$

where $(\widehat{u}^{h_0}_{\alpha\beta}, \widehat{u}^{h_0}_{\alpha\beta})$ are the Fourier coefficients of the measured displacements at $z = h_0$. The solution of this system yields the three unknown coefficients needed to obtain the displacements, effectively closing the problem. The different components in matrix $B_{\alpha\beta}$ are

$$B^{[1,1]}_{\alpha\beta} = \frac{-\alpha^2 k h_0 \cosh(kh_0) + [k^2(-3+4\sigma) - \beta^2]\sinh(kh_0)}{4(-1+\sigma)k^3}, \tag{2.33}$$

$$B_{\alpha\beta}^{[1,2]} = \frac{\alpha\beta[-kh_0\cosh(kh_0)+\sinh(kh_0)]}{4k^3(1-\sigma)}, \tag{2.34}$$

$$B_{\alpha\beta}^{[1,3]} = \frac{i\alpha h_0\sinh(kh_0)}{k(-1+2\sigma)}, \tag{2.35}$$

$$B_{\alpha\beta}^{[2,1]} = B_{\beta\alpha}^{[1,2]}, \tag{2.36}$$

$$B_{\alpha\beta}^{[2,2]} = B_{\beta\alpha}^{[1,1]}, \tag{2.37}$$

$$B_{\alpha\beta}^{[2,3]} = B_{\beta\alpha}^{[1,3]}, \tag{2.38}$$

$$B_{\alpha\beta}^{[3,1]} = \frac{i\alpha(-1+2\sigma)[-kh\sinh(kh)+(-1+2\sigma)\sinh(kh)]}{4k(-1+\sigma)}, \tag{2.39}$$

$$B_{\alpha\beta}^{[3,2]} = B_{\beta\alpha}^{[3,1]}, \tag{2.40}$$

$$B_{\alpha\beta}^{[3,3]} = \frac{2(1-\sigma)\cosh(kh)-kh\sinh(kh)}{2}. \tag{2.41}$$

The solution of the linear system in Eq. 2.32 closes the problem by providing the unknowns that are required to determine $\widehat{\mathbf{u}}_{\alpha\beta}(z)$ and $d\widehat{\mathbf{u}}_{\alpha\beta}(z)$ in Eq. 2.25. The Fourier coefficients of the tangential stress field on the surface of the substrate are related to $\widehat{\mathbf{u}}_{\alpha\beta}(z)$ and $d\widehat{\mathbf{u}}_{\alpha\beta}(z)$ through the constitutive equations

$$\widehat{\tau_{xz}}_{\alpha\beta}(h) = \frac{E}{2(1+\sigma)}\left[i\alpha\widehat{w}_{\alpha\beta}(h)+\frac{d\widehat{u}_{\alpha\beta}}{dz}(h)\right], \tag{2.42}$$

$$\widehat{\tau_{yz}}_{\alpha\beta}(h) = \frac{E}{2(1+\sigma)}\left[i\beta\widehat{w}_{\alpha\beta}(h)+\frac{d\widehat{v}_{\alpha\beta}}{dz}(h)\right], \tag{2.43}$$

The inverse Fourier transform of these coefficients yields the traction field on the surface of the substrate,

$$(\tau_{xz},\tau_{yz})(h) = \sum_{\alpha=-\infty}^{\infty}\sum_{\beta=-\infty}^{\infty}\left(\widehat{\tau_{xz}}_{\alpha\beta},\widehat{\tau_{yz}}_{\alpha\beta}\right)(h)\exp(i\alpha x)\exp(i\beta y). \tag{2.44}$$

We now present the asymptotic behavior of the solution for very high wavenumbers, $kh_0 \gg 1$. In this limit, the solution in Eq. 2.25 becomes

$$\begin{bmatrix}\widehat{\mathbf{u}}_{\alpha\beta}(z)\\ d\widehat{\mathbf{u}}_{\alpha\beta}(z)\end{bmatrix} \sim h\exp(kh)\begin{bmatrix}\mathbf{0}\\ d\widehat{\mathbf{u}}^0_{\alpha\beta}\end{bmatrix}. \tag{2.45}$$

A more detailed analysis is required for $B_{\alpha\beta}$, which becomes

$$B_{\alpha\beta} \sim h_0 e^{kh_0} \begin{bmatrix} \frac{\alpha^2-[(3-4\sigma)\alpha^2-4\beta^2(1-\sigma)]\epsilon}{4k^2(1-\sigma)} & \frac{\alpha\beta(1-\epsilon)}{4k^2(1-\sigma)} & \frac{-i\alpha}{2k(1-\sigma)} \\ \frac{\alpha\beta(1-\epsilon)}{4k^2(1-\sigma)} & \frac{\beta^2-[(3-4\sigma)\beta^2-4\alpha^2(1-\sigma)]\epsilon}{4k^2(1-\sigma)} & \frac{-i\beta}{2k(1-\sigma)} \\ \frac{-i\alpha h(1-\sigma)e^{k(h-h_0)}[1+(1-2\sigma)\epsilon]}{kh_0(1-\sigma)} & \frac{-i\beta h(1-\sigma)e^{k(h-h_0)}[1+(1-2\sigma)\epsilon]}{kh_0(1-\sigma)} & \frac{he^{k(h-h_0)}[2(1-\sigma)\epsilon-1]}{2h_0} \end{bmatrix} \tag{2.46}$$

The small parameter $\epsilon = (kh_0)^{-1}$ has been kept in the above expression because $B_{\alpha\beta}$ is singular at leading order. For $\epsilon \ll 1$, the solution of Eq. 2.32 is written as

$$\begin{bmatrix} d\widehat{u}^0_{\alpha\beta} \\ d\widehat{v}^0_{\alpha\beta} \\ d\widehat{w}^0_{\alpha\beta} \end{bmatrix} \propto [h_0 \exp(kh_0)]^{-1} \left(\frac{1}{\epsilon}\right) = k \exp(-kh_0) \tag{2.47}$$

Combining this expression with Eq. 2.45, we finally get a simple formula that relates the displacements at $z = h$ with those measured at $z = h_0$,

$$\begin{bmatrix} \widehat{\mathbf{u}}_{\alpha\beta}(h) \\ d\widehat{\mathbf{u}}_{\alpha\beta}(h) \end{bmatrix} \sim kh \exp[k(h-h_0)] \widehat{\mathbf{u}}_{\alpha\beta}(h_0) \tag{2.48}$$

in the limit $kh_0 \gg 1$. This result shows that the amplitude of the small-scale features of the displacements measured at $z = h_0$ are smaller than those at $z = h$, and that the ratio between these two increases exponentially with the wave number. Using Eqs. 2.42 and 2.43, it follows that the traction forces exhibit the same exponential dependence on the distance from the substrate of the gel to the measurement plane $(h - h_0)$.

2.2.2 Calculation of 3D traction stresses: three dimensional displacements at substrate free surface are known

Another possible experimental configuration is to capture images of the fluorescent markers embedded in the substrate at various z-planes close to the substrate free surface at each instant of time. This allows for the measurement of the three components of the displacements at $z = h$, $\mathbf{u}^h(x, y)$, which can be used as boundary conditions, providing the z-derivatives of the Fourier coefficients of the the displacements at $z = 0$, $d\mathbf{u}^0_{\alpha\beta}$, after solving (see Eq. 2.25)

$$\begin{bmatrix} d\widehat{\mathbf{u}}^0_{\alpha\beta} \end{bmatrix} = \begin{bmatrix} \mathbf{U_0} & \mathbf{V_0} & \mathbf{W_0} \end{bmatrix}^{-1}_{z=h} \begin{bmatrix} \widehat{\mathbf{u}}^h_{\alpha\beta} \end{bmatrix} = \begin{bmatrix} C_{1u} & C_{1v} & C_{1w} \\ C_{2u} & C_{2v} & C_{2w} \\ C_{3u} & C_{3v} & C_{3w} \end{bmatrix} \begin{bmatrix} \widehat{\mathbf{u}}^h_{\alpha\beta} \end{bmatrix} \tag{2.49}$$

where

$$C_{1u} = \frac{\left(-4\beta^2h^2 + 2(-3+4\sigma)^2\left(\cosh(2kh)-1\right)\right)k^2 + 8\alpha^2 kh(-1+\sigma)\sinh(2kh)}{\left(4k^2h^2 + 3(-3+4\sigma)^2\right)k\sinh(kh) - (-3+4\sigma)^2 k\sinh(3kh)} + \\ + \frac{-2\alpha^2\left(\cosh(2kh)-1\right)(-3+4\sigma)}{\left(4k^2h^2 + 3(-3+4\sigma)^2\right)k\sinh(kh) - (-3+4\sigma)^2 k\sinh(3kh)}, \tag{2.50}$$

$$C_{1v} = \frac{4\alpha\beta k^2h^2 + 8\alpha\beta kh(-1+\sigma)\sinh(2kh) + 2\alpha\beta(-3+4\sigma)\left(1-\cosh(2kh)\right)}{\left(4k^2h^2 + 3(-3+4\sigma)^2\right)k\sinh(kh) - (-3+4\sigma)^2 k\sinh(3kh)}, \tag{2.51}$$

$$C_{1w} = \frac{-8ikh\alpha(-1+\sigma)\left(\cosh(2kh)-1\right)}{\left(4k^2h^2 + 3(-3+4\sigma)^2\right)\sinh(kh) - (-3+4\sigma)^2\sinh(3kh)}, \tag{2.52}$$

$$C_{2u}(\alpha,\beta) = C_{1v}(\beta,\alpha), \tag{2.53}$$

$$C_{2v}(\alpha,\beta) = C_{1u}(\beta,\alpha), \tag{2.54}$$

$$C_{2w}(\alpha,\beta) = C_{1w}(\beta,\alpha), \tag{2.55}$$

$$C_{3u}(\alpha,\beta) = \frac{-4i\alpha(-1+2\sigma)kh\sinh(kh)}{(-3+4\sigma)^2\left(\cosh(2kh)-1\right) - 2(kh)^2}, \tag{2.56}$$

$$C_{3v}(\alpha,\beta) = C_{3u}(\beta,\alpha), \tag{2.57}$$

$$C_{3w} = \frac{4(-1+2\sigma)\left(-kh\cosh(kh) + (-3+4\sigma)\sinh(kh)\right)}{(-3+4\sigma)^2\left(\cosh(2kh)-1\right) - 2(kh)^2}. \tag{2.58}$$

Once we have solved for $d\mathbf{u}^0_{\alpha\beta}$, Eq. 2.25 provides the Fourier coefficients of the displacement field and their z-derivatives at any given z-location, allowing for the computation of the traction stresses (Eq. 2.42 and 2.43).

In case our experimental configuration allow us to obtain only the horizontal displacements at the substrate free surface, another possible set of boundary conditions are to impose known horizontal displacements and zero vertical displacements at $z = h$.

2.2.3 Calculation of 3D displacements: three dimensional traction stresses at substrate free surface are known

For analytical purposes, it may be of practical use to obtain the displacement field generated by a specific traction force field at the substrate free surface. Assuming that we know the distribution of traction stresses at $z = h$, $\boldsymbol{\tau}^h(x, y) = (\tau^h_{xz}, \tau^h_{yz}, \tau^h_{zz})(x, y)$, their Fourier coefficients are related to $d\mathbf{u}^0_{\alpha\beta}$ as

$$\mathbf{D}\left[\ d\widehat{\mathbf{u}}^0_{\alpha\beta}\ \right] = \left[\begin{array}{c} \widehat{\tau_{xz}}^h_{\alpha\beta} \\ \widehat{\tau_{yz}}^h_{\alpha\beta} \\ \widehat{\tau_{zz}}^h_{\alpha\beta} \end{array}\right]_{z=h} \tag{2.59}$$

where

$$\mathbf{D} = \mathbf{E}\left[\begin{array}{ccc} \mathbf{U_0} & \mathbf{V_0} & \mathbf{W_0} \\ \mathbf{dU_0} & \mathbf{dV_0} & \mathbf{dW_0} \end{array}\right]_{z=h} \tag{2.60}$$

and

$$\mathbf{E} = \left[\begin{array}{cccccc} 0 & 0 & \frac{Ei\alpha}{2(1+\sigma)} & \frac{E}{2(1+\sigma)} & 0 & 0 \\ 0 & 0 & \frac{Ei\alpha}{2(1+\sigma)} & 0 & \frac{E}{2(1+\sigma)} & 0 \\ \frac{Ei\alpha\sigma}{(1+\sigma)(1-2\sigma)} & \frac{Ei\beta\sigma}{(1+\sigma)(1-2\sigma)} & 0 & 0 & 0 & \frac{E(1-\sigma)}{(1+\sigma)(1-2\sigma)} \end{array}\right] \tag{2.61}$$

from the constitutive equations relating traction stresses and displacements. The solution for the system of equations in Eq. 2.59 is

$$\left[\ d\widehat{\mathbf{u}}^0_{\alpha\beta}\ \right] = \mathbf{D}^{-1}\left[\begin{array}{c} \widehat{\tau_{xz}}^h_{\alpha\beta} \\ \widehat{\tau_{yz}}^h_{\alpha\beta} \\ \widehat{\tau_{zz}}^h_{\alpha\beta} \end{array}\right] = \left[\begin{array}{ccc} C_{1u} & C_{1v} & C_{1w} \\ C_{2u} & C_{2v} & C_{2w} \\ C_{3u} & C_{3v} & C_{3w} \end{array}\right]\left[\begin{array}{c} \widehat{\tau_{xz}}^h_{\alpha\beta} \\ \widehat{\tau_{yz}}^h_{\alpha\beta} \\ \widehat{\tau_{zz}}^h_{\alpha\beta} \end{array}\right] \tag{2.62}$$

with

$$C_{1u} = \frac{C_{1uN}}{C_{1D}} \tag{2.63}$$

where

$$C_{1uN} = \left(-8h^2k^4 + 8\sinh(2kh)(-1+\sigma)hk^3 + 4(-1+2\sigma)^2\left(\cosh(2kh)-1\right)k^2\right)\beta^2 - 8\sinh(2kh)(-1+\sigma)hk^5 - 16(-1+\sigma)^2\left(\cosh(2kh)+1\right)k^4$$

and

$$C_{1D} = \left(8i\beta(-1+\sigma)\left(\cosh(2kh)+1\right)hk^4 + 8i\beta(-1+2\sigma)(-1+\sigma)\sinh(2kh)k^3\right)$$

$$C_{1v} = \frac{C1vN}{C_{1D}} \tag{2.64}$$

where

$$C_{1vN} = \left(8h^2k^4 - 8\sinh(2kh)(-1+\sigma)hk^3 - 4\left(-1+2\sigma\right)^2\left(\cosh(2kh)-1\right)k^2\right)\beta\alpha$$

$$C_{1w} = \frac{C1wN}{C_{1D}} \tag{2.65}$$

where

$$C_{1wN} = 8i\alpha k^3\left(kh\cosh(2kh) - (1-2\sigma)\sinh(2kh) + kh\right)(1-\sigma)$$

$$C_{2u}(\alpha,\beta) = C_{1v}(\beta,\alpha) \tag{2.66}$$

$$C_{2v}(\alpha,\beta) = C_{1u}(\beta,\alpha) \tag{2.67}$$

$$C_{2w}(\alpha,\beta) = C_{1w}(\beta,\alpha) \tag{2.68}$$

and

$$C_{3u} = \frac{C_{3uN}}{C_{3D}} \tag{2.69}$$

where

$$C_{3uN} = (1+\sigma)(1-2\sigma)\left(4ih\cosh(kh)k^4 - 4i\sinh(kh)(-1+2\sigma)k^3\right)\alpha$$

and

$$C_{3D} = \left(2k^6h^2 + \left((3-4\sigma)\cosh(2kh) + 4(-1+2\sigma)(-1+\sigma) + 1\right)k^4\right)$$

$$C_{3v}(\alpha,\beta) = C_{3u}(\beta,\alpha) \tag{2.70}$$

and finally

$$C_{3w} = \frac{C3wN}{C_{3D}} \tag{2.71}$$

where

$$C_{3wN} = (1-2\sigma)(1+\sigma)\left(4k^5h\sinh(kh) - 8\cosh(kh)(-1+\sigma)k^4\right)$$

Again, once we have solved for $d\mathbf{u}^0_{\alpha\beta}$, Eq. 2.25 provides the Fourier coefficients of the displacement field and their z-derivatives at any given z-location, allowing for the computation of the traction stresses (Eq. 2.42 and 2.43).

2.3 Effect of the finite thickness of the substrate in the calculation of the traction stresses

The traction force cytometry method in Sections 2.2 and 2.2.1 relies on the analytic solution of the equation of static equilibrium for substrates of finite thickness which assumes negligible vertical stresses at the substrate free surface are negligible, and considers non-zero distances between the measurement plane and the substrate free surface. These two effects were usually neglected in previous works [28, 31, 33, 91–93]. Fig. 2.6 shows the errors associated with the approximations in the Boussinesq's solution. The color curves represent the first and second invariants of the transfer matrix that converts the Fourier coefficients of the measured displacements into those of the tangential stresses on the substrate surface (see Eq. 2.12). The data have been plotted as a function of the modulus of the wave number vector $k = \sqrt{\alpha^2 + \beta^2}$ for the representative case when $\alpha = \beta$. The color curves represent the Frobenius norm of the transfer matrix that converts the Fourier coefficients of the measured displacements into those of the tangential stresses on the substrate free surface (see Eq. 2.12):

$$R_T(\alpha, \beta) = \sqrt{tr(T^*_{\alpha\beta} T_{\alpha\beta})}/E, \tag{2.72}$$

where $()^*$ denotes Hermitian transposition (conjugate transposition), and $tr()$ is the trace of a matrix. The data have been plotted as a function of the modulus of the wave number vector $k = \sqrt{\alpha^2 + \beta^2}$ for the representative case when $\alpha = \beta$.

Our exact solution differs substantially from Boussinesq's for $kh < 3$ (by $\gtrsim 10\%$). In this spectral range, the stresses generated by a unit displacement on the surface of the substrate decay slowly with the distance from it and "feel" the bottom of the domain. This is especially clear at $k = 0$, where our solution yields a positive first invariant that is consistent with a non-zero net force (see Eq. 2.13). The semi-infinite thickness approximation was justified previously by the small displacements of the beads relative to h [31, 91, 93]. However, this assumption is not correct since the relevant lengthscale to be compared with h is the horizontal lengthscale of the deformation field. There are multiple plausible candidates for this lengthscale, i.e., the typical size of the cell-to-substrate adhesions, the characteristic distance between these adhesions, the size of the cell, the distance between nearby cells, or the horizontal dimensions of the domain in which the deformations are measured. Several of these lengthscales were proposed before [33] but in absence of experimental evidence, it was not possible to identify the proper one. Fig. 2.6 shows that the appropriate lengthscale to compare with h is the length of the cell. The black curve is the spectral energy density

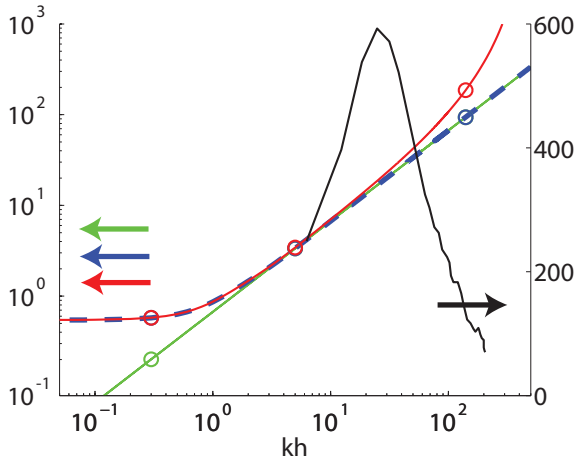

Figure 2.6: Spectral analysis of our 2D solution for substrates of finite thickness and Boussinesq's solution of the elastostatic equation. The color curves follow the left vertical axis and represent the Frobenius norm of the matrix that converts the Fourier coefficients of the measured displacements into those of the tangential stresses on the substrate free surface (see Eq. 2.72) for Poisson's ratio $\sigma = 0.3$. Green, Boussinesq's solution; blue, our solution with $h = h_0$; red, our solution with $h = 1.003\,h_0$. The black curve follows the right vertical axis and shows the spectral energy density of the displacements field in Fig. 2.7a.

of the displacements measured for an example cell, shown in Fig. 2.7a. The spectrum spans the wavenumber range $10 \leq kh \leq 100$ and peaks at $kh \approx 30$, which is equivalent to a length of 26 µm for the corresponding gel thickness, $h = 125$ µm. This characteristic length is approximately the cell length, L, in Fig. 2.7a, and the same correlation is observed for all other cells investigated. Therefore, in order for the infinite-thickness approximation to be valid, the cell length, L, must be much smaller than the thickness of the substrate, which was not always the case in earlier studies [28, 31, 33, 91].

The limit of $kh \approx 3$ implies that if the substrate is thicker than $\approx \lambda/2$, the cell will not be able to sense the infinite rigidity of the bottom substrate. Although the ultimate answer to this question depends on the sensitivity of the mechanotransduction machinery of the cell, a critical value around $kh \approx 3$ agrees with experimental evidence [94, 95].

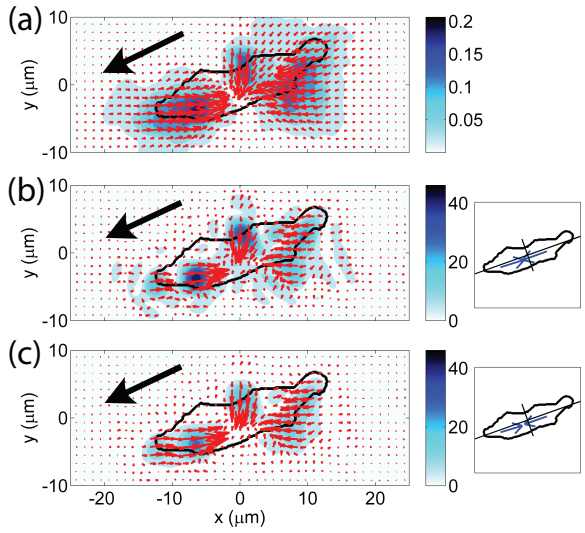

Figure 2.7: Analysis of the mechanics of locomotion of a *Dictyostelium WT* cell migrating up a gradient of the chemoattractant cAMP emitted from a micropipette (see Section 2.1.1). The arrows indicate the intensity and direction of the vector data. The color contours indicate their intensity according to the color bars. The black arrow indicates the direction of motion of the cell. (a) Instantaneous displacements in micrometers. (b) and (c) Instantaneous stresses in Pa; the diagrams on the right show the cell principal axes and the front ($\mathbf{F}_f$) and back ($\mathbf{F}_b$) pole forces. (b) $h - h_0 = 0.4$ μm; $|\mathbf{F}_f| = 624$ pN, $|\mathbf{F}_b| = 648$ pN. (c), $h = h_0$; $\mathbf{F}_f = 572$ pN, $\mathbf{F}_b = 596$ pN. In this specific experiment, the Young's modulus E was 631 Pa and the Poisson's ratio σ was 0.3.

2.4 Effect of the gap between the free surface of the substrate and the displacement marker particles in the calculation of the traction stresses

Boussinesq's solution also underestimates the stresses at high wavenumbers because it neglects the non-zero distances between the beads and the free surface of the substrate, $h - h_0$. This introduces a low-pass filter that has the form $\exp[-k(h - h_0)]$ for $kh \gg 1$ (see Section 2.2) and significantly damps all features shorter or narrower than $2\pi/\log 2 \approx 10$ times $h - h_0$. The exponential filter is important at high wavenumbers even when the gap between the beads and the substrate surface is small, as shown in Fig. 2.6.

The experimental displacement spectrum in Fig. 2.6 is high in the wavenumber interval where the corrections to the Boussinesq's solution because of the gap between the imaged plane of beads and the substrate surface are considerable. This fact is confirmed by Figs. 2.7b-c, which depicts examples of instantaneous tangential stresses on the surface of

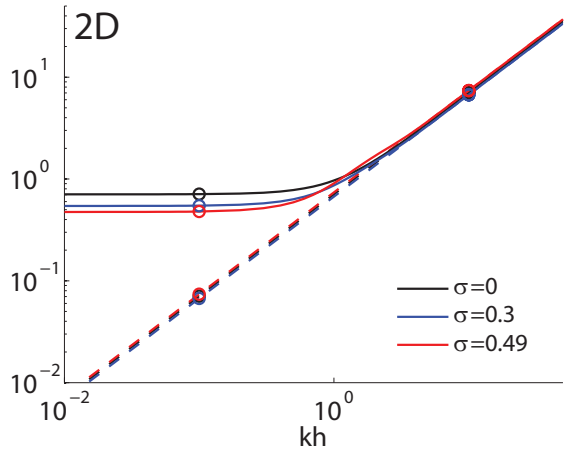

Figure 2.8: Spectral analysis of our 2D solution (solid lines) (see Section 2.2.1) and Boussinesq's solution (dashed lines) of the elastostatic equation for different Poisson's ratios. Spectral distribution of the Frobenius norm of the matrix that converts the Fourier coefficients of the measured displacements at the substrate free surface into those of the tangential stresses at the substrate free surface (see Eq. 2.72) for $\sigma = 0$ (black), $\sigma = 0.3$ (blue), and $\sigma = 0.49$ (red).

the substrate, $\tau_{xz}(x, y, h)$ and $\tau_{yz}(x, y, h)$, computed from the displacements in Fig. 2.7a for positive and zero values of $h - h_0$. Fig. 2.7b displays the results obtained by using the finite thickness solution for $h - h_0 = 0.4$ µm, showing three localized areas of traction in the front, middle, and back of the cell. The magnitude of the stresses in these areas is ≈ 50 Pa and decays rapidly with distance. Fig. 2.7c shows the same results when using the condition $h - h_0 = 0$. Although the patterns in the stress field are similar to those in Fig. 2.7b, their intensity is reduced by 50%. In our experiments, $h - h_0$ was estimated to be between 0 and 0.4 µm (see Section 2.1.6), so the true tangential stresses applied by the cell are in between the values shown in Figs. 2.7b-c.

2.5 Effect of the Poisson's ratio in the calculation of the traction stresses

Poisson's ratio, σ, the ratio of transverse contraction strain to longitudinal extension strain in the direction of stretching force, is required for the calculation of the traction stresses. However, not much attention is payed to its experimental determination in traction force cytometry assays. We aim to provide a quantification of the effect of Poisson's ratio in the calculation of the traction stresses exerted by cells.

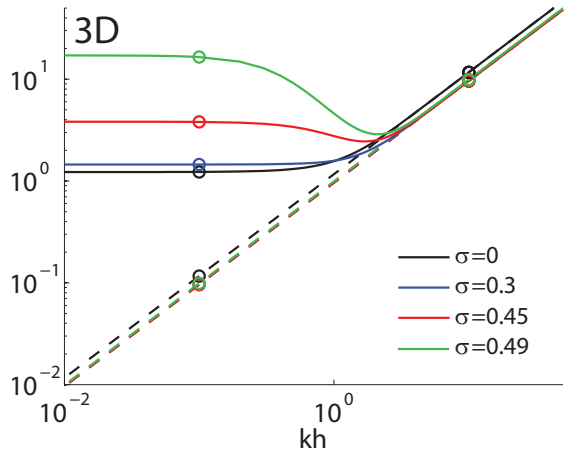

Figure 2.9: Spectral analysis of our 3D solution (solid lines) (see Section 2.2.2) and Boussinesq's solution (dashed lines) of the elastostatic equation for different Poisson's ratios. Spectral distribution of the Frobenius norm of the matrix that converts the Fourier coefficients of the measured displacements at the substrate free surface into those of the tangential stresses at the substrate free surface (see Eq. 2.72) for $\sigma = 0$ (black), $\sigma = 0.3$ (blue), $\sigma = 0.45$ (red), and $\sigma = 0.49$ (green).

Fig. 2.8 shows the spectral analysis of our 2D solution and Boussinesq's solution for different values of σ. This analysis shows that inaccuracies in the determination of σ leads to small errors for $kh \gtrsim 3$ ($\approx 5\%$), becoming maximal for $kh \lesssim 1$ ($\approx 20 - 30\%$).

Fig. 2.9 shows the spectral analysis of our 3D solution and the 3D Boussinesq's solution, showing that the calculation of the 3D traction stresses is very dependent on a good characterization of the Poisson's ratio of the substrate for wavenumbers $kh \lesssim 3$. This dependence on the Poisson's ratio is specially relevant for materials close to incompressible ($\sigma \approx 0.5$). For instance, there is a 300% difference between the norms of the conversion matrices for $\sigma = 0.45$ and 0.49 for $kh \lesssim 3$.

Altogether, these results indicate that for wavenumbers $kh \lesssim 3$ (that is, when cell length $L \approx \lambda > 2h$) and when vertical traction stresses are comparable to horizontal stresses (that is, when vertical stresses are non-negligible and the 3D solution is required), the accuracy of the calculated traction stresses is strongly dependent on a good characterization of the Poisson's ratio of the substrate, σ.

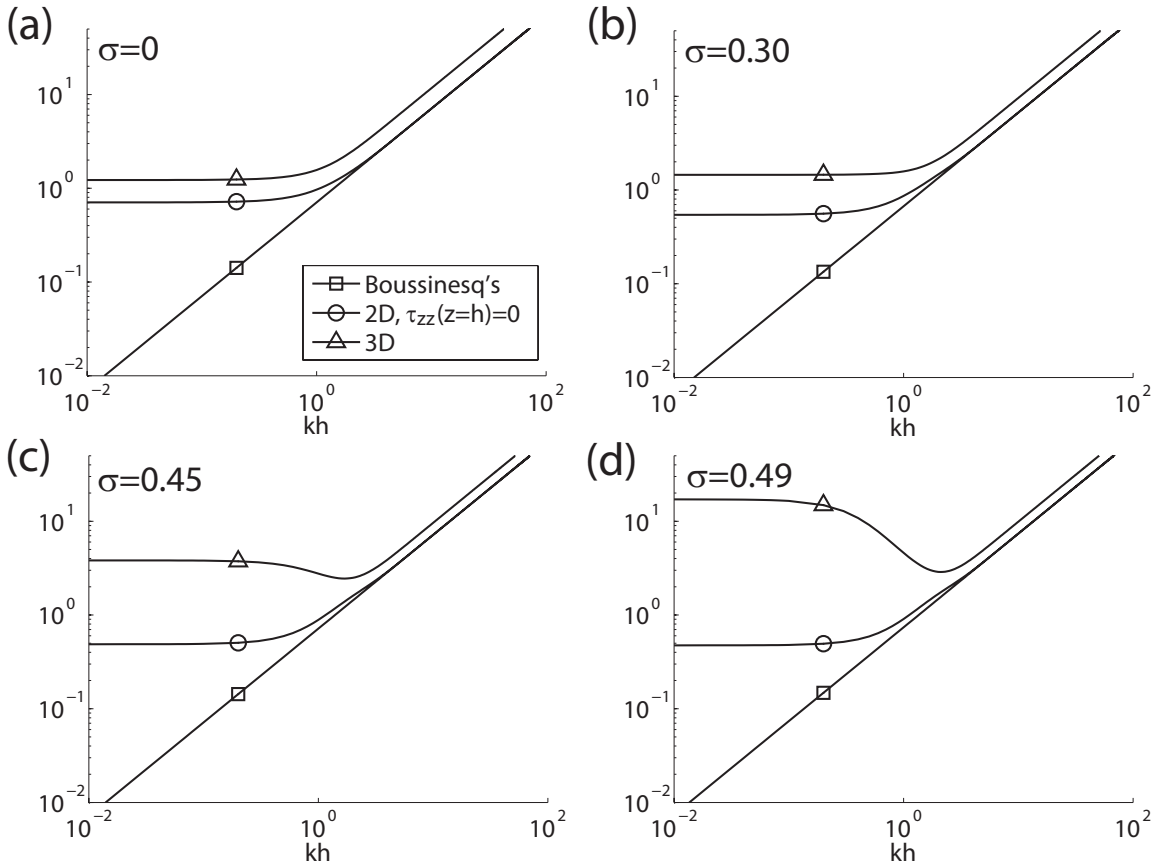

Figure 2.10: Spectral analysis of our 3D, 2D solution for substrates of finite thickness, and Boussinesq's solution of the elastostatic equation, for Poisson's ratio, $\sigma = 0$ (panel a), 0.30 (panel b), 0.45 (panel c), and 0.49 (panel d). The curves represent the Frobenius norm of the transfer matrix (see Eq. 2.72) of our 2D (circles) and 3D (triangles) solution for finite thickness substrates, and Boussinesq's solution (squares).

2.6 Effect of the assumption that vertical traction stresses are negligible in the calculation of the traction stresses

Most of the works studying the traction forces exerted by cells on a flat substrate assume that the vertical stresses at the free surface are negligible, that is, that cells only exert tangential stresses [28, 33–35]. However, there is recent evidence in the literature showing that the vertical stresses exerted by cells can in some cases be comparable to the tangential stresses [96–98]. Given the wide use of 2D traction force cytometry techniques, we will proceed in this section to quantify the error that these methods involve with respect to 3D techniques.

Fig. 2.10 displays the spectral analysis of the 2D and 3D solutions of the elastostatic

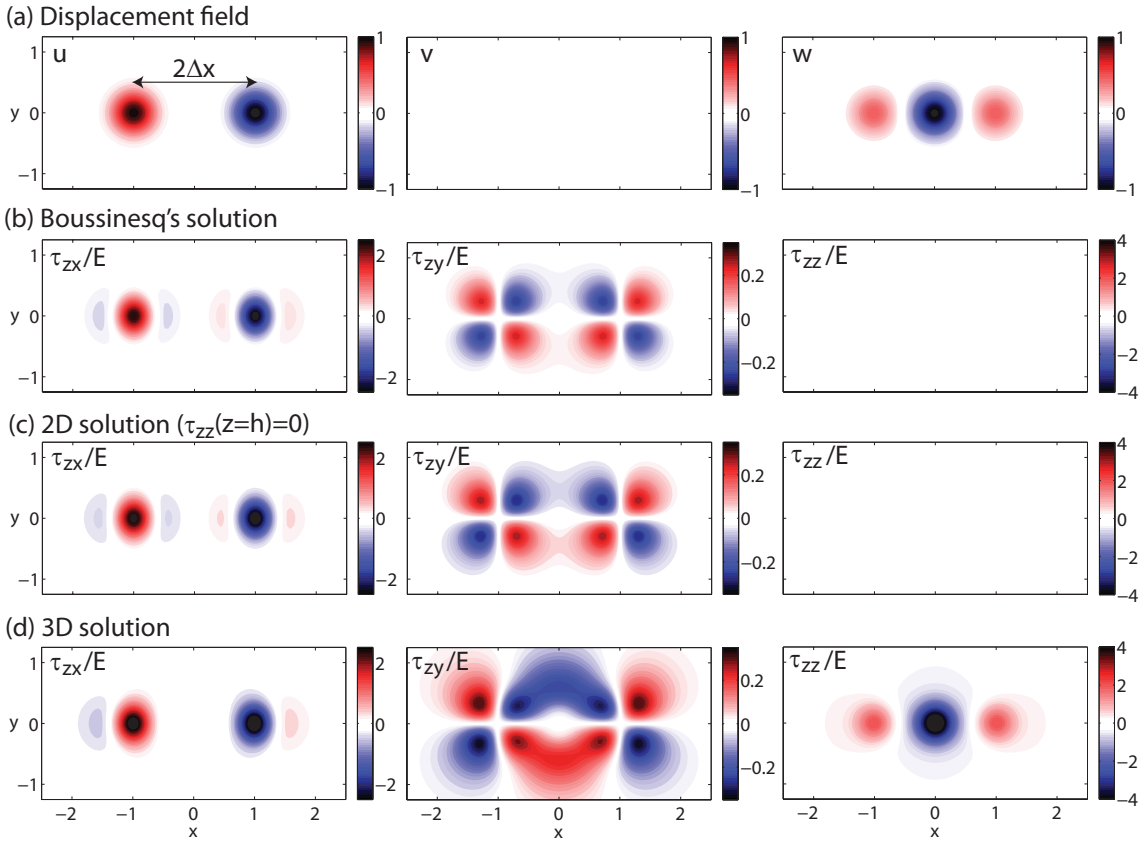

Figure 2.11: Comparison between our 3D, 2D solution for substrates of finite thickness and Boussinesq's solution of the elastostatic equation for a synthetic displacement field. (a) Synthetic displacement field applied at the substrate free surface: u (left panel), v (central panel), w (right panel). (b) For Boussinesq's solution, (c) our 2D solution, and (d) our 3D solution for finite thickness substrates: traction stresses at substrate free substrate associated with the displacement field in panel a. The separation between adhesion regions is $2\Delta x$, substrate thickness $h = 0.5\Delta x$, and Poisson's ratio $\sigma = 0.45$ ($\Delta x = 1$).

equation for finite thickness substrates. This figure shows that, as expected, the 2D and 3D solutions differ for all wavenumbers, given that the determination of the vertical stresses is absent in the 2D method. For high wavenumbers, $kh > 3$, the relative difference between these two solutions remains constant, decreasing as the Poisson's ratio σ approaches 0.5, corresponding to an incompressible material. For low wavenumbers, $kh \lesssim 3$, the differences between the 2D and the 3D solution increase, being maximal as σ approaches 0.5.

Fig. 2.11 shows a comparison between these three methods for a synthetic displacement field representative of the 3D displacement pattern exerted by cells [96–98]. The pattern of tangential stresses in the longitudinal direction, τ_{zx}, obtained from each of the three methods do not differ substantially from each other (Fig. 2.11b-d, left panel). Quantification

of the relative differences in peak stresses shows that Boussinesq's solution underestimates τ_{zx} in 12%, and our 2D solution in 6% with respect to our 3D solution. The pattern of tangential stresses in the lateral direction, τ_{zy}, shows larger discrepancies (Fig. 2.11b-d, central panel). Boussinesq's and our 2D solution underestimate the peak in τ_{zy} by 23% and 16% respectively, but since the magnitude of the lateral stresses is small compared with the longitudinal and vertical stresses (see colorbars in Fig. 2.11b-d) these differences have a reduced effect in the overall stress pattern. As expected, the error in the vertical stresses is 100%, since Boussinesq's and our 2D solution do not capture them (Fig. 2.11b-d, left panel).

2.7 Discussion

Several methods have been used in the past to calculate the traction forces exerted by cells during locomotion over flat substrates [27–29, 31, 33]. Since its introduction by Butler et al. [33], Fourier traction cytometry has been one of the most popular ones. As an improvement over Butler's method, we have presented in this section a Fourier traction cytometry method which considers the effect of the finite thickness of the substrate.

Both the thickness, h, and the Poisson's ratio, σ, of the substrate significantly affect the calculation of the cell traction stresses for lengthscales larger than $2h$. This implies their relevance for the study of collective cell migration, since an important component of the traction forces exerted by a layer of cells corresponds to the size of the layer [99], typically much larger than the substrate thickness, h.

Our study shows that, regardless of the inaccuracy in the assumption that vertical traction stresses at the substrate free surface are negligible, the calculation of the tangential traction stresses using our 2D Fourier traction cytometry technique does not deviate significantly from our 3D technique ($\approx 10\%$ error in magnitude, and similar stress pattern). However, the presence of significant vertical stresses unveils an additional level of complexity in the mechanical interactions cell-substrate. The results by Hur et al. [96], Maskarinec et al. [97] and del Álamo et al. [98], which show that a cell pushes the substrate at its center and pulls it at its periphery, support the existence of a scaffold of actin fibers going over the cell nucleus [100] and attaching to the substrate at the periphery of the cell [101] at a certain angle. The presence of this type of actin structure is in agreement with studies which relate cell shape, nucleus deformation, and the actin cytoskeleton [102], and would explain the exertion of vertical forces, suggesting that it is the cell nucleus, reported to be stiffer than

the cell body [101, 103, 104], which pushes the substrate downwards, suffering deformation. The deformation of the cell nucleus has been related to signalling processes altering cell behavior [105–107], and its consequences for cell migration will need to be understood.

Chapter 2, in part, have been published in the *Proceedings of the National Academy of Sciences of the United States of America*, "Spatio-temporal analysis of eukaryotic cell motility by improved force cytometry," by J. C. del Álamo, R. Meili, B. Alonso-Latorre, J. Rodriguez-Rodriguez, A. Aliseda, R. A. Firtel, and J. C. Lasheras (2007) 104:13343-13348, in the *Conference Proceedings of the IEEE Engineering in Medicine and Biology Society*, "Distribution of traction forces associated with shape changes during amoeboid cell migration," by B. Alonso-Latorre, R. Meili, E. Bastounis, J. C. del Álamo, R. A. Firtel, and J. C. Lasheras (2009) 2009:3346-3349, and is in preparation for submission for publication, "Three-dimensional traction cytometry in amoeboid cells," by J. C. del Álamo, R. Meili, B. Alonso-Latorre, Álvarez B., R. A. Firtel, and J. C. Lasheras (2011). The thesis author is a co-author in the first publication and the primary investigator in the second and third publications.

Experiments were performed by Dr. R. Meili in the Section of Cell and Developmental Biology, University of California, San Diego. This investigation was partially funded by the U.S. National Institutes of Health.

Chapter 3

Quantitative Study of the Mechanics of Amoeboid Motility

Despite the enormous recent advances in our knowledge about the biochemical processes controlling cell motility, our understanding of the spatiotemporal coordination of the mechanical processes on the cellular scale remains limited. Current approaches to this question are based on the measurement of parameters such as cell shape or traction forces and the analysis of their changes in different mutant strains with altered biochemical properties [20, 21, 34, 47, 79, 108–110]. Cells are plastic and dynamic objects, which makes capturing and describing their entire range of motion and shapes challenging [15]. Additionally, there is a substantial level of variability in the properties of individual cells, even in a clonal population [22]. A common way to ameliorate this problem is to select a limited number of cells that can represent the population. However, the identification of such "prototypical" cells is subjective and is often lacking statistical validation.

In the present chapter, we use the improved Fourier traction cytometry method presented in Chapter 2 to study the underpinnings of the motility cycle of single *Dictyostelium* cells moving up a chemoattractant gradient for three strains: *WT* (wild type, KAx-3), MyoII essential light chain null ($mlcE^-$; with altered MyoII motor function, see Section 3.12), MyoII null ($mhcA^-$; lacks MyoII cross-linking and motor function), and talin A null cells ($talA^-$) (obtained from M. A. Titus, University of Minnesota, Minneapolis, MN). We find that these cells produce much larger contractile forces than needed to overcome the resistance from their environment. We show that the chemotactic migration of single, isolated *Dictyostelium* cells is made up of a repetitive sequence of canonical steps. Our analysis of

the temporal evolution of the length of the cell and the strain energy transmitted to the substrate as well as of the area fluxes (defined in Section 3.1.5) shows that these quantities vary periodically. Taking advantage of the periodicity of the cell migration cycle we have implemented a novel statistical methodology that systematically allows us to dissect the motility cycle into four canonical phases (protrusion, contraction, retraction and relaxation), and compute average maps of traction forces for each phase. We have also applied this analysis to the area fluxes that arise when the cells move. The development of this conditional sampling technique enabled us to systematically compile large data sets of high-resolution time-lapse recordings of shapes and traction forces during chemotaxis and obtain a statistically-significant quantification of the spatiotemporal distribution of the traction forces the cell exerts at the different stages in the motility cycle. We have used this approach to compare the motility characteristics of *WT* and mutant strains with impaired MyoII function. We then relate the molecular properties of MyoII with the spatiotemporal organization of the traction stresses, and analyzed how these stresses govern the motility cycle [40, 65, 71, 73, 75, 111–113]. We also demonstrate a remarkably strong correlation between the mean velocity of the cells and the period of the strain energy cycle, which persists for mutants with adhesion and contraction defects. Our studies provide new insight into the molecular basis of MyoII function for cellular organization, in particular, how the cross-linking and motor properties of MyoII affect the spatiotemporal distribution of traction forces and the ability of cells to move. These insights should be applicable to a wide range of cell types.

3.1 Statistical tools

We used conditional statistics to characterize the average traction stresses exerted by *WT*, $mlcE^{-}$, and $mhcA^{-}$ cells during different phases of their motility cycles. These phase averages were calculated from instantaneous maps of traction stresses after arranging the experimental time-lapse data series by phases.

3.1.1 Dissection of the different phases of the motility cycle

The sorting procedure of the different stages of the motility cycle had three steps as sketched in Fig. 3.10a. First, we recorded the quasi-periodic time evolution of the length of the cell, $L(t)$. Second, a human user selected the peaks and valleys of each time history of $L(t)$. Third, a computer algorithm automatically divided each cycle of $L(t)$ into the phases

during which the cell length is increasing (phase 1, protrusion), is near to a local maximum (phase 2, contraction), is decreasing (phase 3, retraction), or is near to a local minimum (phase 4, relaxation). This algorithm worked by applying the following adaptive threshold on $L(t)$

$$Phase(t) = \begin{cases} 1 \text{ if } \gamma(L_{max} - L_{min}) < L(t) - L_{min} < (1-\gamma)(L_{max} - L_{min}) \text{ and } t_{min} < t < t_{max}, \\ 2 \text{ if } |L(t) - L_{max}| < \gamma(L_{max} - L_{min}), \\ 3 \text{ if } \gamma(L_{max} - L_{min}) < L(t) - L_{min} < (1-\gamma)(L_{max} - L_{min}) \text{ and } t_{max} < t < t_{min}, \\ 4 \text{ if } |L(t) - L_{min}| < \gamma(L_{max} - L_{min}), \end{cases} \tag{3.1}$$

where t_{min} and t_{max} are the instants of time associated with the nearest local minimum and maximum of $L(t)$, and $L_{min} = L(t_{min})$ and $L_{max} = L(t_{max})$. Once a phase had been assigned to each time-point of our time-lapse experiments, we calculated the average maps of traction stresses based on the conditions that $Phase(t) = 1, \ldots, 4$. Note that the threshold needs to be $0 < \gamma < 0.5$ in order to avoid overlap of adjacent phases. Figs. 3.10, 3.13 and 3.15 were calculated using $\gamma = 0.2$. The selection of a threshold for separating the motility cycle into stages was shown to have a negligible effect on the phase-averaged traction maps. To check whether our results are independent of γ, we re-calculated Fig. 3.14 for values of the threshold parameter lower and higher than $\gamma = 0.2$. The resulting stress maps (Fig. 3.14) are highly similar to those in Fig. 3.13, confirming that our results are robust irrespective of the threshold.

3.1.2 Phase-averaged traction stresses

Mathematically, we define the average map of traction stresses corresponding to the i-th phase of the motility cycle of a set $j = 1, \ldots, N$ of cells, using M_j temporal observations for the j-th cell, as

$$\langle \boldsymbol{\tau} \rangle_i^N(\xi, \eta) = \frac{\sum_{j=1}^{N} \sum_{k=1}^{M_j} W_i^j(t_k)\, \boldsymbol{\tau}^j(\xi, \eta, t_k)}{\sum_{j=1}^{N} \sum_{k=1}^{M_j} W_i^j(t_k)} \tag{3.2}$$

where, (ξ, η) are the spatial coordinates and $\boldsymbol{\tau}^j(\xi, \eta, t_k)$ is the instantaneous traction stress field generated by the j-th cell at time t_k. The weight function $W_i^j(t_k)$ is set equal to 1 when the j-th cell is in the i-th phase of the motility cycle at time $t = t_k$ and equal to zero otherwise. In the results section, we show that, when N becomes sufficiently large, $\langle \boldsymbol{\tau} \rangle_i^N$

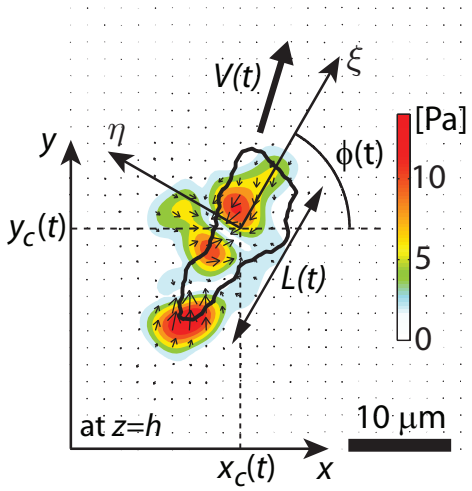

Figure 3.1: Representation of the cell-based reference system in which both traction stresses and shape of the cell are expressed. The black contour indicates the instantaneous contour of the cell, of length $L(t)$. The laboratory reference frame is indicated by axes (x, y). The axes of the cell-based reference frame (ξ, η) are centered at the instantaneous centroid of the cell $(x_c(t), y_c(t))$ and are aligned with its minor and major axes, which lie at an angle $\phi(t)$ with respect to (x, y). The colormap and arrows indicate respectively the strength, in Pa, and the direction of the traction stresses exerted by the cell on the substrate. The thick black arrow indicates the direction of motion of the cell, moving with velocity $V(t)$. The scale bar indicates 10 µm.

converges to a uniquely defined function characteristic for each cell line, independent of the particular cells used to compile the average.

3.1.3 Cell-based coordinate system

Before computing the phase averages, we converted the instantaneous traction stress fields into a cell-based, dimensionless coordinate system (ξ, η) that took into account that the shape and the orientation of the cells was changing and could adapt to these changes (Fig. 3.1). The cell-based representation involves aligning the longitudinal axis of the cell with the horizontal (ξ) axis and re-scaling the coordinates with the half-length of the cell. This coordinate system allowed us to compile statistics coming from different cells at different instants of time. The origin of the cell-based coordinate system was located at the instantaneous centroid of each cell, whose instantaneous coordinates in the laboratory frame were $(x_c(t), y_c(t))$. The (ξ, η) coordinates were expressed mathematically as

$$\begin{aligned} \xi &= [(x - x_c(t)) \cos\phi(t) + (y - y_c(t)) \sin\phi(t)]/[L(t)/2] \\ \eta &= [(y - y_c(t)) \cos\phi(t) - (x - x_c(t)) \sin\phi(t)]/[L(t)/2] \end{aligned} \tag{3.3}$$

where x and y were the coordinates in the laboratory reference frame, and $\phi(t)$ was the angle between the longitudinal axis of the cell and the x axis of the laboratory reference frame. Because the distances were scaled with the instantaneous half-length of the cell, $L(t)/2$, in the cell-based reference frame, the longitudinal axis of the cell always spanned from $\xi = -1$ to $\xi = 1$. The dimensions of the traction stresses in this coordinate system need to be consistent with the fact that their surface integral is a force. Because ξ and η are non-dimensional, these traction stresses are scaled with $(L(t)/2)^2$ and therefore, they have dimensions of force (e.g. pN per unit non-dimensional area).

3.1.4 Phase-averaged cell shape

In order to calculate the phase-averaged contour of the cell, we applied the procedures described above (phase conditioning, aligning, scaling and averaging) to a scalar function $p^j(\xi, \eta, t)$ so that, at each instant of time, $p = 1$ inside the two-dimensional projection of the cell and $p = 0$ outside of it. The conditional average of this function for a set $j = 1, \ldots, N$ of cells (calculated similar to the average traction stresses of Eq. 3.1, $\langle p(\xi, \eta) \rangle_i^N$, yielded the probability that a given point belonged to a cell during the i-th phase of the motility cycle in cell-based coordinates. We defined the phase-averaged contour of the cell as the iso-contour $\langle p(\xi, \eta) \rangle_i^N = pav_i^N$ that enclosed an area equal to the average area of the cell during the same phase. Fig. 3.2 illustrates the calculation of the average cell outline by showing a contour map of $\langle p(\xi, \eta) \rangle_i^N$ measured for the protrusion phase of WT cells, and the resulting average cell contour, which corresponds to the probability level that encloses an area equal to the average area of all cells in this case, $pav_i^N = 41\%$. Because pav_i^N corresponds to a non-zero probability, it is expected that the instantaneous contour of a given cell does not match the average cell contour due to variability in cell shape. In particular, the instantaneous contour of a given cell often exceeds the average cell contour in some locations. When this occurs, the cell may instantaneously exert traction stresses outside of the average cell outline, which can account for the small, non-zero values of the average stresses outside the average contour observed in Figs. 3.13 and 3.14. This statistical effect is caused by the natural variability of cell shape and is observed even when the instantaneous traction stresses outside of the instantaneous cell outline are forced to be zero by using a constrained traction cytometry method (see Section 3.11).

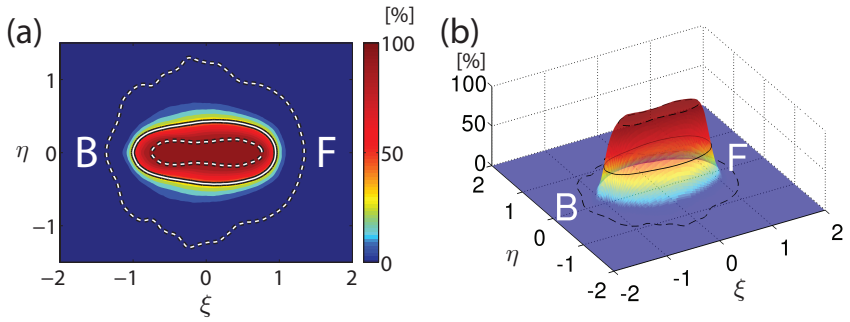

Figure 3.2: Determination of the phase average contour of the cell. (a) Two-dimensional contour map of the probability $\langle R(\xi,\eta)\rangle_i^N$ that a point belongs inside a WT cell in cellbased coordinates (Eq. 3.3) for $N = 31$ cells and $i = 1$ (protrusion phase). The dashed lines represent the probability levels 0% and 95%. The solid line represents the probability level that encloses an area equal to the average area of WT cells during the protrusion stage, which in this case is pav_i $N = 41\%$. Because it conserves the average area of the population, this contour has been chosen as the average outline of the cell. The labels "F" and "B"indicate respectively the front and back of the cell. (b) Three-dimensional representation of the probability map shown in (a). The arrows shown at zero level indicate the magnitude and direction of the average traction forces and have been included for reference.

3.1.5 Area fluxes

The differential area flux at each element of area of the plane is defined as the rate of change of the probability that the considered element belongs inside a cell weighted with the differential area of the element

$$dAF = \frac{p(\xi,\eta,t_k) - p(\xi,\eta,t_{k-1})}{t_k - t_{k-1}} \left[L(t_{k-1})/2\right]^2 \, d\xi \, d\eta \tag{3.4}$$

where (ξ,η) are calculated from Eq. 3.3 with respect to $x_c(t_{k-1})$ and $y_c(t_{k-1})$ and $L(t_{k-1})$ both for $p(\xi,\eta,t_{k-1})$ and $p(\xi,\eta,t_k)$. According to the definition of p given above, $p(\xi,\eta,t_k) - p(\xi,\eta,t_{k-1})$ will be equal to 1 wherever the cell has gained area, -1 wherever the cell has lost area, and 0 if the cell was present at both times t_{k-1} and t_k. Therefore, the integral $AF = \int dAF$ in a region of the (ξ,η) plane represents the change of cell area measured in that region per unit time: if $AF > 0$ in a certain region of space, then the cell is adding material at that region and vice versa.

3.2 Quantitative evidence for a regulated motility cycle

Fig. 3.3 shows a characteristic time series of images exemplifying the distinct stages that constitute one representative motility cycle of *WT Dictyostelium* cells. The strain

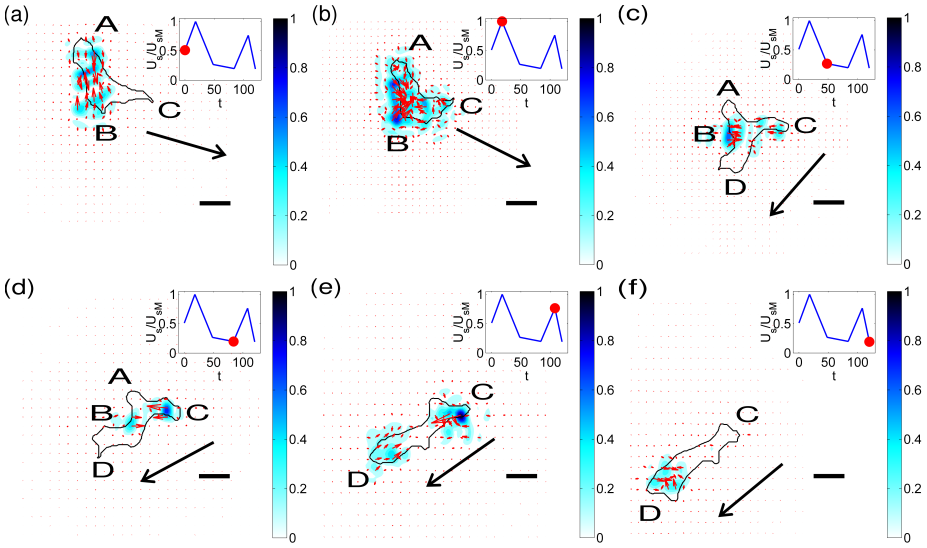

Figure 3.3: Sequence of images of a moving *WT Dictyostelium* cell. The black contour is the outline of the cell. The color contours map the magnitude of the stresses produced by the cell relative to their maximum value. The red arrows indicate the magnitude and direction of these stresses. The plot at the upper right corner of each panel indicates the strain energy of the substrate for the selected images. The red circle in that plot indicates the instant of time that corresponds to each panel: (a) $t = 0$ s; (b) $t = 18$ s; (c) $t = 48$ s; (d) $t = 84$ s; (e) $t = 100$ s; (f) $t = 112$ s. (Scale bars: 10 µm.) The arrow indicates the direction of motion of the cell.

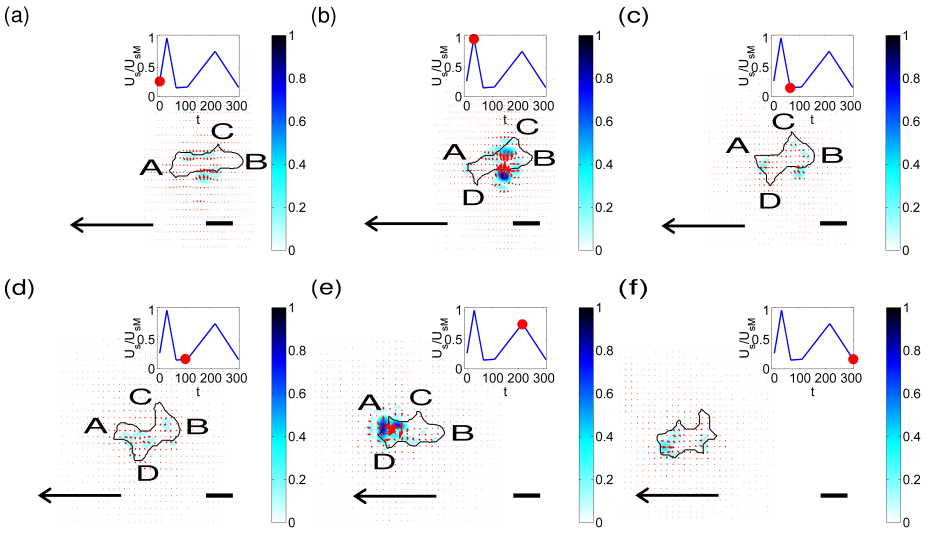

Figure 3.4: Sequence of images of a chemotaxing *mhcA*$^-$ *Dictyostelium* cell, similar to Fig. 3.3. (a) $t = 0$ s. (b) $t = 28$ s. (c) $t = 64$ s. (d) $t = 100$ s. (e) $t = 216$ s. (f) $t = 308$ s.

energy imparted by the cell on the substrate (denoted U_S, see Eqs. 2.15 and 2.16) is also shown on each panel. Note that U_S is approximately periodic, showing successive peaks and valleys (also see Fig. 3.5). While quasi-periodic behaviors in the velocity and shape of migrating *Dictyostelium* cells have been reported previously [79, 114] our findings provide strong evidence that the level of force transmitted by the cell to the substrate reflects the regulation of the cell motility cycle.

In Fig. 3.3a, the cell is transmitting its internal tension to the substrate through two discrete attachment regions at A and B, while it protrudes a pseudopod at C without producing discernable stresses underneath. The convergence of stresses from two principal areas is a prevalent pattern (Figs. 2.7 and 3.3b-f) indicating that the cell is prestretched, consistent with the basic motility model of Lauffenburger and Horwitz [1]. The pseudopod at C then attaches to the substrate $\approx$ 20 s later (Fig. 3.3b), leading to an increase of the stresses and U_S. The increase in U_S seems to trigger the detachment of the back of the cell at A (Fig. 3.3c), which starts a gliding retraction with a subsequent decrease in strain energy. At the same time, a new pseudopod forms at D and glides forward over the substrate. During this phase, which lasts $\approx$ 30 s, the attachment at B weakens, and U_S decreases further (Fig. 3.3d). When the cell finally detaches from B (Fig. 3.3e), the pseudopod at D attaches to the substrate and U_S rises steeply. Following this event, the cell detaches from C and starts a gliding retraction (Fig. 3.3f) that leads to a sudden decrease in U_S, similar to the transition between Figs. 3.3b and c. This quasi-periodic sequence of cell attachment/detachment and force generation is observed in all moving, *WT* cells and correlates well with the time evolution of the strain energy. Consistent with this result, Uchida et al. [79] observed correlation between the cyclic variation of the cell area and the displacement patterns of beads embedded in the substrate. These authors proposed a motility cycle consisting of two phases in which the cell contracts and extends the substrate alternatively. However, in our experiments we never observed any expanding stress pattern, just contractile ones. This discrepancy may be due to permanent deformations of their substrates.

Fig. 3.4 shows a sequence of images representing the motility cycle of $mhcA^-$ cells together with the evolution of U_S. A first comparison of Figs. 3.3 and 3.4 suggests that the stages of the cycle are less distinct in $mhcA^-$ cells than in *WT* cells. This is observed in all of our experiments. In Fig. 3.4a, the cell is attached weakly to the substrate along its periphery between the front (A) and back (B), and begins to extend a pseudopod at C. The strength of the existing adhesions increases during the following 30 s (Fig. 3.4b), while

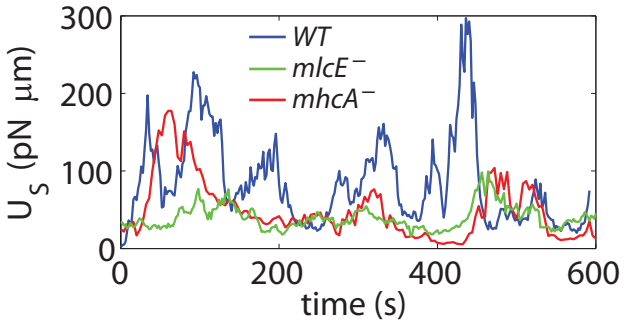

Figure 3.5: Typical time evolution of the strain energy for a *WT* (blue), a *mlcE*$^-$ (green), and a *mhcA*$^-$ (red) cell.

pseudopod C extends and B retracts. Consequently, U_S increases. At the same time, the cell grabs weakly to the substrate near A and protrudes a new pseudopod (D) at its front. Pseudopodia A-D continue gliding while the attachment regions weaken and U_S decays (Fig. 3.4c). After the strain energy has reached a local minimum, pseudopodia A, C, and D continue extending for 40 s in what seems to be a competition to become the dominant protrusion. Eventually, pseudopod A prevails, and the cell slowly retracts pseudopodia B, C, and D (Fig. 3.4e). The strain energy peaks again when A attaches to the substrate. The stress pattern in Fig. 3.4e indicates that the cell is clamping the substrate locally at A. This type of pattern is observed repeatedly in the front of all of the *mhcA*$^-$ cells studied, and differs from the typical stress distribution observed in *WT* cells, which is more coordinated along the whole cell body. In the latter case, the stresses transmitted to the substrate at each attachment region are generally unidirectional and compensate for the stresses transmitted by a different pseudopod (Fig. 3.4). Fig. 3.4f shows the instant when the cell loosens its adhesion to the substrate, and U_S returns to its baseline.

3.3 Effects of cytoskeletal mutations on the strain energy, and magnitude of the pole forces, and migration speed

The statistical analysis of the motility parameters of single *WT*, *mlcE*$^-$, and *mhcA*$^-$ cells yields interesting results (Table 3.1 for *Whole cycle*). Consistent with previous works [67, 111], we find that the average translation velocity V of both *mlcE*$^-$ and *mhcA*$^-$ cells is about half than that of *WT* cells (Table 3.1). The speed of single cells shows little or no correlation with either pole force (see Eq. 2.14) or strain energy (see Eqs. 2.15 and 2.16) (Fig. 3.6). Because the external and inertial forces acting on the cells are much smaller

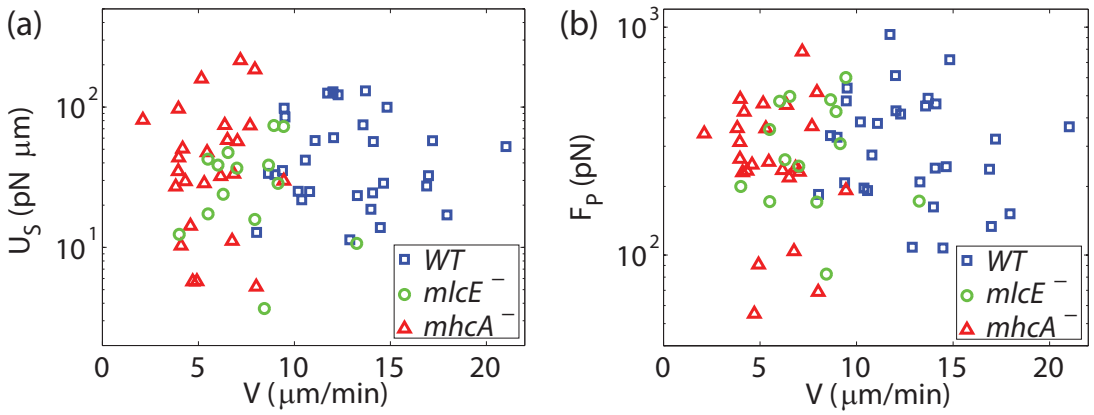

Figure 3.6: Scatter plots of the average velocity of each cell (V) versus the average value of the strain energy (U_S, panel a) or the average magnitude of the pole forces (F_P, panel b). Blue symbols represent WT ($N = 30$), green symbols $mlcE^-$ ($N = 14$), and red symbols $mhcA^-$ cells. ($N = 25$). The data show little correlation between V and U_S or F_P.

than the traction forces measured in our experiments, the front and back pole forces always have approximately the same magnitude. They are generally oriented along the direction of polarization and always display a converging or contractile pattern (see panels on the right of Figs. 2.7b-c). Therefore, they can be used to quantify the level of cytoskeletal tension of the cell along the direction of polarization. The average magnitude of the pole forces transmitted at the attachment regions in the front and back of the cells is $F_p \approx 346$ pN for WT, and $mlcE^-$ and $mhcA^-$ are still able to produce $F_p \approx 350$ pN and $F_p \approx 280$ pN respectively. Not surprisingly, the pole forces and strain energy correlate well with cell area (Fig. 3.7). These results differ from [79], who reported that $mhcA^-$ cells exert much stronger forces on the substrate than WT cells.

Figs. 3.3 and 3.4 demonstrate that the time evolution of the strain energy is a simple, quantitative indicator of the stages of their motility cycle. The graph in Fig. 3.5 compares three representative, 10-min-long time histories of U_S for a WT, a $mlcE^-$, and a $mhcA^-$ cell. The three curves show a quasi-periodic behavior, but the periods of U_S differ. Although U_S rises and decays about 7 times for the WT cell, it only does so about 4 times for both mutant cells. $MhcA^-$ cells have in average longer strain energy periods than both WT and $mlcE^-$ cells, and WT cells present the shortest periods in average.

The average values of U_S for WT, $mlcE^-$, and $mhcA^-$ cells are similar (Table 3.1), although the standard deviations indicate a high variability from cell to cell within the three strains. Together with the different magnitudes observed for the pole forces, this suggests that force production in $mhcA^-$ cells is less coordinated with polarization than in both WT

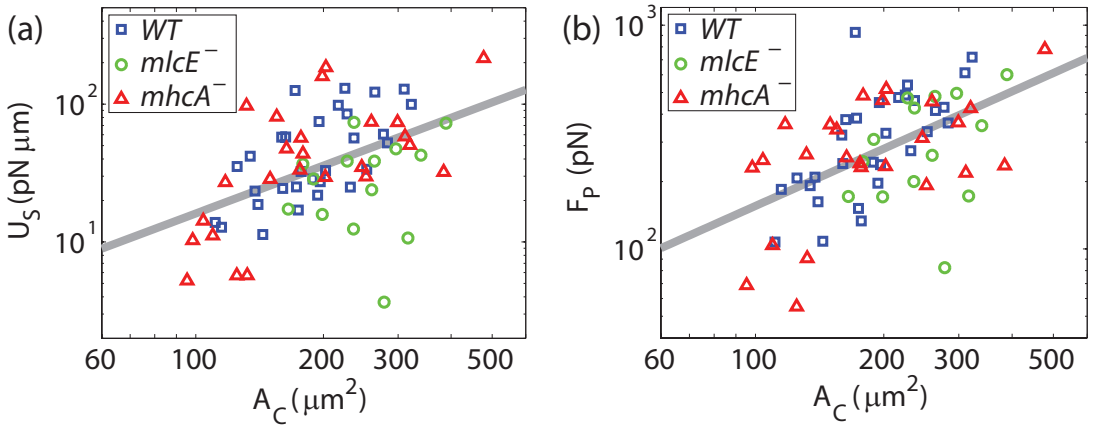

Figure 3.7: Scatter plots of the average projected area of each cell (A_c) versus the average value of the strain energy (U_S, panel a) or the average magnitude of the pole forces (F_P, panel b). Blue symbols represent WT ($N = 30$), green symbols $mlcE^-$ ($N = 14$), and red symbols $mhcA^-$ cells. ($N = 25$). The data show strong correlation between A_c and U_S or F_P. The gray lines are least square fits to the data: $U_S(\text{pN}\mu\text{m}) = 10^{-1.084}\, A_c(\mu\text{m}^2)^{1.1527}$, and $F_P(\text{pN}) = 10^{0.4918}\, A_c(\mu\text{m}^2)^{0.8501}$.

and $mlcE^-$ cells. Under such conditions local stresses may cancel each other out and thus reduce the pole forces while local strain energies always add up in the calculation of U_S (see also Fig. 3.13).

3.4 The mechanical process of amoeboid cell motility is characterized by quasi-periodic changes of cell length and strain energy exerted on the substrate

The quasi-periodic time evolution of both cell length, L, and total strain energy exerted by the cell on the elastic substrate, U_S (Eqs. 2.15 and 2.16), suggests that stereotypical elements of chemotactic cell movement like protrusion or contraction are repeated sequentially (Figs. 3.3, 3.4, 3.5, and 3.8b), consistent with previous observations of other groups on a range of cell types [1, 111, 115].

The existence and degree of periodicity of a force-regulated motility cycle were studied in more detail by analyzing the autocorrelations and crosscorrelation of L and U_S (Fig. 3.8c). The autocorrelation of U_S, $R_{U_S U_S}$, and the crosscorrelation between L and U_S, R_{LU_S}, show a high degree of periodicity and can be used to more unambiguously determine the period of the motility cycle, T. Another important aspect is the duration

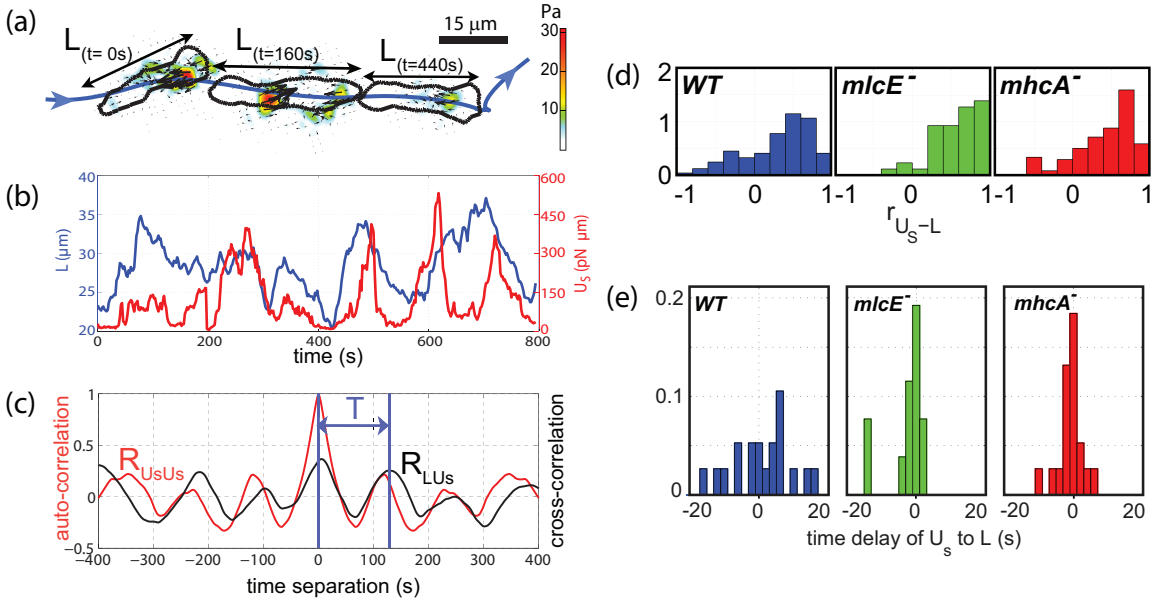

Figure 3.8: Periodicity of amoeboid motility. (a) Outline of a *WT* cell moving left to right at three different instances of time and the corresponding traction stresses it imposes on the elastic substrate. The graph in (b) shows the quasi-periodic time evolution of the length of such a cell (L) in blue and the time evolution of the total strain energy it deposits into the substrate in red (U_S). The graph in (c) further illustrates the periodic nature of the cellular motility process by plotting the cross-correlation between cell length and strain energy (R_{U_SL}) in black and the autocorrelation of the strain energy in red ($R_{U_SU_S}$). (d) Histograms of the correlation coefficients between U_S and L within each motility cycle for *WT* (blue, $N = 31$ cells, 122 cycles), *mlcE*$^-$(green, $N = 14$ cells, 46 cycles), and *mhcA*$^-$ (red, $N = 27$ cells, 119 cycles) cells. (e) Histograms of the phase shift between the peaks of R_{U_SL} and $R_{U_SU_S}$, measured in seconds. The histograms in (d) and (e) are normalized to integrate to unit area.

of the correlation which, in the case of the cell presented in Fig. 3.8, is maintained for 4 complete cycles as indicated by the sustained magnitude of the peaks of $R_{U_SU_S}$ and RLU_S, instead of rapidly decaying to zero as would be expected for an irregular signal. The observed correlations are consistent with the notion that the oscillations in L and U_S are caused by a recurring organized process rather than by random fluctuations. The magnitudes of the peaks for both $R_{U_SU_S}$ and R_{LU_S} are very similar, meaning that U_S is correlated as closely with itself as it is with L. Physically, this means that the cell length and the level of stresses transmitted to the substrate are highly correlated. Although the analysis shown in Fig. 3.8 is for a single *WT* cell, similar periodicity was statistically confirmed for three strains studied. The histograms of the correlation coefficient between U_S and L, r_{U_SL}, for the three strains (Fig. 3.8D) indicate that L and U_S are strongly correlated for the majority

of the *WT*, *mhcA*$^-$, and *mlcE*$^-$ cells analyzed. The percentage of cells showing a correlation coefficient $R_{LU_S} > 0.5$ is 44% for *WT*, 58% for *mlcE*$^-$, and 55% for *mhcA*$^-$ cells. Further evidence is provided by the statistics of the probability of the null hypothesis that U_S and L are independent versus the alternative that they show positive correlation. The percentage of cells with a p-value lower than 0.05 is 58% for *WT*, 89% for *mlcE*$^-$, and 72% for *mhcA*$^-$ cells, which confirms that in the vast majority of cases U_S and L are positively correlated. The histograms of the time delay between the peaks of R_{LU_S} and $R_{U_SU_S}$, shown in Fig. 3.8e, are narrow and symmetric with respect to zero, indicating that the time evolutions of cell length and strain energy are statistically in phase.

3.5 The average speed of migration of *Dictyostelium* cells is determined by the period of their motility cycle

Fig. 3.9a provides quantitative evidence that the average velocity of migration V of a cell is determined by the frequency at which it is able to perform the motility cycle. The relationship between the average velocity of the cell (V) and the period of the strain energy cycle (T) is well approximated by the hyperbola $V\,T = \lambda$, where λ is a constant with units of length (Fig. 3.9a). The correlation coefficient between V and $1/T$ is $R = 0.71$. The probability of the null hypothesis that V and $1/T$ are independent versus the alternative that they show positive correlation, $p = 2.3 \times 10 - 14$, is extremely low. One important aspect of this empirical relationship is that it holds for a wide range of velocities ($2 - 20$ µm/min) and is conserved in mutants we have tested with contractility defects. *WT* cells ($p = 0.0045$) have the fastest velocities and shortest periods, while *mhcA*$^-$ cells ($p = 0.011$) have the slowest velocities and the longest periods and *mlcE*$^-$ cells ($p = 0.0029$) have velocities and periods falling between the ones measured for *WT* and *mhcA*$^-$ cells.

To test the robustness of the above empirical relationship across these three strains, a non-parametric, one-way ANOVA test was performed on the values of λ measured for the *WT*, *mlcE*$^-$, and *mhcA*$^-$ cells. The resulting p-values of the null hypothesis that the distributions of λ from different strains have different averages (p=0.36 for *WT*/*mlcE*$^-$, p=0.22 for *WT*/*mhcA*$^-$ and p=0.97 for *mlcE*$^-$/*mhcA*$^-$) indicate that these distributions are similar. Fig. 3.9b depicts a box-plot of the distributions of λ for *WT*, *mlcE*$^-$, and *mhcA*$^-$ cells. The measured average and standard deviations of λ for *WT*, *mlcE*$^-$, and *mhcA*$^-$ cells are $\lambda = 19.5 \pm 6.0$ µm, 17.6 ± 6.2 µm, and 17.4 ± 4.0 µm, respectively. These values are of the order of the length of the cells, indicating that on average, during each

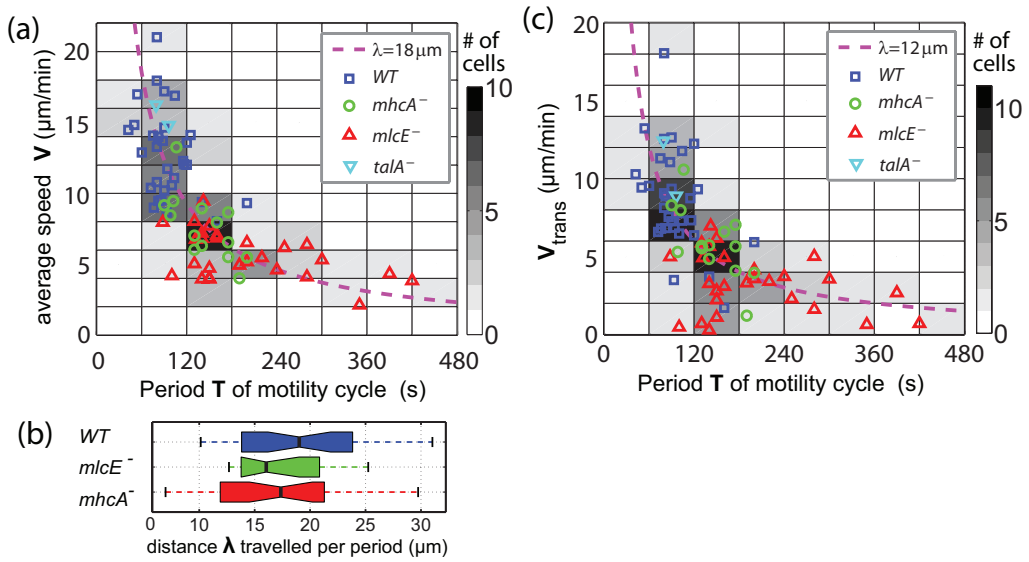

Figure 3.9: *Dictyostelium* motility on gelatin substrates is pace limited. (a) Scatter plot of the average velocity of $N = 74$ chemotaxing *Dictyostelium* cells versus the period of their motility cycle (determined from the time evolution of L). The data points come from four different cell lines: $N = 31$ WT cells (blue squares), $N = 14$ $mlcE^-$ cells (green circles), $N = 27$ $mhcA^-$, and $N = 2$ $talA^-$ cells (cyan triangles). The dashed magenta hyperbola ($V = \lambda/T$) is a least square fit to the data, yielding $\lambda = 18$ μm. The $V - T$ plane has been divided into tiles that have been colored according to the number of cells whose speed and motility period lie within each tile. Darker tiles contain more cells, as indicated in the color. (b) Box plot of the product $V - T$ for WT, $mhcA^-$, and $mlcE^-$ cells. (c) Scatter plot of the continuous translocation velocity V_{trans} (see Eq. 3.7) of the same cells as in (a) versus the period of their motility cycle. The dashed magenta hyperbola ($V_{trans} = \lambda/T$) is a least square fit to the data, yielding $\lambda = 12$ μm.

motility cycle these cells move a distance comparable to their length. This similarity in values of λ suggests that, despite their differences, the implementation of the motility cycle of these three strains should not differ substantially.

We have included in Fig. 3.9a two cells lacking talin A ($talA^-$ cells), a conserved protein that mediates cell adhesion [116], showing that their speed is also well described by the same hyperbolic law. The speed of $talA^-$ cells is comparable to that of WT cells, even though their average pole forces transmitted to the substrate (≈ 200 pN) are lower than those transmitted by $mhcA^-$ cells.

3.6 A phase statistical analysis of the motility cycle provides a unified description of the behavior of *WT* and mutant cells

We developed a statistical method that enables us to determine the spatiotemporal mechanical organization of the average cell during locomotion (Section 3.1). The method first divides the motility cycle into a number of canonical stages (or phases) and then computes the phase-average maps of the traction forces. For this purpose, we developed an unbiased, automatic procedure that is capable of identifying the canonical stages of the motility cycle in each experimental time-lapse record. This is possible for amoeboid cells because they move following a series of well-defined steps that translate into periodic oscillations of L and U_S, as previously discussed. We employed a cell-based reference system with the origin at the instantaneous centroid of each cell and the horizontal axis coinciding with the longitudinal major axis of the cell (see Section 3.1). Comparing sequential time points enabled us to determine the shape changes. We divided the motility cycle into four stages (or bins) according to the criteria indicated in Fig. 3.10a and named these stages based on the properties of the cell at each stage: 1) Protrusion, defined as the fraction of each cycle during which the cell length is increasing; 2) Contraction, defined as the fraction of each cycle during which the cell length is near a local maximum (our force measurements have shown this phase to coincide with maximum strain energy; Fig. 3.8); 3) Retraction, defined as the fraction of each cycle during which the cell length decreases; and 4) Relaxation, defined as the fraction of each cycle during which the cell length is at a minimum (our force measurements have shown this phase to coincide with minimum strain energy; Fig. 3.8). We used the assigned phases to sort the data obtained from different cells at different instants of time and to compile average maps of stress and cell shape. More information about this methodology, including the algorithm for the dissection of the motility cycle into phases and other statistical tools employed in this study, can be found in Section 3.1. Our method is robust, and relatively insensitive to the algorithm used to sort out the four phases of the motility cycle (see Section 3.8.1).

The changes in cell shape during the cycle can be analyzed by determining the area fluxes (for the definition see Section 3.1.5). Fig. 3.11 shows that the described cycle-sorting algorithm is able to dissect the motility cycle of *Dictyostelium* cells into the succession of leading-edge protrusions, formation of new adhesions near the front, cell contraction, release of the rear adhesions, and retraction that has been described phenomenologically

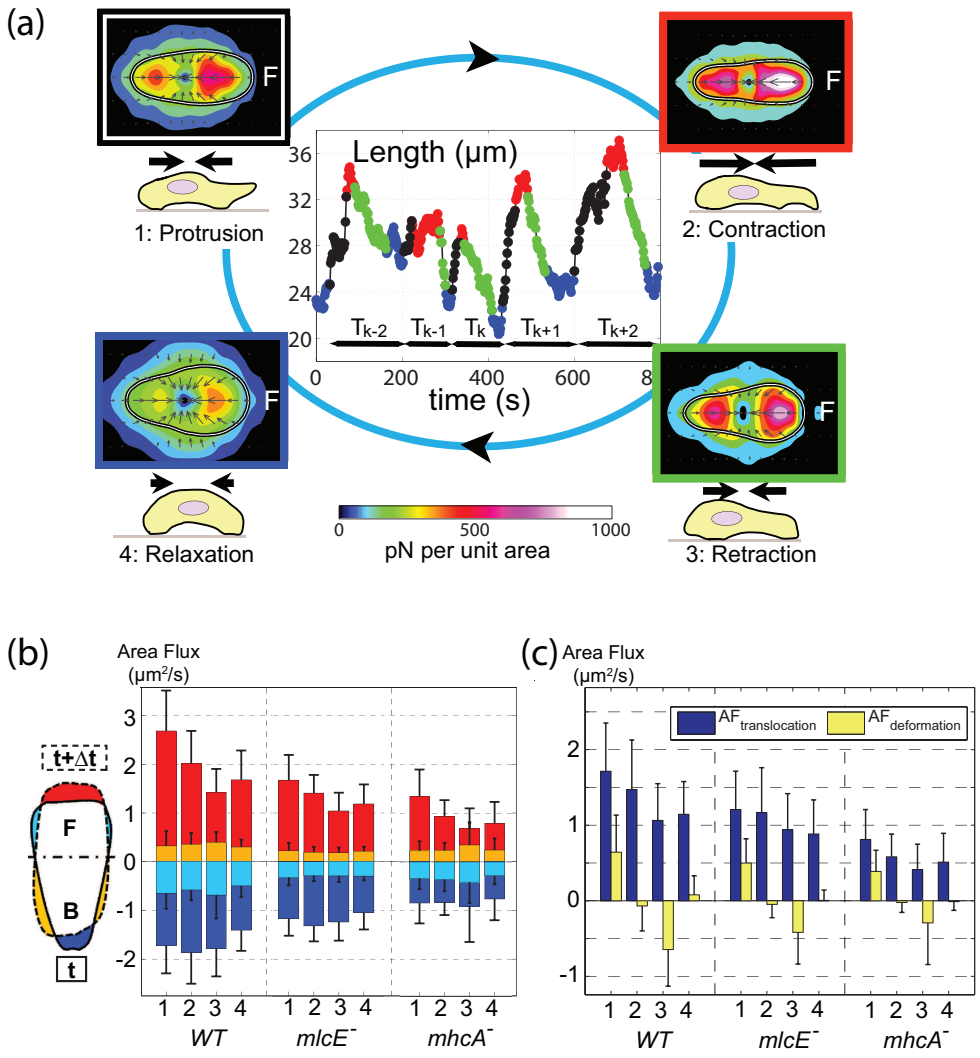

Figure 3.10: Analysis of the four phases of the motility cycle using phase statistics. (a) Assignment of individual time points to the four phases of the motility cycle based on increasing length (black), maximal length (red), decreasing length (green), and minimal length (blue). Normalization yields average stress maps (color map) and cell shape (black-white-black outline) for each phase. The bar plots in (b) show average area fluxes during each phase as determined by phase statistical analysis. The insert sketch represents the contour of a cell at time t (solid line) and at time $t + \Delta t$ (dashed) and illustrates the origin of each of the different area fluxes represented in the bar plots in this panel. Red stands for area increase in the front and yellow for increase in the back. Dark blue stands for area decrease in the back and light blue for area decrease in the front. (c) Area flux due to cell shape change (see Eq. 3.5) in yellow; area flux attributable to continuous translocation in dark blue (see Eq. 3.6).

elsewhere [1]. Fig. 3.11 shows phase-averaged maps of the fluxes (gain/loss) of cell area that occur during cell migration. The red and blue areas in the figure indicate the locations

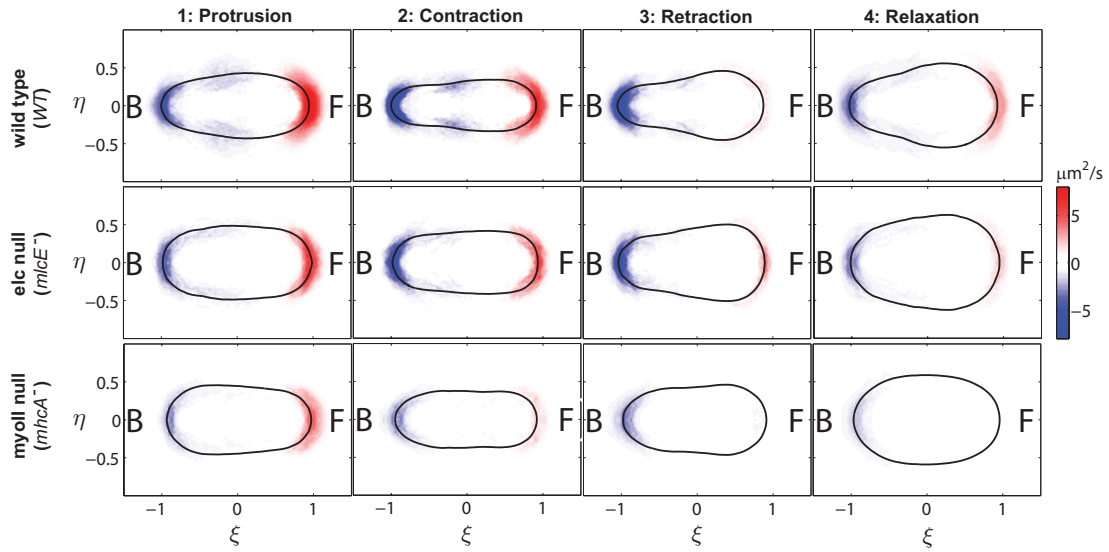

Figure 3.11: Spatiotemporal mapping of the area fluxes in WT and MyoII mutant cells. Phase-averaged area fluxes and cell shape corresponding to the four stereotypical stages defined in Fig. 3.10 for WT (first column, $N = 31$), $mlcE^-$ (second column, $N = 14$), and $mhcA^-$ (third column, $N = 27$) cells. The contour maps show the average area flux field, measured in a reference frame rotated to coincide with the instantaneous principal axes of the cells and scaled with their half-length, $L(t)/2$. The colors indicate the magnitude of the area fluxes in $\mu m^2/s$ (red: positive area flux or gain of cell area; blue: negative area flux or loss of cell area. The black contours show the average shape of the cells in this reference frame. The front "F" of the cell corresponds to $\xi > 0$ and the back "B" corresponds to $\xi < 0$.

where area is being added (red) or depleted (blue) respectively during each of the stages of the motility cycle. The bar plot in Fig. 3.10b shows the integrated positive area flux in the front, AF^+_{front}, the integrated negative area flux in the back, AF^-_{back}, the integrated negative area flux in the front, AF^-_{front}, and the integrated positive area flux in the back, AF^+_{back}. The inset sketch in Fig. 3.10b is a graphical representation of each of these contributions. The absolute values of the integrated area fluxes vary between 1 and 5 $\mu m^2/s$, and are in good agreement with previous measurements of average and instantaneous area gain or loss for single cells ([15, 109, 111, 117]). If a cell simply moved forward while maintaining a constant shape, then AF^+_{front} and AF^-_{back} would have the same magnitude and opposite signs, and the sum of AF^-_{front} and AF^+_{back} would be equal to zero. In reality, amoeboid motility involves an additional component of deformation. To distinguish kinematically between shape preserving translocation and the component of the cell movement that is associated with deformation, we define the area flux of deformation, AF_{defor}, and the area

flux of translocation of the cells, AF_{trans}, as:

$$AF_{defor} = (|AF^{+}_{front}| - |AF^{-}_{back}|) - (|AF^{-}_{front}| - |AF^{+}_{back}|) \tag{3.5}$$

$$AF_{trans} = 1/2\,(|AF^{+}_{front}| + |AF^{-}_{back}|) - 1/2\,(|AF^{-}_{front}| + |AF^{+}_{back}|) \tag{3.6}$$

These parameters are defined so that $AF_{defor} = 0$ when a cell is undergoing shape preserving translocation and $AFtrans = 0$ when the front and back area fluxes are balanced so that the centroid of the cell does not change position. Fig. 3.10c shows a bar plot with the values of AF_{defor} and AF_{trans} for WT, $mlcE^{-}$, and $mhcA^{-}$ cells during the four stages of the motility cycle. This plot confirms that our stage-sorting methodology captures the physical events defining the motility cycle for the three cell lines under study. AF_{defor} indicates that during protrusion, cells, on average, mainly deform by gaining area at the front, while they lose area at the back during retraction. Conversely, the cells undergo little deformation during contraction and relaxation. The substantial contribution of AF_{trans} to each phase means that part of the locomotion of *Dictyostelium* cells occurs independent of deformation or area change on the time scale of the period T. This could potentially be due to events of protrusion/retraction with a period much shorter than T. However, considerably shorter period fluctuations of cell length are absent from the time-lapse movies of individual migrating cells , which suggests a shape preserving translocation due to continuous contraction of the actomyosin network at the back of the cell ([111, 117–119]). To isolate the component of the velocity coming from continuous translation of the cell rather than from its deformation, we have estimated the average velocity of continuous translocation, by dividing the area flux of translocation with the average width of the cell, W. This estimation is expressed as

$$V_{trans} = \left|\frac{AF_{trans}}{W}\right| = \left|\frac{(|AF^{+}_{front}| + |AF^{-}_{back}|) - (|AF^{-}_{front}| + |AF^{+}_{back}|)}{2\,W}\right| \tag{3.7}$$

Fig. 3.9c illustrates that V_{trans} shares the same correlation with the period of the motility cycle as the total cell velocity. This result is expected, as we find that continuous translocation is a substantial contributor to the total velocity of the cell. However, this correlation suggests the existence of a coupling mechanism through which the period T of the cell deformation cycle for the inchworm-like contribution to cell motility is linked to the continuous translocation.

Finally, it should be noted that, although the magnitudes of AF_{trans} and AF_{defor} are lower in $mhcA^{-}$ and $mlcE^{-}$ cells than in WT cells, the time evolution of the parameters for all of the cell lines parallel each other, indicating that the cells from the three strains

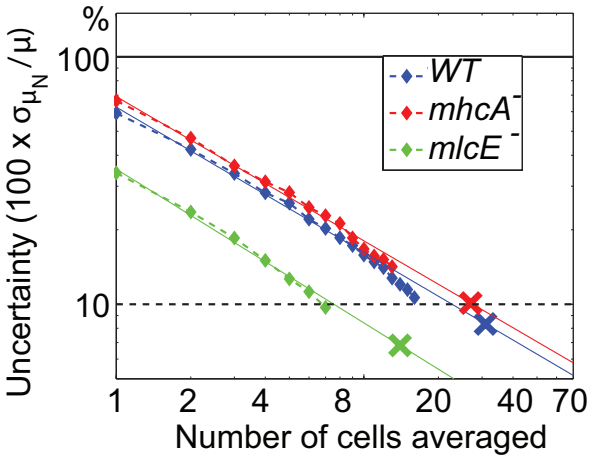

Figure 3.12: Percentage of error (two-dimensional L2 norm) of the phase averaged traction fields as a function of the number of cells compiled in the statistics. Blue, *WT* cells; red, $mhcA^-$ cells; green, $mlcE^-$ cells. The plots show the standard deviations, σ_μ^N, of the distributions of phase-averages μ^N obtained for all possible combinations of N cells that can be formed within a population of $N_{TOT} > N$ cells. The results are normalized with the total average, μ_{TOT}^N, and represented as a function of N. The straight lines are projections of the data from each cell strain. The color crosses on the projections correspond to $N = N_{TOT}$ (N_{TOT} = 31, 14, and 27 for *WT*, $mlcE^-$ and $mlcE^-$ cells, respectively). These crosses therefore estimate the uncertainty of the phase averages in Fig. 3.13.

implement the motility cycle in a similar manner, despite the defects in actomyosin contractility of the mutants. This result is consistent with the observation noted above that all of the cell lines have similar values of λ, the distance moved per cycle (Fig. 3.9).

3.7 Measurements of individual cells are variable but the phase averages converge rapidly and reproducibly

For any sample of cells, the statistical significance of the cell-based phase averages introduced in Section 3.1 is limited by sources of uncertainty such as cell-to-cell variability, measurement errors, or the reproducibility of the experimental conditions. These random contributions eventually cancel out as one increases number N of measured cells. Fig. 3.12 quantifies the relative uncertainty of the phase-averaged traction stresses defined in Eq. 3.2 as a function of N. We estimate this uncertainty from the ratio

$$\nu_i^N = \frac{\sigma_i^N}{\mu_i} = \left\{ \frac{\sum_{l=1}^{K} \int \left[\left\{ \langle \boldsymbol{\tau} \rangle_i^N(\xi,\eta) - \langle \boldsymbol{\tau} \rangle_i^{N_{TOT}}(\xi,\eta) dS \right\} \right]^2}{K \int \left[\langle \boldsymbol{\tau} \rangle_i^{N_{TOT}}(\xi,\eta) \right]^2 dS} \right\}^{1/2} \tag{3.8}$$

where $\langle \boldsymbol{\tau}(\xi,\eta)\rangle_i^N$ is the average traction stress field for the i-th phase of the motility cycle, and $\int() dS$ represents a surface integral in the cell-based coordinate system. The numerator of Eq. 3.8, σ_i^N, is the standard deviation of the distribution $\{\langle \boldsymbol{\tau}(\xi,\eta)\rangle_i^N\}$ of the i-th-phase average traction stresses obtained for all the subsets of N cells (a total of K) that exist within in a set of $N_{TOT} > N$ cells [i.e. for $N = 2$ cells and $N_{TOT} = 3$ cells, we would calculate $K = 3$ partial averages with cells $(1,2)$, $(2,3)$, and $(1,3)$, and compare them with the total average obtained with cells $(1,2,3)$]. We note that σ_i^1 is the standard deviation of the distribution of instantaneous traction stresses observed on single cells. The denominator of Eq. 3.2, μ_I, represents the average traction stresses for the i-th phase and is used to normalize σ_i^N, so that ν_i^N indicates the variability of $\langle \boldsymbol{\tau}(\xi,\eta)\rangle_i^N$ relative to its expected value.

Eq. 3.2 is a precise estimation of the uncertainty of the measurements only when $N_{TOT} \gg N$ and the average, $\langle \boldsymbol{\tau}(\xi,\eta)\rangle_i^{N_{TOT}}$, can be considered as "exact" in comparison with $\langle \boldsymbol{\tau}(\xi,\eta)\rangle_i^N$. However, N_{TOT} is necessarily limited in practice by the finite number of experiments performed, which in our case is $N_{TOT} = 31$, 14 and 27 for *WT*, *mlcE*$^-$, and *mhcA*$^-$ cells. For this reason, we have only plotted ν_i^N for $N < N_{TOT}/2$ in Fig. 3.12. Even for these moderate numbers, the combinations that need to be considered for the calculation of σ_i^N are overwhelmingly large, so we have estimated this quantity by performing a Monte-Carlo simulation with $n = 1000$ iterations. The result shows that the relative uncertainty of $\langle \boldsymbol{\tau}(\xi,\eta)\rangle_i^N$ decreases with the number of cells as $\sigma_i^N/\mu_i \propto N^{-1/2}$, as expected for the standard deviation of the sum of independent statistical distributions [120]. The accuracy of the phase-averaged traction stresses given in this paper can be estimated by extrapolating the $\nu_i^N \propto N^{-1/2}$ behavior to $N = N_{TOT}$. This extrapolation yields the colored crosses in Fig. 3.12, which correspond respectively to $\nu_i^N = 10\%$ for the three cell lines. A similar extrapolation can also be carried out to estimate the number of cells that would be necessary to reach any desired level of statistical convergence. For instance, Fig. 3.12 indicates that $\nu_i^N = 30\% - 70\%$ for $N = 1$, implying that observations made on the basis of single-cell traction maps have a high inherent uncertainty, which makes the need for statistical analysis obvious.

3.8 MyoII is required for the proper spatial organization of the traction stresses

Comparison of the contour and traction stress maps of *WT*, *mlcE*$^{-}$, and *mhcA*$^{-}$ cells should provide insights into the different function of MyoII in controlling the distribution of traction forces during the chemotaxis motility cycle. Fig. 3.13a includes contour maps of the phase averaged traction stresses generated by these three strains during the four stereotypical phases as defined in this study: protrusion, contraction, retraction, and relaxation. In all strains, the cells contract from the periphery inward towards the cell center throughout the cycle, as indicated by the black arrows. It should be noted that Fig. 3.13 shows *average* maps of traction forces and *average* cell contours. Because the instantaneous contour of the cell does not need to be equal to the average contour, it is perfectly possible to observe non-zero average traction stresses outside of the average cell contour (for more details, Section 3.11).

WT cells produce the highest traction stresses (see colormap), which are concentrated in two well-defined areas in the front and the back of the cell and which most likely correspond to the two discontinuous regions of cell substrate adhesion observed by [78]. The overall spatial distribution of stresses in *mlcE*$^{-}$ cells is similar to that of *WT* cells, although their magnitude is lower by a factor of ≈ 2. MyoII motor activity has been proposed to be mostly abrogated in *mlcE*$^{-}$ cells [67], but MyoII still can crosslink F-actin [121]. The integrated pole forces for *WT* and *mlcE*$^{-}$ present similar values, indicating, as visible also in Fig. 3.13, that the traction stresses in *mlcE*$^{-}$ are less focused than in *WT*, suggesting a growth in their area adhesion to compensate for the reduced motor activity of protein MyoII. The stresses produced by *mhcA*$^{-}$ cells, which lack the myosin II heavy chain and thus all MyoII functions, are similar in magnitude to those of *mlcE*$^{-}$ cells. We therefore suggest that the loss/reduction of MyoII-mediated contraction results, unexpectedly, in only modestly depressed peak values of stress, suggesting that similar stress levels can be maintained by other mechanisms. In *mhcA*$^{-}$ cells, the stress pattern is qualitatively different due to not being focused in two separate areas and being situated closer to the cell boundaries than in *WT* or *mlcE*$^{-}$ cells. The differences between the *mhcA*$^{-}$ and *mlcE*$^{-}$ strains suggest that the lack of organization in the stress patterns of the *mhcA*$^{-}$ cells may result from the loss of MyoII's F-actin crosslinking function, and not due to an inability to generate shape-preserving forces which play a role during mitosis [122]. The importance of MyoII for the organization of the stresses is even more evident in a different view of

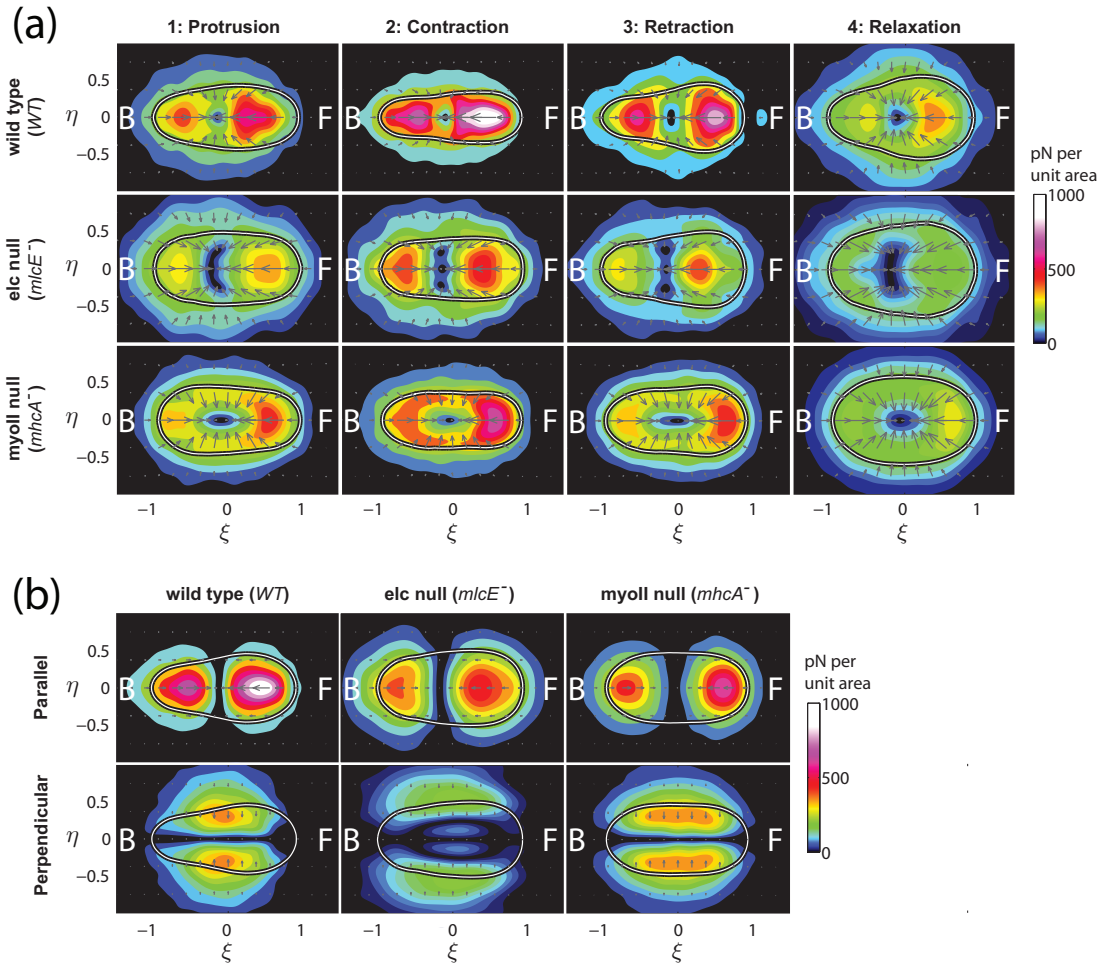

Figure 3.13: Spatiotemporal mapping of the traction stresses exerted by WT and MyoII mutant cells. (a) Phase-averaged traction stresses and cell shape corresponding to the four stereotypical stages defined in Fig. 3.10 for WT (first column, $N = 31$), $mlcE^{-}$ (second column, $N = 14$), and $mhcA^{-}$ (third column, $N = 27$) cells. The contour maps show the average traction stress field, measured in a reference frame rotated to coincide with the instantaneous principal axes of the cells and scaled with their half-length, $L(t)/2$. The colors indicate the magnitude of the stresses in pN per unit area and the arrows indicate their direction. The white contours show the average shape of the cells in this reference frame. The front "F" of the cell corresponds to $\xi > 0$ and the back "B" corresponds to $\xi < 0$. (b) Components of the traction stresses parallel and perpendicular to the major axis of the cell averaged over the entire motility cycle. An estimation of the average stresses in Pa (=pN/μm^2) (with a 10% error) can be obtained by dividing the values of traction stresses shown in this figure (in pN) by the squared average of $L(t)/2$ (in square micrometers). Average values for the length of each cell line during each phase of the motility cycle are given in Table 3.1.

the traction stress data presented in Fig. 3.13b. Here, the vectors of traction stress fields averaged over the entire cycle period are decomposed into their components parallel and

perpendicular to the main cell axis. This view emphasizes that in *WT* and *mlcE*$^{-}$ cells, the contribution of the parallel stress components to the total stress field is much higher than that of the perpendicular components. This is not true for *mhcA*$^{-}$ cells, in which the proportion of the perpendicular components is much larger, consistent with a key role of the MyoII F-actin-crosslinking function in regulating the spatial organization of the stress forces.

3.8.1 Selection of threshold for separating motility cycle into stages has negligible effect on phase-averaged traction maps

The algorithm applied to separate and sort the different stages of the motility cycle according to the temporal evolution of cell length, $L(t)$, applies a threshold on $L(t)$ as shown in Eq. 3.1, which depends on a threshold parameter, γ, that can vary between 0 and 0.5. Figs. 3.10, 3.13 and 3.15 were plotted using $\gamma = 0.2$. To check whether our results are independent of γ, we re-calculated Fig. 3.13 for values of the threshold parameter lower and higher than $\gamma = 0.2$. The resulting stress maps shown in Fig. 3.14 are highly similar to those in Fig. 3.13, confirming that our results are robust irrespective of the threshold.

3.9 The mechanical cycle of traction stresses and cell shapes remains similar but is slowed down when MyoII function is lost

We then applied the phase averaging method to examine the forces that cells exert during each stage of the motility cycle, enabling us to compare the mechanics of their locomotion. In Fig. 3.13a, each strain is represented by four distinct phase-averaged stress maps and cell shapes. Table 3.1 contains the measured average speed and duration corresponding to each phase and strain described in Fig. 3.13a. Remarkably, the *WT* and the two mutant strains that affect MyoII function move continuously during all phases with relatively small changes in speed, as shown in Fig. 3.10b and discussed above. In addition, the cells always contract. Comparison of the three strains shows that while the magnitudes of the traction forces in the cell-based reference system are different, the overall time evolutions of the stress patterns during the phases of the motility cycle are similar: they are minimal during the relaxation phase (minimal cell length), increase during protrusion, reach their maximum during contraction (maximal length), and decrease during retraction.

Table 3.1: Numeric values obtained from the statistical analysis of the motility cycle of *WT*, *mclE*$^-$, and *mhcA*$^-$ cell lines. The table lists the averages and standard deviations for each phase of the motility cycle as well as for the whole cycle. Values are given for cell length (L) , cell aspect ratio (AR), cell speed (V), translational component of area flux (AF_{trans}), component of area flux attributable to deformation (AF_{defor}), total duration of motility cycle (T) and duration of individual phases (T_1, T_2, T_3 and T_4), pole force (F_P), and strain energy (U_S). The number N of cells used for this statistical analysis: *WT* ($N = 31$), *mlcE*$^-$ ($N = 14$), and *mhcA*$^-$ ($N = 27$).

			L (µm)	AR	V (µm/min)	AF_{trans} (µm^2/s)	AF_{defor} (µm^2/s)	T (s)	F_P (pN)	U_S (pN µm)
WT	Whole Cycle	mean	21.85	2.53	12.71	1.27	0.01	94.10	345.8	54.86
		std	4.51	0.66	3.12	0.41	0.10	29.15	203.3	41.02
	Protrusion	mean	22.14	2.56	15.11	1.65	0.65	22.01	331.3	51.2
		std	4.57	0.60	4.00	0.54	0.50	11.52	213.4	38.0
	Contraction	mean	24.88	3.14	14.40	1.38	-0.03	23.19	414.5	69.2
		std	5.14	0.80	4.19	0.59	0.26	14.00	268.8	58.8
	Retraction	mean	22.10	2.55	11.47	1.02	-0.56	22.93	381.3	58.8
		std	4.52	0.70	3.12	0.40	0.42	10.84	264.5	53.7
	Relaxation	mean	19.13	2.02	10.97	1.05	0.04	29.96	292.6	46.9
		std	3.64	0.52	2.65	0.35	0.21	14.93	162.8	39.5
mlcE$^-$	Whole Cycle	mean	22.32	2.03	7.62	1.01	0.02	143.64	348.5	38.2
		std	3.31	0.29	2.30	0.36	0.09	36.22	132.9	19.1
	Protrusion	mean	22.34	2.02	8.55	1.14	0.41	32.80	344.3	38.5
		std	3.17	0.29	2.70	0.50	0.27	12.09	142.0	23.0
	Contraction	mean	24.76	2.39	8.50	1.13	-0.02	38.01	416.6	47.5
		std	2.98	0.35	2.58	0.40	0.18	7.75	162.1	25.9
	Retraction	mean	22.62	2.09	7.03	0.94	-0.31	39.30	363.1	40.4
		std	3.15	0.31	2.33	0.42	0.26	16.97	140.3	23.2
	Relaxation	mean	19.98	1.68	6.70	0.86	0.05	42.54	265.7	26.4
		std	3.55	0.29	2.23	0.39	0.11	18.76	119.2	14.4
mhcA$^-$	Whole Cycle	mean	19.98	2.08	5.64	0.58	0.00	190.81	284.6	48.8
		std	5.72	0.39	1.68	0.33	0.04	83.29	159.9	50.0
	Protrusion	mean	20.47	2.16	7.21	0.87	0.41	35.50	302.8	53.1
		std	5.78	0.44	2.08	0.40	0.25	19.27	205.4	61.1
	Contraction	mean	22.95	2.54	6.27	0.61	-0.03	41.22	364.4	64.5
		std	6.41	0.53	1.93	0.31	0.15	21.10	222.0	59.8
	Retraction	mean	20.24	2.13	4.90	0.40	-0.21	50.01	281.8	47.0
		std	5.41	0.38	1.62	0.34	0.24	28.14	174.8	51.6
	Relaxation	mean	17.57	1.72	5.20	0.56	-0.02	58.81	241.6	40.0
		std	5.11	0.32	1.65	0.41	0.12	30.83	141.3	48.3

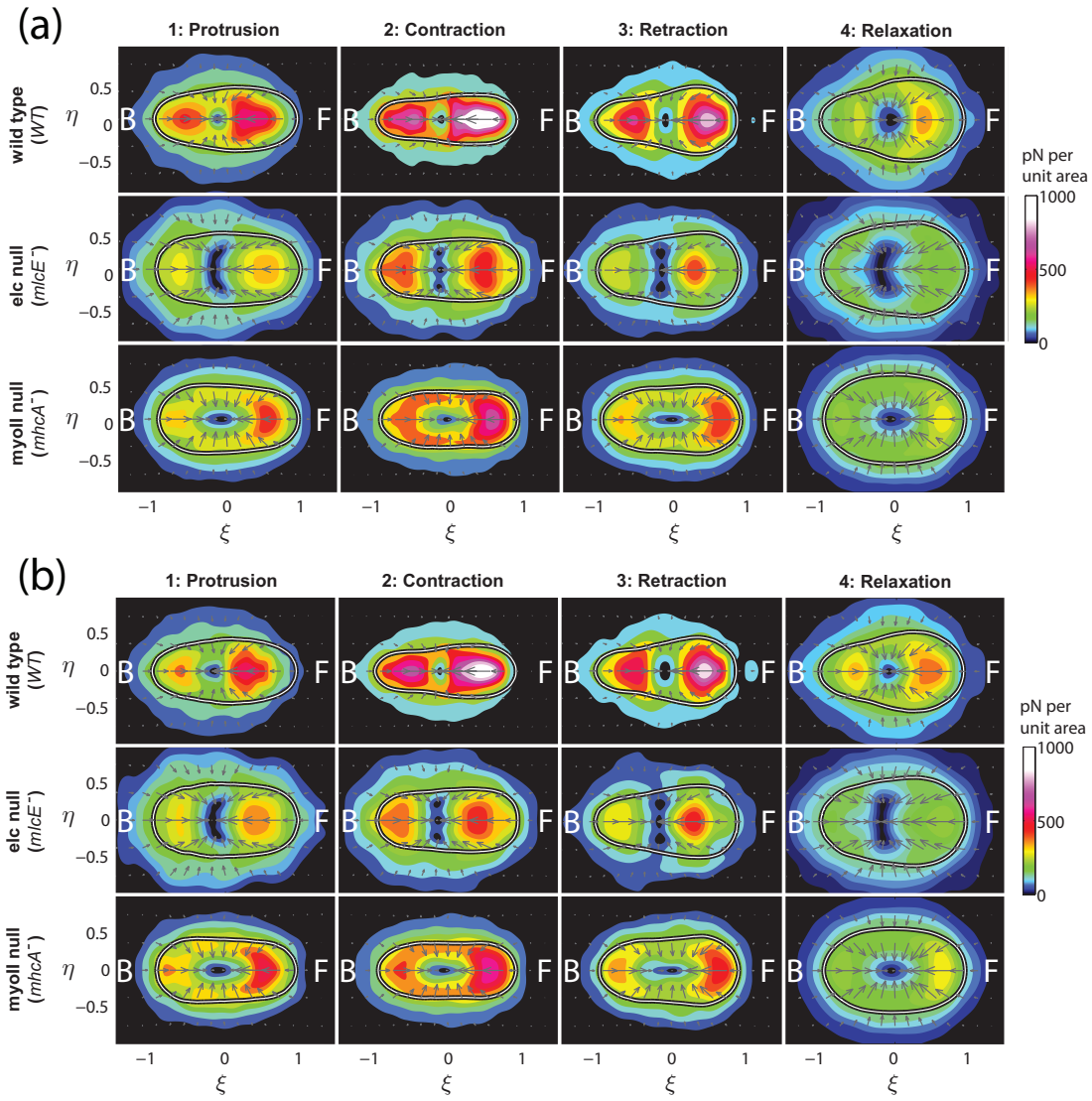

Figure 3.14: Spatiotemporal mapping of the traction stresses exerted by *WT* and MyoII mutant cells showing phase-averaged traction stresses and cell shape corresponding to the 4 stereotypical stages defined in Fig. 3.10. This figure is similar to Fig. 3.13a but in this case the stages have been separated using a value of the threshold $\gamma = 0.14$ (panel (a)) and $\gamma = 0.33$ (panel (b)) in Eq. 3.1, instead of the value $\gamma = 0.2$ used in Fig. 3.13a.

Theses observations support the hypothesis that *WT*, $mlcE^{-}$, and $mhcA^{-}$ cells move by implementing a similar motility cycle in which the cell length and the mechanical energy deposited by the cell on the substrate evolve similarly in time, which is consistent with the data presented in Figs. 3.9 and 3.10.

Despite these overall similarities, we observe differences between the three cell lines that can be correlated with the molecular properties of the MyoII complex. One of the

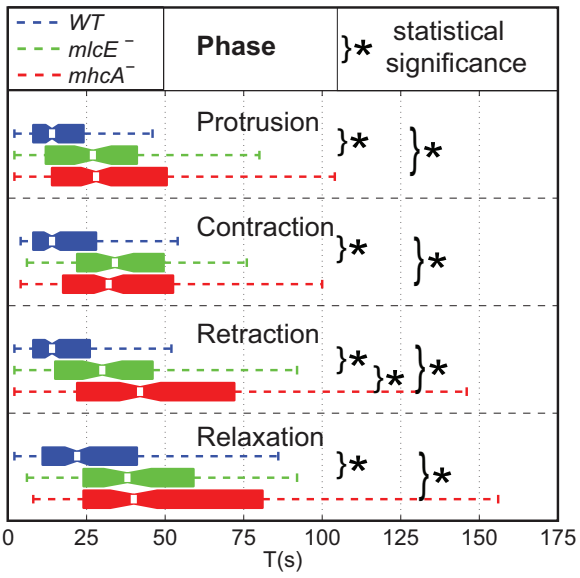

Figure 3.15: Box plot of the durations T_1, T_2, T_3, and T_4 of the stereotypical stages of the motility cycle defined in Fig. 3.10: 1) protrusion, 2) contraction, 3) retraction, and 4) relaxation.

most obvious differences between WT and MyoII mutant strains is the increased duration of all four phases T_1, T_2, T_3, and T_4 (Fig. 3.15). The durations of each of the four phases of WT cells are considerably shorter than those of $mhcA^-$ cells and are also far shorter than those of $mlcE^-$ cells for protrusion, contraction, and retraction and slightly shorter for the relaxation phase. This finding suggests that the contractile function of MyoII is important during all phases of motility and is an important factor in determining the overall speed.

We then examined the mechanical function of MyoII during each stage of the motility cycle in more detail by comparing the stress patterns and cell shapes. In WT cells, we observe that the region of concentrated stresses at the front is close to the centroid of the cell during protrusion, suggesting that the frontal part of the cell (the pseudopod) glides over the substrate (consistent with previous studies [15]). During contraction, this region of concentrated stresses seems to have moved closer to the front edge of the cell, suggesting the formation of new adhesion regions. Likewise, the region of concentrated stresses in the posterior part of the cell is located closer to the centroid of the cell during retraction, consistent with the back of the cell gliding forward. During protrusion, $mhcA^-$ cells produce comparatively low, spread-out traction stresses at their back, which indicates a dilated shape compared to WT and $mlcE^-$ cells. These differences could be due to an inability of $mhcA^-$ cells to compensate for the increase in cytoskeletal compression in response to

F-actin polymerization at the front through myosin contraction at the back of the cell. Instead, the bulge that appears at the back of $mhcA^-$ cells during this phase suggests that this compression is compensated for by an increase in membrane tension at the back. This implies that $mhcA^-$ cells are less effective in controlling the stability of protruding pseudopodia, which may explain the reduced frequency of pseudopod protrusion in $mhcA^-$ cells observed by Wessels et al. [111]. Consistent with these ideas, Fukui et al. [118] reported reduced stability of protruding pseudopodia in $mhcA^-$ cells subjected to centrifugal force. During retraction, the shape of WT and $mlcE^-$ cells becomes much wider at front than at the back due to the accumulation of mass coming from the retraction of the rear part of the cell. This shape is consistent with the cortical tension being lower at the front than at the back, probably due to MyoII contracting at the back and generating a pressure gradient. A similar, although less pronounced, frontal dilation is observed in $mlcE^-$ cells during retraction, suggesting that these cells can still partially control their cortical tension, presumably through the cross-linking action of MyoII. However, this mechanism seems to be less efficient in cells with reduced or modified MyoII-based motor function since this phase is prolonged in $mlcE^-$ mutants compared to WT cells (Fig. 3.15). Cells lacking MyoII cannot take advantage of either of these two mechanisms. They display a reduced dilatation of their front and their retraction is prolonged considerably. The relaxation time in $mlcE^-$ cells is longer than that in WT cells but shorter than that in $mhcA^-$ cells, indicating that both the contractile and the non-contractile activities of MyoII help to determine how fast a cell can finish retraction and protrude again to start the next motility cycle.

3.10 Our traction cytometry method is consistent with Newtonian mechanics

In our experiments, the cells are submerged in buffer and crawl on a substrate. At any time during migration, the product of cell mass and acceleration (inertia) must be equal to the difference between the forward traction force produced by the cell and the viscous drag exerted by the surrounding fluid. The drag is estimated using Stokes law, $D = S\,\mu\,V\,/d$, where μ is the viscosity of water, d the gap between the cell and the substrate, and S the area of the horizontal projection of the cell. Assuming a typical value for the gap given by [123], $d \approx 100$ nm, the estimated value $S \approx 100$ µm^2, and the average velocity measured in our experiments, we estimate that $D \approx 0.1$ pN. From our shape and velocity measurements, we estimate that the inertia is at least 3 orders of magnitude lower than D. Therefore, the

Table 3.2: The magnitude of net traction is negligible. The left column contains the net forces measured in pN ($|\mathbf{F}_{net}|$, see Eqs. 2.13 and3.9). The right column contains the ratio between the net forces and the average magnitude of the forces exerted by the cell at different locations, $|\mathbf{F}_{net}/F_R|$ (for a mathematical definition of F_R, see Eq. 3.10). Histograms of the instantaneous values of the magnitudes represented in this table are shown in Fig. 3.16.

		$\lvert\mathbf{F}_{net}\rvert$ (pN)	$\lvert\mathbf{F}_{net}/F_R\rvert$(%)
WT	mean	7.70	1.62
	std	4.51	1.19
$mlcE^-$	mean	11.29	2.03
	std	7.48	0.93
$mhcA^-$	mean	10.39	1.85
	std	9.36	1.14

cells in our experiments must exert a non-zero but very small net force on the substrate while moving. Previous methods developed by others were designed to yield a zero net traction forces regardless of the actual measurements [28, 33]. These methods are based on the Boussinesq solution of the elastostatic equation, which assumes an infinitely thick gel. Our method takes the finite thickness of the substrate into account, which enables the determination of these non-zero net traction forces. The net force exerted by a cell on an elastic substrate of Young modulus E, Poisson ratio σ and thickness h is

$$\mathbf{F}_{net} = \int\int [\tau_{xz}(x,y), \tau_{yz}(x,y)]\, dx\, dy = \frac{E}{2(1+\sigma)h} \int\int \mathbf{u}(x,y)\, dx\, dy, \tag{3.9}$$

where $\mathbf{u}(x,y)$ is the horizontal vector deformation field measured at the surface of the substrate and $\boldsymbol{\tau}(x,y) = [\tau_{xz}(x,y), \tau_{yz}(x,y)]$ are the stress (force/area) exerted by the cell on the substrate. Fig. 3.16 shows histograms of the net traction force's magnitude measured for all cells studied, as well histograms of the ratio between the net traction force and the average magnitude of the force exerted by the cell at each location, which was defined as

$$F_R = \int\int \sqrt{\tau_{xz}^2(x,y) + \tau_{yz}^2(x,y)}\, dx\, dy. \tag{3.10}$$

Table 3.2 shows the average and standard deviation of $|\mathbf{F}_{net}|$ and $|\mathbf{F}_{net}/F_R|$ for the three cell lines used in this study. The results indicate that the measured net forces are approximately 10 pN, which is rather small if one considers that a single myosin II head can generate a force stroke of about 5 pN (Finer et al., 1994). Fig. 3.16 and Table 3.2 also show that the measured net forces are between 50 and 100 times smaller than the average magnitude of

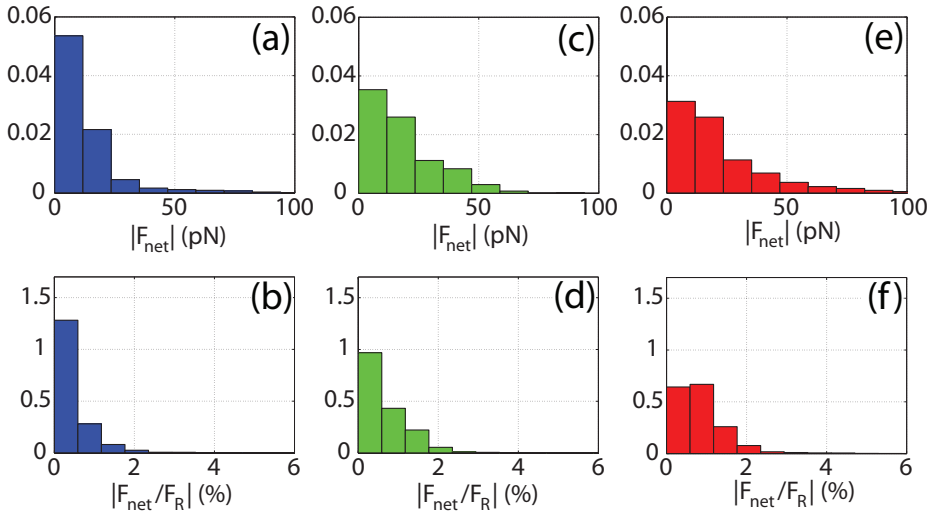

Figure 3.16: Histograms of the net forces measured for all cells studied. Panels (a), (c) and (e) show histograms of the magnitude of the net forces measured in pN ($|\mathbf{F}_{net}|$, see Eq. 3.9). Panels (b), (d) and (f) show histograms of ratio between the magnitude of the net forces and the average magnitude of the forces exerted by the cell at different locations, $|\mathbf{F}_{net}/F_R|$ (for a mathematical definition of F_R, see Eq. 3.10). Panels (a) and (b) correspond to *WT* cells. Panels (c) and (d) correspond to $mlcE^{-}$ cells. Panels (e) and (f) correspond to $mhcA^{-}$ cells. The averages and standard deviations corresponding to each of the histograms of this figure are shown in Table 3.2.

the contractile forces exerted by the cell, which is within the error of our measurements. The discrepancy between the measured net forces and our theoretical estimations of 0.1 pN may either be due to the simplified assumptions used for the estimation of the drag or be due to experimental noise. In summary, the net traction forces we measure and our estimates are consistent with Newtons second law of mechanics.

3.11 Some traction forces are expected to fall outside the average cell shape contour in our phase averages

Fig. 3.13 shows non-zero average traction forces outside of the average cell contours. A priori, this result may appear counter-intuitive because the cell can only apply traction forces inside its two-dimensional outline at each instant of time. However, as discussed in the Materials and Methods, when one plots the averaged distribution of traction forces superposed on the averaged cell contour the variability in cell shape leads to nonzero average forces outside of the average cell contour. This effect is illustrated in Fig. 3.19a, which shows the average force map obtained from the three snapshots shown in Fig. 3.17. This figure

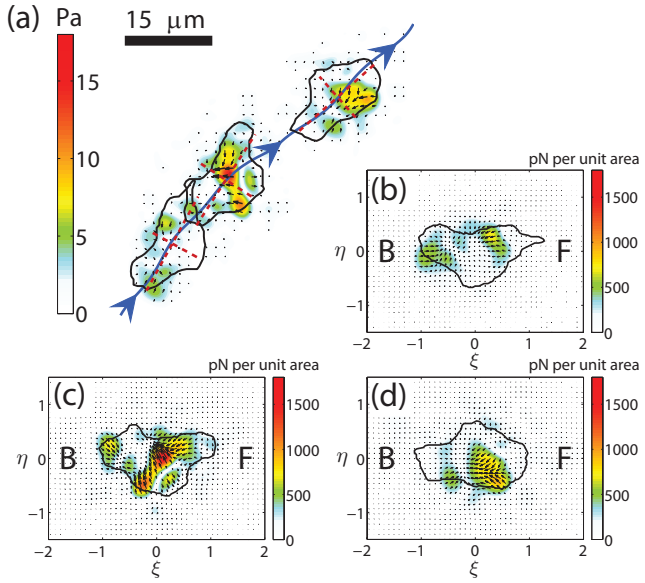

Figure 3.17: Steps taken in the calculation of the average distribution of traction forces. (a) Snapshots (three) of the trajectory of a *WT* cell in the laboratory reference frame. The black contours are the measured cell outlines. The color shades and arrows indicate the magnitude and direction of the traction stresses exerted by the cell on the substrate. The dashed red lines represent the major and minor axes of the 2D projection of the cell (outline of the cell). The blue line represents the trajectory of the centroid of the cell. (b-d) Same three snapshots aligned and scaled into cell-based coordinates (Eq. 3.3). The cells have been aligned so that their major axes always coincide with the horizontal axis, and their dimensions scaled with the length of the each cell. The dashed black line in these panels represents the average contour of *WT* cells. The labels "F" and "B" indicate respectively the front and back of the cell.

shows that the solid black lines, which represent the instantaneous cell contours, extend beyond the dashed blue contour that represents the average cell contour at some locations. This explains why we should not expect the average traction stresses to be constrained to the inside of the average cell contour.

In contrast to the methods of others [28, 33], our method does not constrain the stresses to the cell outline and a small proportion of the stresses we calculate for individual cells are localized outside their contour. We therefore want to show that even we when eliminate this small contribution, the statistical variability of cell shape alone leads to non-zero traction stresses outside of the average cell contour. For that purpose, we re-calculated the average traction stress map of Fig. 3.17 using the constrained Fourier transform traction cytometry method proposed by Butler et al. [33]. This method iteratively solves the elastostatic equation for the substrate and corrects the measured deformations to yield zero

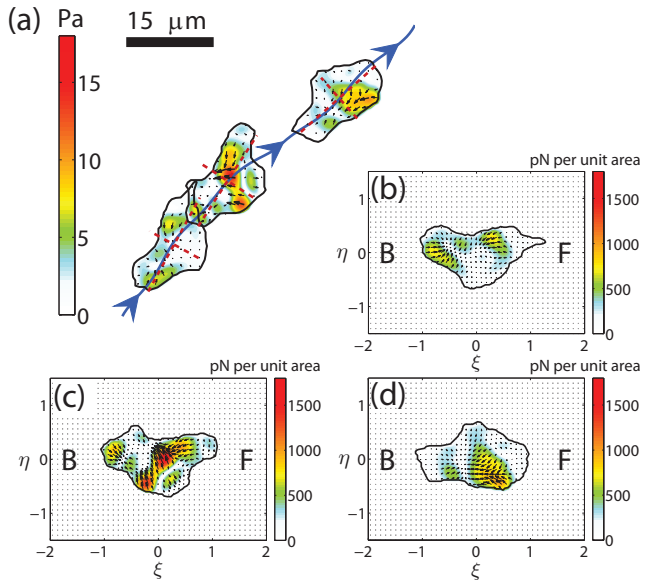

Figure 3.18: Same as Fig. 3.17 when the traction forces are calculated using the constrained iterative method proposed by Butler et al. [33], which imposes the forces to be zero outside of the instantaneous cell outline.

traction stresses outside of the cell upon convergence. Figs. 3.18 and 3.19b are obtained with the constrained method and are equivalent to Figs. 3.17 and 3.19a. By the design of the constrained method, the obtained stresses are generally inconsistent with the experimentally measured deformation field [28], and are known to be sensitive to small errors in the identification of the cell contour [124]. Additionally, methods that constrain the forces outside the cell to zero, can lead to artificially elevated stresses near the cell periphery. Despite these caveats, the stress fields shown in these plots are qualitatively similar. As expected, in the three snapshots of Fig. 3.18 the traction stresses are zero outside of the instantaneous cell contour. However, the averaged traction stress map of these three cells in Fig. 3.19b shows non-zero stresses in some locations outside of the average cell contour because there is a non-zero proportion of the cell outlines outside the average contour generating these stresses.

3.12 Discussion

There have been several attempts to model the underlying physical processes in cell motility by using continuum mechanics approaches [116, 125, 126]. However, quantitative measurements of the cellular traction forces are still challenging because of the necessary

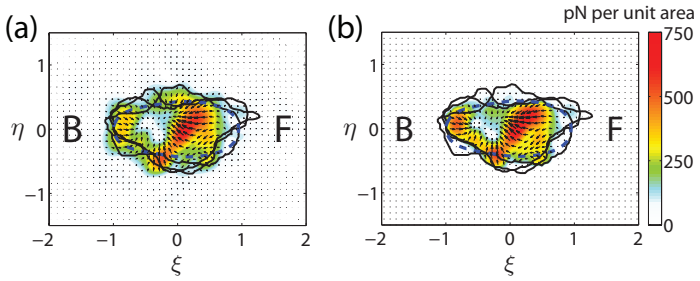

Figure 3.19: Average map of traction force resulting from: (a) the three snapshots shown in Fig. 3.17, (b) the three snapshots shown in Fig. 3.18 (calculated using the constrained iterative method proposed by Butler et al. [33], which imposes the forces to be zero outside of the instantaneous cell outline). The solid black lines are the instantaneous cell contours coming from the three snapshots and the dashed blue contour is the average cell contour for *WT* cells. The labels "F" and "B" indicate respectively the front and back of the cell. Note that, in both panels (a) and (b), because the instantaneous cell contours may exceed the average cell contour at some locations, the average traction stresses are not necessarily zero outside of the average cell contour.

temporal and spatial resolutions. These requirements become especially demanding in the case of *Dictyostelium* cells because of their relatively small size and high migration speeds. Therefore, only a few studies to quantify the dynamics of the migration of these cells have been performed to date [79, 80, 127]. In this dissertation, we have measured the evolution of the forces and strain energies produced by *Dictyostelium* cells with high temporal and spatial resolution (Figs. 3.3 and 3.4). This approach has enabled us to record the quasi-periodic oscillations of these variables and validate the generally accepted cycle of pseudopod protrusion, adhesion, contraction, and retraction of the back [1]. Our traction cytometry method has allowed us to compute the traction field when the net force exerted by the cell is not zero (see Eqs. 2.13 and 3.9). In our experiments, the contractile forces produced by *Dictyostelium* cells were found to be much higher than the viscous drag force they need to overcome to move. Because the cell inertia is negligible, these forces always show a converging pattern and largely cancel each other out at any given time, so that the resultant net thrust force is too small to be measured reliably with our method. There are, however, other conditions in which this net force could be much higher, and the calculation of the net thrust force could greatly benefit from our improved method, i.e., cells under external flow shear [128, 129] or under centrifugal forces [118].

We have expanded previous descriptions of the amoeboid motility cycle [1] and have elucidated the functions that MyoII plays in controlling the spatial distribution of traction forces that regulate this process. We have used a new phase-averaging statistical

method to analyze the measurement of the temporal evolution of the traction forces and cell shapes changes during chemotaxis that does not depend on the subjective identification of representative cells. Our statistical analysis provides a quantitative representation of the motility cycle of the average cell with detailed spatial and temporal information and provides statistically significant evidence for the existence of a coherent motility cycle, as was proposed previously based on microscopic observations [37, 78, 130]. Our analysis of the area fluxes of the plane view of the cells undergoing chemotaxis clearly shows that the overall cell movement is the result of a combination of a continuous translocation with a superimposed periodic cycle of front protrusion and rear retraction. These results provide clear evidence against an alternative possibility in which cells move continuously, undergoing random changes in cell shape, traction stresses, and length.

We show that when amoeboid cells undergo chemotaxis on elastic substrates, the largest fraction of the variations in the strain energy transmitted to the substrate are "periodic" and coordinated with the changes in cell length, rather than the superposition of chaotic "random" changes. Owing to the periodic nature of this process, we have been able to implement a novel statistical methodology that dissects the motility cycle into four "canonical" stages and to compute average maps of traction forces for each stage of the cycle. This phase-average analysis has allowed us to quantify the main differences in the cell shape changes and generation of traction forces among *WT*, $mlcE^{-}$, and $mhcA^{-}$ strains. These maps provide new insights into how MyoII crosslinking and contractility functions contribute to the generation of the traction forces that cells exerts on the substratum as they move. We show that *WT* cells and cells with altered MyoII function exhibit important and significant differences, providing insight into the complex roles MyoII plays in regulating these forces. We note that there are specific differences between *WT* and $mlcE^{-}$ cells. In vitro, MyoII lacking the essential light chain, while retaining ATPase activity, lacks motor activity, although it still binds and cross-links F-actin (for discussion, see Chen et al. [67], Xu et al. [121]). However, the behavior of this myosin has not been fully characterized, particularly the force-velocity relationship and how this myosin behaves in response to mechanical stress. For example, the MyoII complex lacking the essential light chains may behave similar to $\text{MyoII}^{\text{S456L}}$ in that it is able to undergo translocation under conditions when mechanical stress is applied [131]. The differences between the strains can at least partially be explained by a possible altered responsiveness of the MyoII motor activity or reduced motor activity in $mlcE^{-}$ cell, while retaining the ability to cross-link F-actin or, in $mhcA^{-}$ cells, the absence of MyoII function [111]. Comparison of phase-averaged con-

tours of *WT* or *mlcE*$^{-}$ cells to those of *mhcA*$^{-}$ cells show that *mhcA*$^{-}$ cells are overall of more rounded shape at all stages of the motility cycle. More importantly, we show that *mhcA*$^{-}$ cells are still able to contract continuously, but unlike the other cell types, *mhcA*$^{-}$ cells do not mainly contract by exerting opposing pole forces front to back, but rather they contract all around the cell periphery. This difference in the stress distribution reveals an important role of MyoII for cytoskeletal integrity through its F-actin cross-linking function. In addition to the loss of myosin motor activity, which impairs rear retraction, this reduced organization of the stress forces may contribute to the observed increase in the periods of the motility cycle of *mhcA*$^{-}$ cells. Additional evidence for the role of MyoII in cytoskeletal integrity becomes apparent in the protrusion phase in which, in *mhcA*$^{-}$ cells, the back is wider than the front, suggesting that the cytoskeletal integrity at the back of the cell may be insufficient to balance the backward, forces produced by actin polymerization during protrusion [45–47]. A reduced ability to compensate for these forces also may be connected with the reduced frequency of pseudopod protrusion in *mhcA*$^{-}$ cells, which has been reported previously [46, 111, 118]. Our detailed analysis of the temporal and spatial distribution of stress forces also suggests that both MyoII actin cross-linking and contractility functions play an important role in increasing the level of intracellular tension at the back of the cell to promote retraction.

It should be noted that MyoII may determine the stresses transmitted to the substrate not only by setting the level of cytoskeletal tension through its cross-linking and contraction functions but also by modulating the number and area of the cell substrate adhesions. Therefore, a more detailed dissection of the mechanical function of MyoII would require measuring jointly the cell traction forces and substrate attachment regions. Nevertheless, our pole force measurements (Table 3.1), which represent the integrated effect of the stresses in the front and back of the cell [35], provide a quantification of the overall level of cytoskeletal contraction in the cell independent of the number and area of the adhesions. These pole force measurements show no significant differences between *WT* and *mlcE*$^{-}$ cells but are 27% lower in *mhcA*$^{-}$ cells, consistent with prior observations that the cortical resistance to compression is reduced by 32% in *mhcA*$^{-}$ cells [132], and supporting an important role of MyoII for cytoskeletal integrity through its F-actin cross-linking function. In contrast, these data indicate that roughly 70% of the magnitude of cellular stresses comes from molecules other than MyoII. For example, we know that other actin cross-linking proteins, including α-actinin, cortexillin, and gelation factor (ABP120), make a significant contribution to maintaining cytoskeletal integrity and cortical stiffness [133–

135]. It is therefore reasonable to assume that in $mhcA^-$ cells, where our measurements show that contractile forces are more uniformly distributed throughout the cortex, some of these cross-linkers are relocalized and possibly partially compensate for the lack of MyoII crosslinking function.

We gained further insight into the conserved motility cycle by decomposing our measurements of the movement of *Dictyostelium* cells into two distinct kinematical components: an inchworm-like motility component consisting only of protrusion and retraction and a shape-preserving component consisting only of continuous translocation. These events are not necessarily driven by different biochemical processes but are characterized by a different level of spatial and temporal coherence. We argue that the shape-preserving component is the result of continuous contributions from events occurring at a length scale much shorter than the cell length and at a time scale much shorter than the measured period of the motility cycle (T), possibly at the level of a single protein or molecular complex. Our MyoII mutant data suggest a direct involvement of continuous actomyosin contraction in this component and therefore indicate that MyoII makes an important contribution to cell speed during all phases of motility. Such a contribution may be related to its previously described role in frontal blebbing, which is sometimes observed in highly motile *Dictyostelium* cells [117, 119] and other cell types [136, 137]. Interestingly, both the total migration speed and its inchworm-like and shapepreserving components are inversely proportional to the period of T. This dependence on the period of the cycle for the shape-preserving portion is unexpected and strongly suggests the existence of a coupling mechanism. The "inchworm" component presumably modulates the overall shape of the cell as well as other cellular properties like the global level of stress that drives the continuous, shape-preserving translocation of the cell. Recently, two components have also been found to play a role in leukocyte motility, but, rather than contributing to motility simultaneously, they have been described as a switch from deformation to gliding when MyoII activity is suppressed, or when substrate adhesiveness is increased [138]. Further work is needed to understand the exact relationship between our results and this observation, but the two findings suggest the existence of evolutionarily conserved mechanical aspects of amoeboid motility.

Our phase-averaged maps also shed light on the mechanical process of motility and reflect on the role of MyoII in this process. Our traction cytometry measurements reveal that cells migrating under conditions of normal adhesiveness generate opposing traction "pole forces" much greater than those required to overcome the external resistance of the environment [35]. Basic mechanical principles suggest that the speed of amoeboid cells is

limited by the amount of propulsive power that they are able to generate through their traction forces. The average propulsive power generated per motility cycle can be represented as $P = F\,v \sim F\lambda/T$, where F is the characteristic traction force, λ is the distance traveled per cycle, and T is the characteristic period or duration of the cycle. Two extreme regimes of motion can arise when the propulsive power is limited either by the strength of the forces that the cells can produce to overcome the resistance of their environment (strength limited motility) or by the pace at which they can repeat their motility cycle (pace limited motility). Strength limited motility is realized experimentally in highly adhesive substrates, in restrictive environments such as multicellular aggregates or under an agar overlay, or when cells are moving against an external force generated by a micropipette. Previous studies have established the importance of MyoII for cell motility under these conditions [75, 111–113, 122, 135, 139]. Our study provides an analysis of the role of MyoII in motility under nonrestrictive conditions and helps define specific roles for MyoII functions in controlling traction forces and cell motility.

Because the net traction forces required to drive the motion of the cell were measured to be much smaller than the forces that the cell applies locally to the substrate in all of cases that we studied (Table 3.2 and Fig. 3.16), we suggest that the motility of *WT* and mutant cells on flat surfaces is not strength limited, in contrast to the case of cells moving in highly adhesive substrates, in restrictive environments, or against external forces. Instead, we propose that amoeboid motility on flat surfaces is pace limited. Consistent with this regime, we measure that a cell mean velocity of migration V and the period T of its motility cycle are related by a rather simple proportionality as $V = \lambda/T$, where $\lambda \approx 18$ µm is a "stride" length. Furthermore, we find that the stride length is conserved between *WT* cells and strains with modified MyoII contractility or even in cells with reduced adhesion. The finding that, for *WT* cells and these specific mutants, regardless of the speed of migration, a cell on the average advances a fixed length per cycle, suggests that the mechanochemical processes that define λ are conserved in all of these strains. Consistent with the above findings, we propose that the stride length may be controlled by the regulation of F-actin polymerization either via intrinsic properties of F-actin polymerization, such as an average duration controlled by biochemical feedback loops, or via adaptable sensors of physical parameters. We further postulate that such a control mechanism is more likely than the determination of a set stride length by direct physical constraints such as membrane stiffness, because *WT* and MyoII mutant strains differ greatly in their cytoskeletal properties [140–142], yet vary little in their characteristic step length. Moreover, in agreement with previous reports [34, 35, 79, 111], we

find that the period T of the motility cycle is partially determined by altered properties of actomyosin contractility (lacking in $mlcE^{-}$ and $mhcA^{-}$ cells) and by the actin crosslinking function of MyoII (lacking in $mhcA^{-}$ cells). In particular, we show quantitatively that the actomyosin contractility is important for efficient progress through all of the phases of the motility cycle. We find that the F-actin crosslinking by MyoII is as important for the initiation of the protrusion of the front as for the retraction of the rear, possibly by indirectly stabilizing the cytoskeletal organization along the lateral sides and posterior of the cell where cortical MyoII is distributed along an anterior-posterior gradient [40].

Chapter 3, in part, have been published in the *Proceedings of the National Academy of Sciences of the United States of America*, "Spatio-temporal analysis of eukaryotic cell motility by improved force cytometry," by J. C. del Álamo, R. Meili, B. Alonso-Latorre, J. Rodriguez-Rodriguez, A. Aliseda, R. A. Firtel, and J. C. Lasheras (2007) 104:13343-13348, in the *Conference Proceedings of the IEEE Engineering in Medicine and Biology Society*, "Distribution of traction forces associated with shape changes during amoeboid cell migration," by B. Alonso-Latorre, R. Meili, E. Bastounis, J. C. del Álamo, R. A. Firtel, and J. C. Lasheras (2009) 2009:3346-3349, in *Molecular Biology of the Cell*, "Myosin II is essential for the spatiotemporal organization of traction forces during cell motility," by R. Meili R., B. Alonso-Latorre B., J. C. del Álamo, R. A. Firtel, J. C. and Lasheras (2010) 21:405-417, and has been accepted for publication in the *International Journal of Transport Phenomena*, "Distribution of traction forces and intracellular markers associated with shape changes during amoeboid cell migration," by J. C. Lasheras, B. Alonso-Latorre, R. Meili, E. Bastounis, J. C. del Álamo, and R. A. Firtel (2010). The thesis author is a co-author in the first publication and the primary investigator in the last three publications.

Experiments were performed by Dr. R. Meili in the Section of Cell and Developmental Biology, University of California, San Diego. This investigation was partially funded by the U.S. National Institutes of Health.

Chapter 4

An Oscillatory Contractile Pole-Force Mode Dominates the Traction Forces Exerted by Migrating Amoeboid Cells

Amoeboid cell migration requires the coordinated regulation of many molecules, but occurs through a small repertoire of shape changes consisting mainly of anterior protrusions and posterior retractions [6]. There is ample evidence indicating that these morphological changes are mechanically coupled to the biochemical modulation of the adhesions via the traction stresses exerted by the cell on the extracellular matrix (ECM) [36, 143–146]. However, there is a need to better understand the coupling of the global cell shape changes, the distribution of traction stresses and the associated biochemical processes.

The objective in this chapter is to refine the spatiotemporal description of motility by obtaining a statistically significant characterization of the relationship between traction forces and cell shape in migrating amoeboid cells, using PCA as primary tool. For this purpose, we carried out simultaneous measurements of the time evolution of cell shape and traction forces exerted by *Dictyostelium* cells migrating individually over a flat substrate. We then applied a modified version of PCA to the measurements of the traction forces which maximized the strain energy accounted by each component. This analysis provided the principal traction force patterns and shape changes implemented by migrating cells in terms of strain energy production. These patterns have a clear physical interpretation

because the strain energy represents the amount of mechanical work performed by the cell against its surroundings while it is moving.

PCA effectively "compressed" the mechanics of locomoting *Dictyostelium* cells by finding a minimal set of degrees of freedom that accounted the work performed by the cells. We found that a set of five canonical principal components, exhibiting a high degree of repeatability from cell to cell, accounted for most of the traction work exerted by WT cells. The most important of these components accounted for $\approx 40\%$ of the traction work, and contracted the substrate from front and back towards the center of the cell. Its temporal evolution was oscillatory and correlated well with that of the strain energy and the cell length. We also identified the most relevant principal components in two mutant strains with contractility defects: MyoII Essential Light Chain Null ($mlcE^{-}$) and MyoII Heavy Chain Null ($mhcA^{-}$) cells.

The identification of the most relevant strain energy components could aid to semiempirical modeling approaches [147–150] by providing a reduced set of parameters that describe the motion of the cell. This framework can be readily applied to other problems such as cell migration inside 3D matrices [151–154], or to the study of the spatio-temporal distribution of relevant cytoskeletal proteins [155–158].

4.1 Analytical methodology

Experiments using the methodology described in Chapter 2 were carried out for WT, $mlcE^{-}$, and $mhcA^{-}$ cells, tracking at each instant of time both cell shape (see Section 2.1.2) and cell traction stresses exerted on the substrate free surface, $\boldsymbol{\tau} = (\tau_{zx}, \tau_{zy})$, calculated from measurements of the horizontal displacements at the substrate free surface, $\mathbf{u} = (u, v)$, and assuming negligible vertical tensile stresses at the substrate free surface ($\tau_{zz}(z = h) \sim 0$) (see Sections 2.1.7 and 2.2.1).

This section describes the analytical tools, applied to the recordings of cell shape and cell traction stresses, which have led to the dissection of the different components through which migrating *Dictyostelium* cells exert mechanical work.

4.1.1 Cholesky decomposition of the strain energy U_S exerted on a flat substrate

The strain energy exerted by the cell on the surface of the substrate at a given instant of time was [33]

$$U_S(t) = \frac{1}{2}\int_A \boldsymbol{\tau}(\mathbf{x},t)\cdot\mathbf{u}(\mathbf{x},t)\,d\mathbf{x} = \{\boldsymbol{\tau},\mathbf{u}\}\,, \tag{4.1}$$

where $(\cdot)$ represents scalar product, $\int_A d\mathbf{x}$ represents a surface integral in a box enclosing the cell, and $\{\,\}$ represents an inner product. Note that U_S is equivalent to the mechanical work the cell is exerts on the substrate.

We applied PCA to obtain a reduced set of traction force patterns which the cell used to exert mechanical work on the substrate. PCA works by optimizing the modal decomposition of a set of observations according to the norm associated to a predefined inner product. We then rewrote the strain energy as the norm $U_S = \{\boldsymbol{\theta},\boldsymbol{\theta}\}$, where $\boldsymbol{\theta}(\mathbf{x})$ is the *strain energy square root* or *U_S-square root*. This decomposition is called the Cholesky decomposition and is easier to perform in the Fourier domain,

$$U_S = \frac{L_B^2}{2}\sum_{\alpha=-\infty}^{\infty}\sum_{\beta=-\infty}^{\infty}\widehat{\mathbf{u}}^*_{\alpha\beta}\,A_{\alpha\beta}\,\widehat{\mathbf{u}}_{\alpha\beta}, \tag{4.2}$$

where $\widehat{\mathbf{u}}_{\alpha\beta}$ are the Fourier coefficients of the lateral displacement vector, $A_{\alpha,\beta}$ is the Fourier norm matrix and $()^*$ denotes Hermitian transposition. In Fourier space, the problem of finding the functional Cholesky decomposition of the norm operator is reduced to finding the algebraic Cholesky decomposition of the norm matrix, $A_{\alpha\beta} = Q^*_{\alpha\beta}\,Q_{\alpha\beta}$, where $Q_{\alpha\beta}$ is a lower-triangular matrix. Introducing this decomposition in Eq. 4.2, one obtains that $\widehat{\boldsymbol{\theta}}_{\alpha\beta} = Q^*_{\alpha\beta}\,\widehat{\mathbf{u}}_{\alpha\beta}$, and inversion of the Fourier transform yields

$$\boldsymbol{\theta}(\mathbf{x}) = \mathcal{F}^{-1}\left(\widehat{\boldsymbol{\theta}}_{\alpha\beta}\right) = \mathcal{F}^{-1}\left(Q^*_{\alpha\beta}\,\widehat{\mathbf{u}}_{\alpha\beta}\right). \tag{4.3}$$

Prior to applying PCA, we mapped the *U_S-square root* $\boldsymbol{\theta}(\mathbf{x})$ in the dimensionless cell-based coordinate system (ξ,η) defined in Section 3.1 (see Eq. 3.3), which takes into account the changes in cell shape and orientation (see Fig. 3.1). In order to ensure that the magnitude of both the traction forces and the strain energy were conserved upon transformation of reference frame, the traction stresses and the *U_S-square root* were redefined respectively as $\boldsymbol{\tau}^\star(\boldsymbol{\xi}) = L^2\,\boldsymbol{\tau}(\boldsymbol{\xi})/4$ and $\boldsymbol{\theta}^\star(\boldsymbol{\xi}) = L\,\boldsymbol{\theta}(\boldsymbol{\xi})/2$. The size of the computational box where traction forces were calculated was 6 dimensionless units, and was discretized using 129×129 nodes.

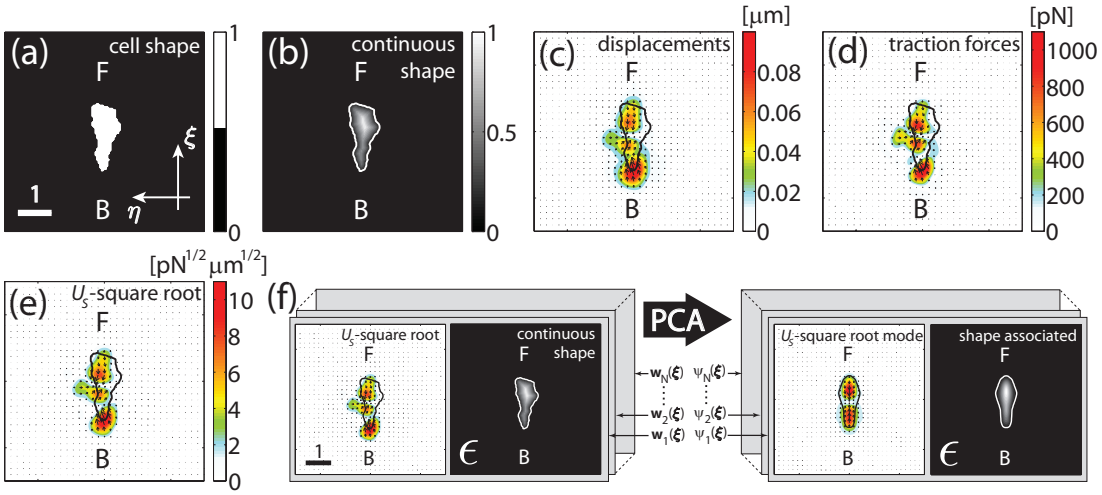

Figure 4.1: morphology in the context of the PCA methodology applied. Functions used to study the dynamics of traction stresses and cellular shape. For a *WT* cell at a certain instant of time: (A) 2D function of the cell shape ($p(\boldsymbol{\xi})$). (B) 2D continuous function of the cell shape ($s(\boldsymbol{\xi})$). The white line is the contour of the cell. At the free surface of the substrate: (C) Horizontal displacement field exerted by the cell ($\mathbf{u}(\boldsymbol{\xi})$), (D) Traction force field associated ($\boldsymbol{\tau}(\boldsymbol{\xi})$), (E) Associated field of the function *strain energy square root* ($\boldsymbol{\theta}(\boldsymbol{\xi})$). In panels (C-E): the colormap and arrows indicate respectively the magnitude and direction of the variable represented, and the black contour the contour of the cell. (F) We applied PCA over a set of observations combining $\boldsymbol{\theta}(\boldsymbol{\xi})$ and $\mathbf{s}(\boldsymbol{\xi})$ ($\mathbf{s}(\boldsymbol{\xi})$ multiplied by a very small factor ϵ, so that its weight in the optimization process is negligible), and as a result we obtained a set of strain energy components ($\boldsymbol{\varphi}(\boldsymbol{\xi})$) and the cell shape associated to each component ($\boldsymbol{\chi}(\boldsymbol{\xi})$). Scale bars in panels (A) and (F): 1 dimensionless unit of length (=half-length of the cell).

4.1.2 Scalar field mapping of the shape of the cell allows relating shape to traction forces

The instantaneous cell shape is mapped using the dimensionless cell-based coordinate system defined in Eq. 3.3 as a 2D function $p(\boldsymbol{\xi})$ such that $p(\boldsymbol{\xi}) = 1$ if $\boldsymbol{\xi}$ laid within the contour of the cell, and $p(\boldsymbol{\xi}) = 0$ otherwise (Fig. 4.1a). This function was discontinuous at the contour of the cell, which could lead to undesired spurious oscillations in its modal decomposition (the Gibbs phenomenom, see [89]), and deteriorates the convergence of PCA. This was avoided by using a continuous scalar field $s(\boldsymbol{\xi})$ to represent cell shape

$$s(\boldsymbol{\xi}) = p(\boldsymbol{\xi})\, c(\boldsymbol{\xi}) / \max_{\boldsymbol{\xi}}[c(\boldsymbol{\xi})], \tag{4.4}$$

where $c(\boldsymbol{\xi})$ was the distance from each point inside the cell $\boldsymbol{\xi}$ to the cell contour (see Fig. 4.1b).

Because our aim was to determine how the cell shape associates with strain energy and traction forces at each instant of time, we applied PCA on the composite three dimensional function

$$\mathbf{w}(\boldsymbol{\xi},t) = (\boldsymbol{\theta}\,, \epsilon s)\,(\boldsymbol{\xi},t), \tag{4.5}$$

which grouped both the U_S square root and the shape of the cell. The value of parameter ϵ was set very low ($\epsilon = 10^{-9} - 10^{-12}$) to ensure that the results from PCA only depended on the strain energy and were independent on shape variance. We verified that the use of the small parameter ϵ, as well as its selected magnitude, did not affect the calculation of the components of $\boldsymbol{\theta}(\boldsymbol{\xi})$.

4.1.3 Principal component analysis (PCA) on the *strain energy square root* and asssociated cell shape

Given a set of N experimental recordings of cell shape and traction forces (i.e. at times $t = t_k$ for $k = 1...N$), we applied PCA [159, 160] to the composite function $\mathbf{w}(\boldsymbol{\xi},t)$ (Eq. 4.5), which allowed us to express it as the weighted sum of principal components

$$\mathbf{w}(\boldsymbol{\xi},t) = \sum_{k=1}^{N} a_k(t)\,\boldsymbol{\psi}_k(\boldsymbol{\xi}), \tag{4.6}$$

where the basis functions $\boldsymbol{\psi}_k(\boldsymbol{\xi}) = (\boldsymbol{\varphi}(\boldsymbol{\xi})\,, \epsilon\,\chi(\boldsymbol{\xi}))_k$, contain the spatial structure of cell shape and traction forces of each principal component and are denoted *principal functions*, and a_k is the weight coefficient for each component. To facilitate the interpretation of the principal functions, we transformed them into their traction force equivalents,

$$\boldsymbol{\Xi}(\boldsymbol{\xi}) = [2/\langle L\rangle]\,\mathcal{F}^{-1}(A_{\alpha\beta}\,Q^{T*-1}_{\alpha\beta}\,\widehat{\boldsymbol{\varphi}}_{\alpha\beta})(\boldsymbol{\xi}), \tag{4.7}$$

where $\langle\,\rangle$ denotes temporal average and $\langle L\rangle$ is the average cell length.

The principal functions are mutually orthonormal with respect to the inner product (i.e. $\{\boldsymbol{\psi}_i, \boldsymbol{\psi}_j\} = 1$ if $i = j$ and zero otherwise), so that the total strain energy is given by

$$U_S(t) = \sum_{k=1}^{N} |a_k(t)|^2 = \sum_{k=1}^{N} U_S^k(t). \tag{4.8}$$

This property allows us to evaluate the instantaneous contribution of each term of the sum to the strain energy, $U_S^k(t) = |a_k(t)|^2$. The time-averaged contribution of each component is usually referred to as the *principal value* associated to the component, λ_k. The principal components are arranged in decreasing order of λ_k, (i.e. $\lambda_{k+1} < \lambda_k$). The relative

contribution of each principal component to the strain energy is obtained from the ratio $\nu_k = \lambda_k / \langle U_S \rangle$. The defining property of PCA is that, when applied to the U_S square-root (Eq. 4.3), it distributes the maximum amount of strain energy in the fewest possible number of principal components [160].

It is important to point out that other PCA methods involve the subtraction of the average of the observations prior to computation. This subtraction can be motivated by inaccuracies in the baseline of the observations, which is not our case, since both $\boldsymbol{\tau}(\mathbf{x})$ and $\mathbf{u}(\mathbf{x})$, and thus $\boldsymbol{\theta}(\mathbf{x})$, decay to zero far from the cell (Fig. 4.1). Thus, we have performed PCA without subtracting the average of the observations, a procedure already reported in the literature [161], and which in our case leads to the maximization of the strain energy accounted for by each component. We have tested PCA using both approaches (subtracting and not subtracting the average), and found similar components, although their order could in some cases be shifted. The correlations between components are unaffected.

4.1.4 Individual and Global PCA

We applied PCA to the time history of $\boldsymbol{\theta}(\boldsymbol{\xi}, t)$ for 1) each single cell (*individual* PCA), and 2) for a pooled set of observations coming from all the cells recorded in our experiments (*global* PCA). The high computational cost of performing *global* PCA to all the cells (10468 observations from $N = 24$ cells) led us to consider 10 different sets, each of them containing 600 observations evenly distributed among each cell. Comparing the principal components obtained from individual and global PCA allowed us to determine the cell-to-cell reproducibility of the principal components of shape and strain energy.

4.2 Traction force components in wild-type cells and reproducibility

We applied PCA (see Materials and Methods) to determine the dominant strain energy components exerted by *WT Dictyostelium* cells migrating chemotactically. These principal components were found to be reproducible from cell to cell, as well as representative of the cell line. We identified a set of five strain energy components which consistently appeared among the most important ones in a very large proportion of cells for *individual* PCA and in a 100% of the pools of observations considered for *global* PCA (Fig. 4.2b). We will refer to these dominant components as canonical principal components of the strain energy, or CPCs. Altogether, the five CPCs accounted for $\approx 60\%$ of the strain energy

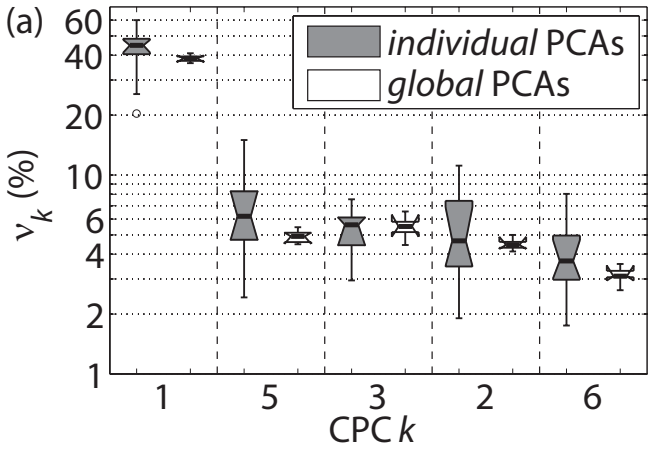

(b)

CPC k	1	2	3	4	5
% cells realizing mode k in *individual* PCA	100	92	75	83	96
% cells realizing mode k in *global* PCA	100	100	100	100	100

Figure 4.2: Contribution and degree of repeatibility of each canonical principal component (CPC) of the strain energy to the total strain energy U_S for WT cells. (A) Box-plots of the fraction of U_S accounted for by each CPCk, ν_k ($k = 1 - 5$), in *individual* and *global* PCA. (B) Percentage of the cells (for *individual* PCA) and percentage of the pools of observations (for *global* PCA) in which each CPCk was identified ($k = 1 - 5$). For *individual* PCA: $N = 24$ cells. For *global* PCA: $N = 10$ pools of data with 600 observations each.

exerted by migrating WT cells. Each CPC presented a similar average value of ν_k in both *individual* and *global* PCA (Fig. 4.2a). The narrow distribution of ν_k for *global* PCA indicated that each of the pools considered were representative of the whole cell line.

The spatial distributions of the five CPCs are shown in Fig. 4.3. The most important canonical principal component, CPC1, accounts for $\approx 40\%$ of the total strain energy exerted by WT cells (Fig. 4.2a). Fig. 4.3a displays CPC1 as $a_1|_{50}\,\boldsymbol{\Xi}_1(\boldsymbol{\xi})$, where $\boldsymbol{\Xi}_1(\boldsymbol{\xi})$ is the traction force corresponding to CPC1 (see Eq. 4.7) and $a_1|_{50}$ is the median of its weight coefficient. CPC1 depicts the cell attaching at both its anterior and posterior parts and contracting the substrate inwards towards the centroid of the cell. The coefficient a_1, which modulated the magnitude of the traction forces in CPC1, was skewed towards positive values in 98.5% of the observations (see Fig. 4.4a), indicating that CPC1 accounted for a persistent contraction of the substrate from front and back.

Unlike the first principal component, the weight coefficients of CPC2-5 were centered around zero (see Fig. 4.4b-e). This result motivated the distinction between (+) and (−)

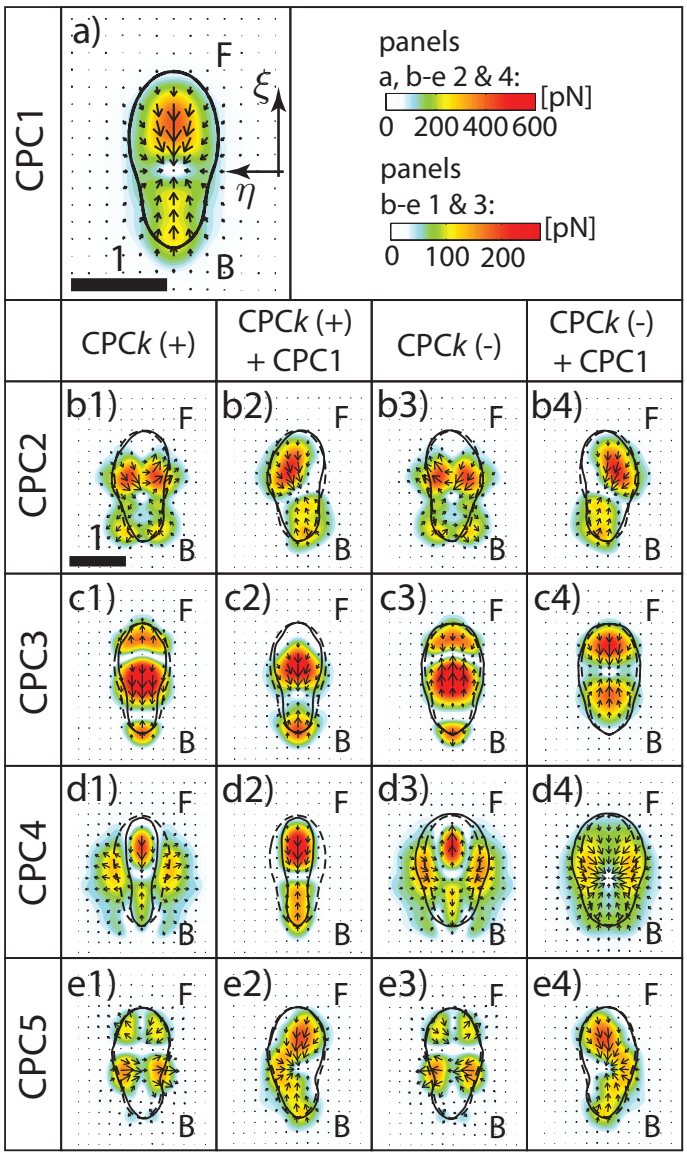

Figure 4.3: Canonical principal components of the strain energy (CPC) identified in *WT* cells. The panels in this figure come from a particular pool of observations over which *global* PCA was applied and represent the traction force equivalents to each strain energy component (Eq. 4.7). CPC1 is represented in (A) and CPCk (k=2-5) in (B-E). (B1/3-E1/3) (+)/(-) configuration of CPC2-5. (B2/4-E2/4) Overall ffect of CPC2-5 (+)/(-) on CPC1. The colormap indicates the magnitude and the arrows the direction of the traction forces (colorbars for each panel in top-right corner, in pN). The solid black contour indicates the cell shape associated with each CPC. The dashed black contour indicates the median cell shape associated with component 1. In top-right corner: x and y are the dimensionless axes for all panels. Scale bars: 1 dimensionless unit of length = half-length of the cell (see panels indicated). Letters "F" and "B" denote the front (anterior region) and back (posterior region) of the cell respectively.

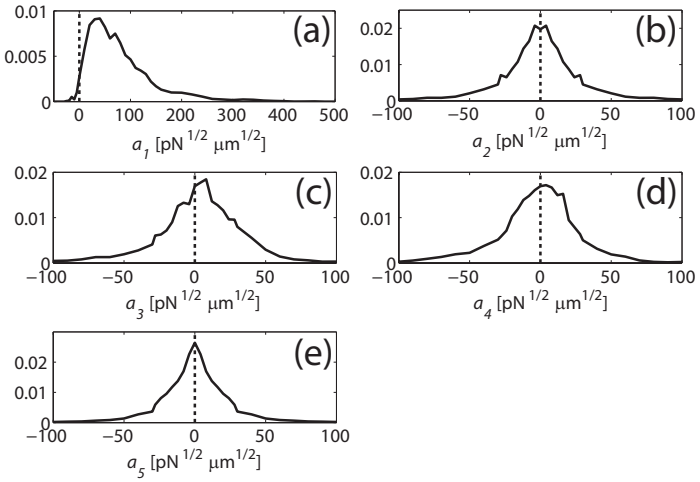

Figure 4.4: (A-E) PDF of the weight coefficients of each canonical principal component CPCk, a_k ($k = 1 - 5$), for the pool of all the observations ($N_{observations} = 10468$) coming from *individual* PCA applied over each WT cell ($N = 24$).

configurations of these components (see Fig. 4.3b1-f1 and b3-f3). Because of both the high proportion of U_S accounted for by CPC1 and the marked skewness of its weight coefficient towards positive values, it was useful to determine the perturbation effect that each CPCk (k=2-5) had on the first principal component. Fig. 4.3b2-f2 displays the addition of CPCk (+) to CPC1 as

$$a_1|_{50}\,\boldsymbol{\Xi}_1(\boldsymbol{\xi}) + a_k|_{90}\,\boldsymbol{\Xi}_k(\boldsymbol{\xi}), \tag{4.9}$$

and Fig. 4.3b4-f4 displays the addition of CPCk (−) to CPC1 as

$$a_1|_{50}\,\boldsymbol{\Xi}_1(\boldsymbol{\xi}) + a_k|_{10}\,\boldsymbol{\Xi}_k(\boldsymbol{\xi}) \approx a_1|_{50}\,\boldsymbol{\Xi}_1(\boldsymbol{\xi}) - a_k|_{90}\,\boldsymbol{\Xi}_k(\boldsymbol{\xi}). \tag{4.10}$$

The percentiles 10 and 90 of a_k were chosen to facilitate the visualization of the effect that CPC2-5 had in the overall traction force pattern, which was dominated by CPC1.

CPC2 and CPC5 were respectively responsible for $\approx 6\%$ and 3% of the strain energy exerted by WT cells (Fig. 4.2a) and accounted for lateral asymmetries in their traction forces. These components were associated with the bending of cell shape due to projection of pseudopods not aligned with the longitudinal axis of the cell (Fig. 4.3b and e respectively). The overall effect of CPC2 (+)/(−) (Fig. 4.3 b1/b3) was to displace the region of application of traction forces towards the right/left at the back of the cell, and towards the left/right at the front. At the front, the cell shape displaced towards the right/left, not exerting significant forces, thus suggesting that the front was not attached. CPC5 (+)/(−) was similar to CPC2 (+)/(−), but presented an net enhancement of the contractile traction

forces at the front (Fig. 4.3 e2 and e4), which suggests that the front was attached to the substrate, in contrast to CPC2.

CPC3 was responsible for $\approx 6\%$ of the strain energy exerted by cells (Fig. 4.2a). The (+)/(−) configuration of CPC3 depicted the contraction/stretch of the substrate from center to back and stretch/contraction of it from front to center (Fig. 4.3 c1/c3). The effect of CPC3 on the traction force pattern was easier to understand when added up to CPC1 (Fig. 4.3c2/c4). CPC3 (+)/(−) displaced the areas of contraction of the substrate towards the back/front of the cell. The cell shape associated with CPC3 (+)/(−) was a slight elongation/dilation (see dashed black line in Fig. 4.3c).

CPC4 (Fig. 4.3d) accounted for $\approx 5\%$ of the total strain energy (Fig. 4.2a). The (+)/(−) configuration of CPC4 accounted for an increase/decrease in the strength of the contractile forces at front and back, and a decrease/increase of the contractile lateral forces at the sides of the cell. CPC4 (+)/(−) was associated with the elongation/dilation of the cell shape.

4.3 The temporal modulation of one component captures the temporal dynamics of both the strain energy U_S exerted by cells and cell length L

Previous studies showed that U_S and L are positively correlated [35, 36], uncovering a link between cell shape and the traction work exerted by motile cells. However, the specific mechanical actions that the cell performs on the substrate, and which originate this relationship remained unclear. The aim of this section to dissect the potential connections between global cell shape, strain energy and each of the principal components determined with PCA. For this purpose, we analyzed the Spearman's rank correlation coefficient between the weight coefficient of CPCk, a_k, and either U_S or L ($r_{U_S-a_k}$ or r_{L-a_k}, $k = 1-5$), computed from *individual* PCA (see Fig. 4.5).

The PDF of $r_{U_S-a_1}$ was clearly displaced towards high positive values ($\langle r_{U_S-a_1}\rangle \approx 0.9$, p$< 10^{-5}$, Fig. 4.5b), indicating that the temporal evolution of U_S was accurately described by the temporal dynamics of CPC1. The weight coefficients a_k for components $k = 2-5$ showed no correlation with U_S, collapsing to zero for the asymmetric components $k = 2$ and 5. The PDF of r_{L-a_1} showed a statistically significant positive correlation (p=0.007, Fig. 4.5c), which together with the high correlation between U_S and CPC1,

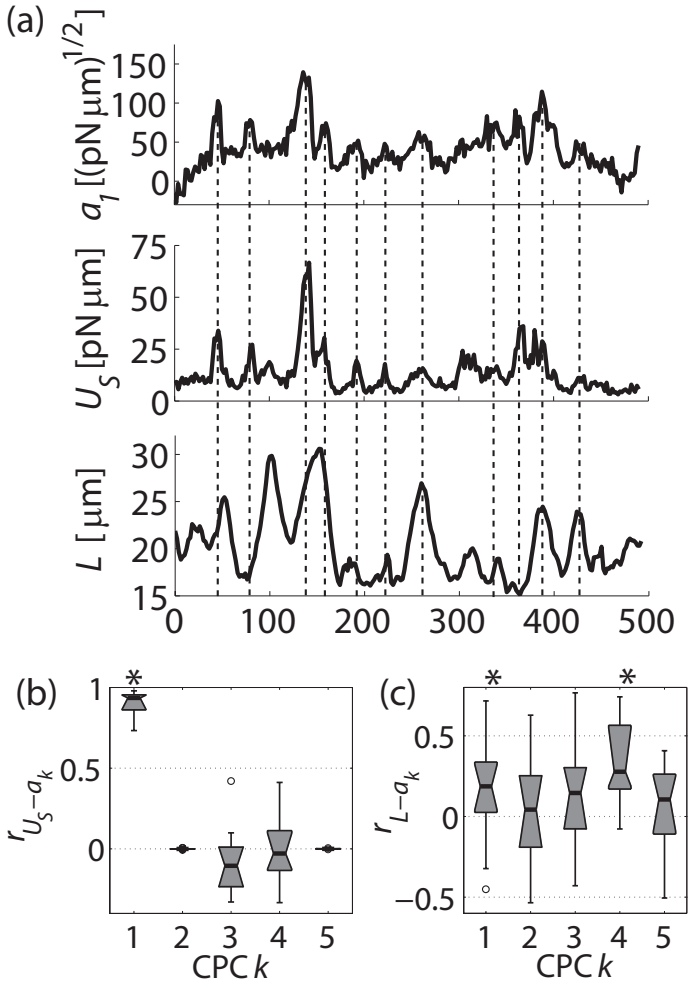

Figure 4.5: The weight coefficient of CPC1, a_1, correlates with both the strain energy exerted U_S and the cell length L. (A) For a WT cell, temporal evolution of a_1 (top panel), U_S (middle panel), L (bottom panel), as an example of the correlation between these functions. (B) Box-plot of the Spearman's rank correlation coefficient between the weight coefficient of the 5 CPCs identified, $a_k(t)$ $(k = 1 - 5)$, and U_S. (C) Box-plot of the Spearman's rank correlation coefficient between $a_k(t)$ $(k = 1 - 5)$ and L. Legend of the sign test of the null hypothesis that the statistical distributions in panels (A-B) have zero median: $*$ = p<0.01.

indicates that the modulation of the inward contraction of the substrate from front and back of the cell was responsible for the positive correlation between U_S and L [35, 36]. Weight coefficient a_4 and L were also positively correlated (p= 4×10^{-5}), due to the fact that CPC4 was an aspect ratio component that accounted for changes in traction forces related to the dilation and elongation of the cell (Eq. 3.3, Fig. 4.3 d). The 2D-PDFs of a_k $(k = 2 - 5)$ versus a_1 (Fig. 4.6) showed that the weight of CPC2-5 was bounded by

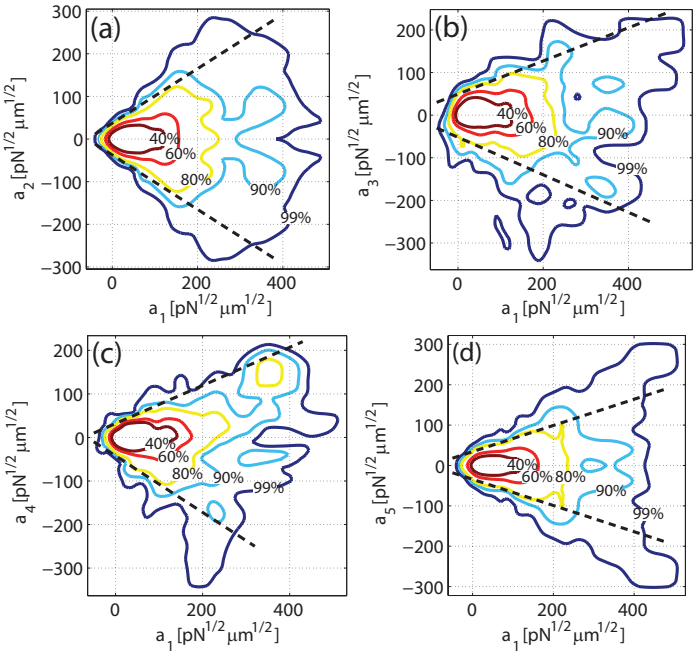

Figure 4.6: The weight of canonical strain energy components (CPC) 2 to 5 is bounded by the weight of CPC1. (A-E) 2D-PDFs of the weight coefficient of CPCk, $a_k(t)$ ($k = 2-5$), versus the weight coefficient of CPC1, a_1, for the pool of all the observations ($N_{observations} = 10468$) coming from *individual* PCA applied over each *WT* cell ($N = 24$). Solid lines represent the contours containing 40% (dark red), 60% (red), 80% (yellow), 90% (light blue) and 99% (blue) of the data. The dashed black lines indicate the approximate envelope of each 2D-PDF for a_k-a_1 ($k = 2-5$).

the weight of CPC1. This result confirmed that the first principal component governed the mechanics of amoeboid motility.

4.4 Temporal and spatial coherence are captured by the first strain energy component and degraded in higher components

We analyzed the temporal behavior of the principal components of the strain energy, finding that its coherence decreased and eventually became random from low- to high-order components (that is, for components with decreasing values of ν_k).

Temporal coherence was quantified for *individual* PCA using the autocorrelation of the weight coefficients of each component, $R_{a_k}(\tau) = \langle a_k(t)\, a_k(t+\tau)\rangle$. We obtained the parabolic fit to the first 10 s of positive lag of R_{a_k}, and calculated the time t_{R0} at

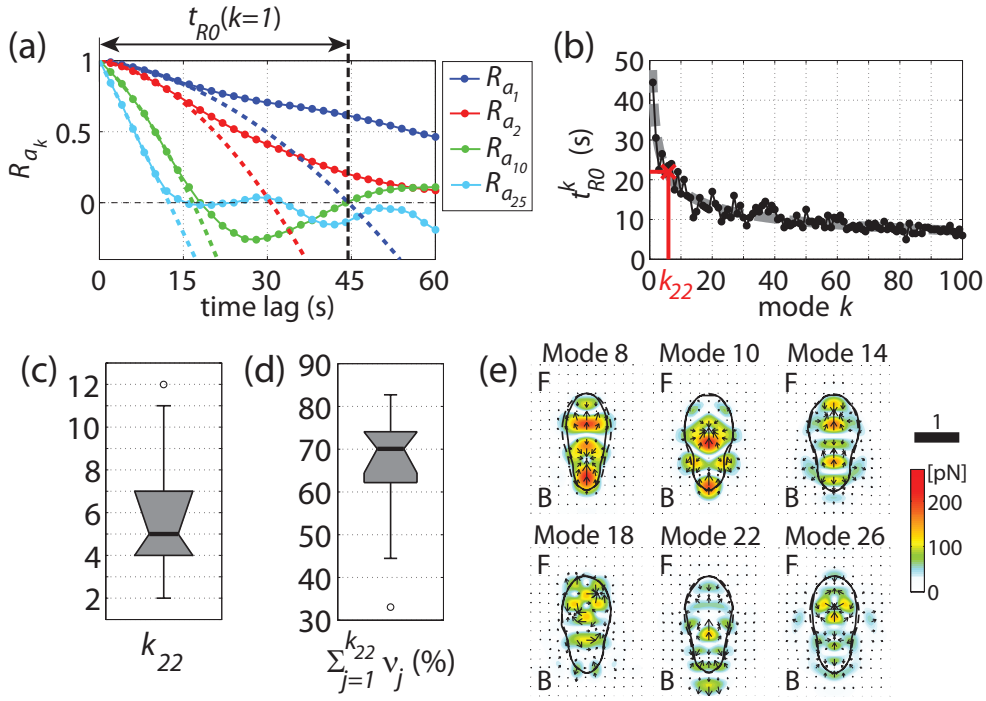

Figure 4.7: Loss of temporal (in A-D) and spatial (in E) coherence in high components (in *individual* PCA). (A) For a *WT* cell, autocorrelation of the weight coefficient of strain energy component k (R_{a_k}) represented as lines with circles for $k = 1$ (blue), 2 (red), 10 (green) ad 25 (light blue). Dashed lines represent the parabola fitting to R_{a_k} for time lag 0-10 s. The intersection of the parabola with the axis $R_{ak} = 0$ determines the scale for temporal decay of component k ($t_{R0}(k)$). (B) For the same cell, $t_{R0}(k)$ (black line with circles). The dashed grey line is the power law fit to $t_{R0}(k)$ (p_{R0}). The dashed red lines and cross mark the component for which p_{R0} has decayed to a threshold of 22 s (k_{22}), providing with a quantification for the component for loss of temporal coherence for this cell. (C) Box-plot of k_{22} for *WT* cells ($N = 24$). (D) Box-plot of the percentage of strain energy exerted with components 1 to k_{22}, $\sum_{j=1}^{k_{22}} \nu_k$, for *WT* cells ($N = 24$). (E) Loss of spatial coherence. Traction force components 8, 10, 14, 18, 22 and 26 for the same *global* PCA of *WT* used to represent CPCs in Fig. 4.3. Compare to CPCs (Fig. 4.3) to appreciate the decrease in size and directional coherence in higher strain energy components.

which that parabola crossed the axis $R_{a_k} = 0$, providing with an estimated time for loss of temporal coherence for component k (Fig. 4.7a). We then calculated the component k_{22} above which $t_{R0}(k)$ becomes lower than 22 s using a power law fit (Fig. 4.7b). The temporal threshold of 22 s was chosen because it is the average duration of the shortest phase of the motility cycle for *WT* cells [protrusion, see ref. 36]. Analysis of k_{22} indicated that temporal correlation is lost in average for principal components with $k = 5$ and higher (Fig. 4.7c). We also computed statistics of the proportion of U_S exerted with strain energy components 1 to k_{22}, $\sum_{j=1}^{k_{22}} \nu_k$, showing that $\approx 70\%$ of U_S was exerted with components presenting a

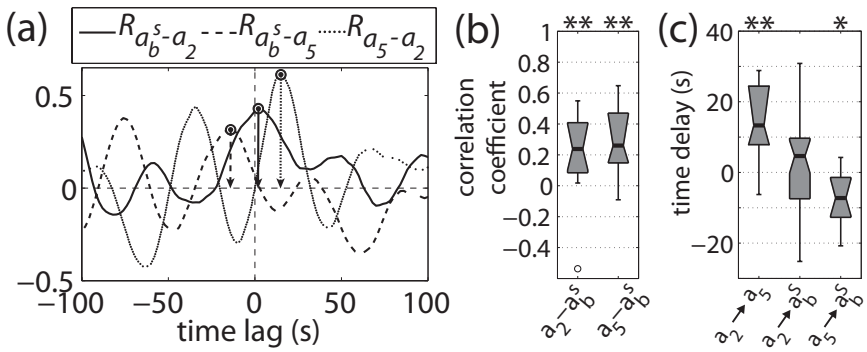

Figure 4.8: Analysis of the temporal coordination between cell shape bending and the two asymmetric canonical principal components of the strain energy, CPC2 and CPC5. (A) For a *WT* cell, cross-correlations between the bending of the cell (weight coefficient a_b^s), CPC2 (weight coefficient a_2) and CPC5 (weight coefficient a_5), used to quantify the delay between the signals (indicated with solid circles). (B) Box-plot of the Spearman's rank correlation coefficient between: a_2 and a_b^s, and a_5 and a_b^s. (C) Box-plot of the time delay, in s, between different weight coefficients, as extracted from their cross-correlations (see panel (A)) ($a_x \to a_y$ = time delay of a_y with respect to a_x). Legend of the sign test of the null hypothesis that the statistical distributions in panels (B-C) come from a continuous distribution with zero median: $*$ = p<0.05 and $**$ = p<0.01.

temporally coherent evolution (Fig. 4.7c). Thus, the remaining $\approx 30\%$ of U_S was exerted without a clear temporal signature and may be considered as temporally random, due either to intrinsic noise in the system under study, experimental noise, or the occurrence of fast events we could not capture in our experiments. According to these estimations, $\approx 85\%$ of the fraction of U_S exerted with a coherent temporal pattern is captured by the first five CPCs (Fig. 4.3), and $\approx 60\%$ of it is captured by CPC1 alone.

Parallel to the loss of temporal coherence, we observed that the spatial features of the strain energy components became smaller and lacked a clear structure for increasing components (Fig. 4.7 e). This decrease in both temporal and spatial coherence for higher strain energy components reinforces the argument that the five CPCs presented in the last subsection (Fig. 4.3), and specially CPC1, are enough to account for most of the mechanical work exerted by migrating cells on the ECM.

4.5 Temporal coordination between traction forces and lateral protrusions

The two asymmetric canonical principal components, CPC2 and CPC5, were found to be associated with lateral protrusion of pseudopods. CPC5 accounts for the cell attaching

the lateral protrusion to the substrate (Fig. 4.3b), whereas in CPC2 the lateral protrusion is not attached (Fig. 4.3b). The aim of this section was to analyze the possible temporal coordination between these two components, and how they are coordinated with the resulting bending of cell shape. The results from this analysis showed that the protrusion of lateral pseudopods takes about 12 s in average, starting with the lateral protrusion leading to the bending of cell shape and finishing with the attachment of the pseudopod to the substrate.

Application of PCA only to cell shape, similar to Killich et al. [24] and Keren et al. [22], provided with a set of cell shape components. One of them accounts directly for cell bending and is temporally described by its weight coefficient $a_b^s(t)$. The PDFs of the Spearman's rank correlation coefficient between a_b^s and either a_2 or a_5 (Fig. 4.8 b) proved that the association between cell shape bending and both CPC2 and CPC5 was positive and statistically significant. We studied the temporal coordination of cell shape bending, CPC2, and CPC5 through analysis of the cross-correlation of their weight coefficients and their temporal delays (Fig. 4.8a and c), showing that CPC5 is delayed ≈ 12 s with respect to CPC2 (p=0.004) (Fig. 4.8a and c, first boxplot) and that the physical bending of the cell precedes CPC5 by ≈ 7 s (p=0.0015) (Fig. 4.8a and c, third boxplot). Although Fig. 4.8c (third box-plot) suggests that CPC2 precedes the bending of the cell by ≈ 4 s, the statistical significance was marginal (p=0.09), probably because this delay was close to the temporal resolution of our experiments, 2 s.

4.6 Traction force components in contractility mutants are similar to those in wild-type cells

To investigate the role that MyoII contractility plays in the strain energy components we applied PCA to recordings of 1) MyoII essential light chain null cells with altered MyoII motor function [67] ($mlcE^-$, N=13), and 2) MyoII null cells lacking MyoII cross-linking and motor function [82] ($mhcA^-$ N=19).

Applying both *global* and *individual* PCA (see Materials and Methods) to recordings of traction forces and cell shape for both $mhcA^-$ and $mlcE^-$ cells, we identified five CPCs for each mutant cell line. These principal components, specially in $mlcE^-$, were remarkably similar to those identified for WT cells (Fig. 4.11 for $mlcE^-$, and 4.12 for $mhcA^-$ in the Supporting Material), and accounted for $\approx 55\%$ of U_S exerted by $mlcE^-$ and $mhcA^-$ (Fig. 4.10a in the Supporting Material).

As in WT cells, CPC1 accounted for a substantial proportion of the strain energy ($\approx$

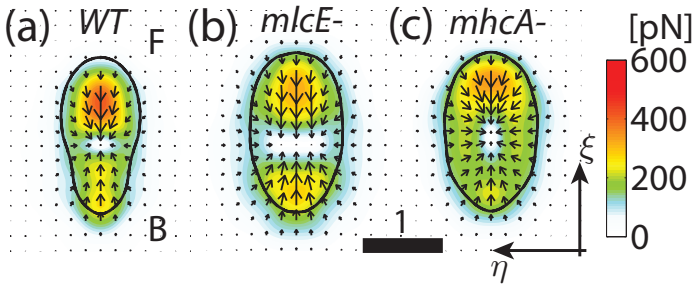

Figure 4.9: Canonical strain energy component 1 (CPC1) identified for (A) *WT*, (B) $mlcE^{-}$ and (C) $mhcA^{-}$ cells (as extracted from a particular *global* PCA). They are presented as their traction force equivalents (Eq. 4.7). The colormap and the arrows indicate the magnitude (in pN) and direction of the traction forces respectively. The solid black contour indicates the median cell shape associated with this component. See Eq. 4.7 for further explanation of the representation. x and y are the dimensionless axes. Scale bar: 1 dimensionless unit of length = half-length of the cell. Letters "F" and "B" denote the front (anterior region) and back (posterior region) of the cell respectively.

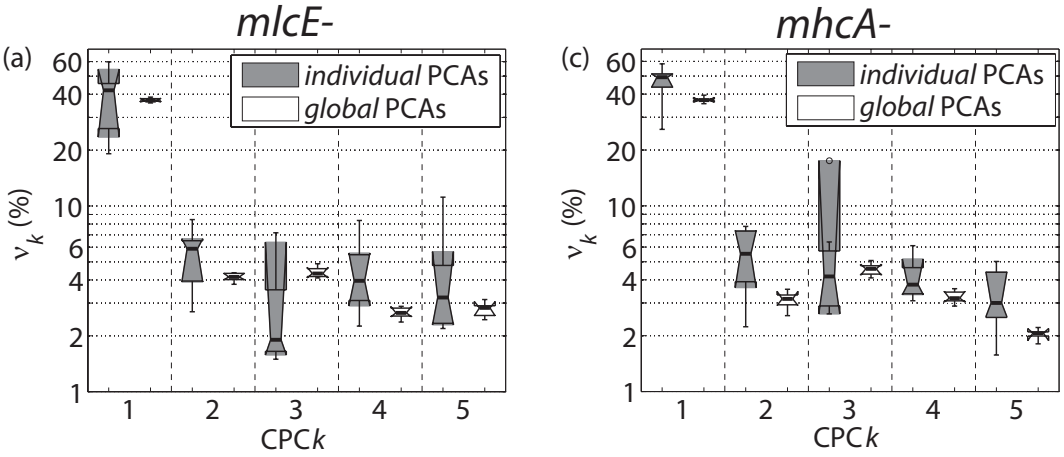

CPC k	1	2	3	4	5
% cells realizing mode k in *individual* PCA	100	92	77	92	92
% cells realizing mode k in *global* PCA	100	100	100	100	100

CPC k	1	2	3	4	5
% cells realizing mode k in *individual* PCA	100	63	37	47	89
% cells realizing mode k in *global* PCA	100	100	100	100	100

Figure 4.10: For contractility mutants $mlcE^{-}$ (panels A and B) and $mhcA^{-}$ cells (panels C and D), contribution and degree of repeatibility of each canonical principal component of the strain energy (CPC) to the total strain energy U_S. (A) and (C) Box-plots of the fraction of U_S accounted for by each CPCk, ν_k ($k = 1 - 5$), in *individual* and *global* PCA. (B) and (D) Percentage of the cells (for *individual* PCA) and percentage of the pools of observations (for *global* PCA) in which each CPCk was identified ($k = 1 - 5$). For *individual* PCA: $N = 13$ $mlcE^{-}$ cells and $N = 19$ $mhcA^{-}$ cells. For *global* PCA: $N = 10$ pools of data with 600 observations each for both $mlcE^{-}$ and $mhcA^{-}$ cells.

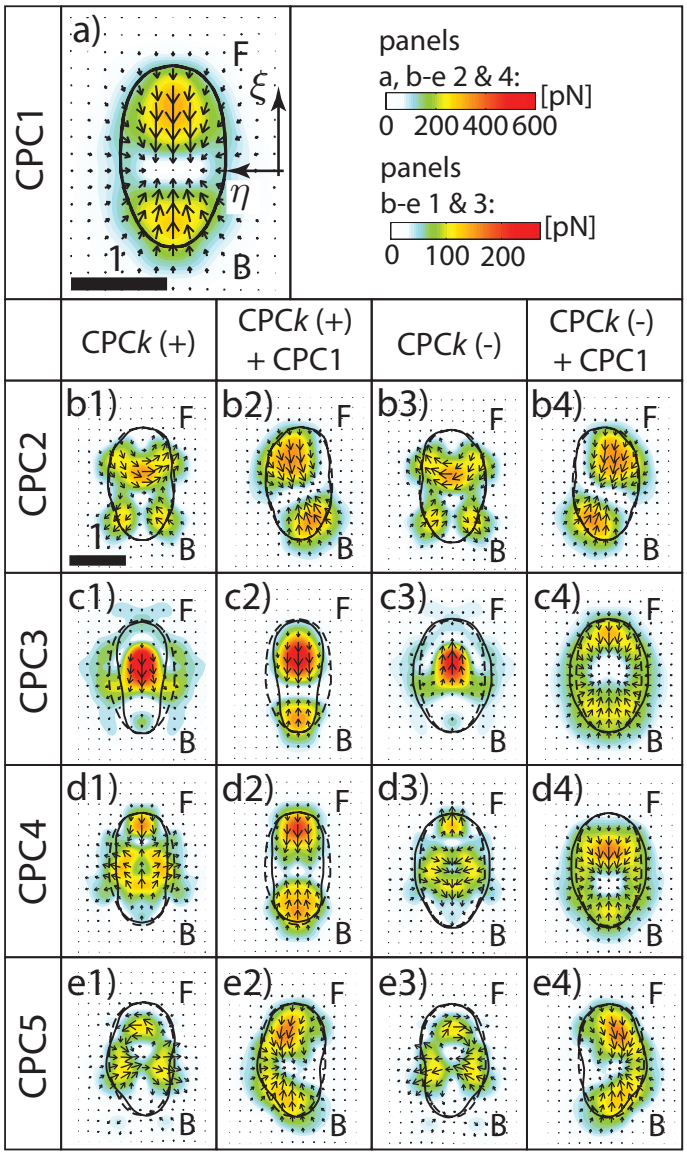

Figure 4.11: Canonical principal components of the strain energy (CPC) identified in $mlcE^{-}$ cells. The panels in this figure come from a particular pool of observations over which *global* PCA was applied and represent the traction force equivalents to each strain energy component (Eq. 4.7). CPC1 is represented in (A) and CPCk (k=2-5) in (B-E). (B1/3-E1/3) (+)/(-) configuration of CPC2-5. (B2/4-E2/4) Overall ffect of CPC2-5 (+)/(-) on CPC1. The colormap indicates the magnitude and the arrows the direction of the traction forces (colorbars for each panel in top-right corner, in pN). The solid black contour indicates the cell shape associated with each CPC. The dashed black contour indicates the median cell shape associated with component 1. In top-right corner: x and y are the dimensionless axes for all panels. Scale bars: 1 dimensionless unit of length = half-length of the cell (see panels indicated). Letters "F" and "B" denote the front (anterior region) and back (posterior region) of the cell respectively.

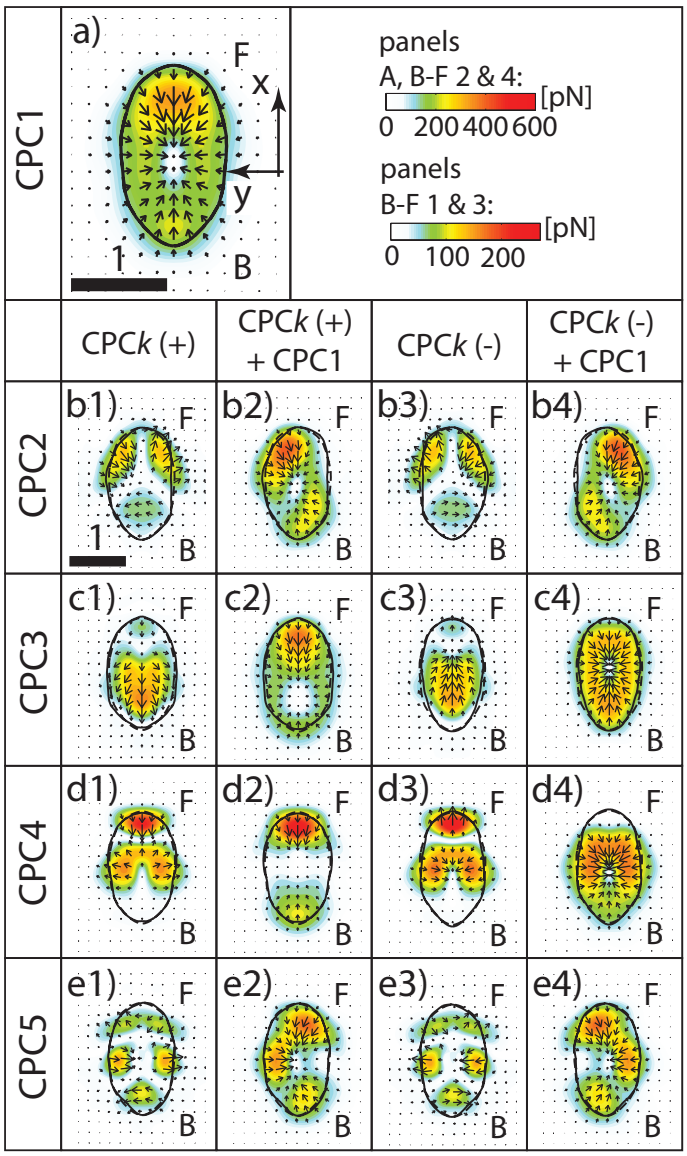

Figure 4.12: Canonical principal components of the strain energy (CPC) identified in $mhcA^-$ cells. The panels in this figure come from a particular pool of observations over which *global* PCA was applied and represent the traction force equivalents to each strain energy component (Eq. 4.7). CPC1 is represented in (A) and CPCk (k=2-5) in (B-E). (B1/3-E1/3) (+)/(-) configuration of CPC2-5. (B2/4-E2/4) Overall ffect of CPC2-5 (+)/(-) on CPC1. The colormap indicates the magnitude and the arrows the direction of the traction forces (colorbars for each panel in top-right corner, in pN). The solid black contour indicates the cell shape associated with each CPC. The dashed black contour indicates the median cell shape associated with component 1. In top-right corner: x and y are the dimensionless axes for all panels. Scale bars: 1 dimensionless unit of length = half-length of the cell (see panels indicated). Letters "F" and "B" denote the front (anterior region) and back (posterior region) of the cell respectively.

40%) in both $mlcE^-$ and $mhcA^-$ cells, indicating that temporal evolution of the mechanical interaction between contractility mutants and their substrate was also dynamically simple in these mutants. However, the principal components with $k > 1$ were less reproducible from cell to cell (Fig. 4.10b in the Supporting Material) than in *WT*, indicating the difficulty to define a clear "mechanical phenotype" for this cell line.

The first principal component in $mlcE^-$ was very similar to that in *WT* cells (Fig. 4.3a1 and 4.9 a), with traction forces focused at two areas at the posterior and anterior parts of the cell. However, this was not the case in $mhcA^-$ cells, where CPC1 presented a large amount of lateral forces (Fig. 4.9b). The prominent exertion of lateral forces by $mhcA^-$ is present throughout all the components (Fig. 4.12 in the Supporting Material).

4.7 Discussion

Shape changes in motile cells are strongly related with the modulation of cell adhesions to the substrate via the forces they exert on it [36, 143–146]. In order to study this modulation, we measured the traction forces and cell shape of *Dictyostelium* cells migrating chemotactically over a flat elastic substrate. We then applied a tailored formulation of PCA that optimized the mechanical work exerted by these cells. In addition, we used a cell-based coordinate system and a 2D mapping of cell shape to obtain the different shape changes associated with each strain energy component, thus allowing for a physical interpretation of the dominant strain energy components.

This analysis determined a set of five canonical principal components of the strain energy (CPCs) that were reproducible from cell to cell, and which captured $\approx$ 60% of the total mechanical work exerted by cells. The time evolution of these components was observed to remain temporally coherent for a period of time equal to the duration of pseudopod protrusions and retractions. The most important component accounted for $\approx$ 40% of U_S, presenting an oscillatory temporal evolution which correlated with both the strain energy and global cell shape. This component depicted the cell attaching at front and back, contracting the substrate inward towards its center, consistent with previous traction force measurements [34–36]. The rest of the components were substantially less important in terms of mechanical energy, accounting for less than 7% each.

Keren et al. [22] showed that a low number of components described the shape variability of migrating keratocytes within a population. In their cells, the most important

component behaved steadily in time. The present study illustrates that PCA is also able to compress the more complex dynamics of amoeboid migrating cells using a reduced number of degrees of freedom with coherent temporal evolution. For instance, PCA identified two modes related with the initiation and termination of lateral protrusions. These components were separated by a period of ≈ 12 s, during which an increase of traction forces revealed the formation of new adhesions.

The canonical principal components were found to be similar in the case of mutants with contractile deficiencies ($mlcE^-$ and $mhcA^-$), although these components were less reproducible in $mhcA^-$ cells, indicating they have a less clear "mechanical phenotype". The first component in $mhcA^-$ cells presented high lateral forces, suggesting a cortical origin of the traction forces in the absence of MyoII.

By compressing the mechanics of motile cells into a reduced set of temporally resolved degrees of freedom, the present study may contribute to refined models of cell migration [147–150] that incorporate mechanical cell-substrate interactions. For instance, the model of adhesion and contraction developed by Buenemann et al. [149] for *Dictyostelium* cells, could benefit from the present empirical description. Models that were originally formulated for other cell types [147] could potentially be adapted to amoeboid cells based on the principal components identified in this study.

Chapter 4, in part, has been submitted for publication in the *Biophysical Journal*, "An oscillatory contractile pole-force mode dominates the traction forces exerted by migrating amoeboid cells," by B. Alonso-Latorre, J. C. del Álamo, R. Meili, R. A. Firtel, and J. C. Lasheras (2010). The thesis author is the primary investigator in this publication.

Experiments were performed by Dr. R. Meili in the Section of Cell and Developmental Biology, University of California, San Diego. This investigation was partially funded by the U.S. National Institutes of Health.

Chapter 5

Advanced Fourier Traction Force Cytometry Assays for the Study of Mechanosensing

In the last years, abundant evidence has demonstrated that cell behavior is affected by the mechanical properties of the surrounding environment. For instance, it has been reported that mesenchymal stem cells differentiate according to substrate elasticity [162], or how cells increase their spread area as the substrate stiffness increases [95, 162]. In the recent years, an array of proteins localized at cell-substrate adhesions and playing a role in the mechanotransduction machinery have been identified (integrin, talin, α-actinin, FAK,...) [163], as well as candidate mechanical processes allowing cells to "feel" their mechanical environment [164]. However, we are still far from understanding comprehensively how cells probe the mechanical properties of the substrate (mechanosensing), how they transduce the output of that process into chemical signals (mechanotransduction), and how those chemical signals lead to a certain action or response (mechanoresponse).

In this chapter, we present the derivation of two different analytical solutions of the elastostatic equation (Eq. 2.17) under conditions of interest for the study of mechanosensing. Section 5.1 presents the solution of the elastostatic equation for a two-layered substrate. Observations on the obtained solution indicate that this configuration could be used to answer questions such as what is the lengthscale at which cells measure the mechanical properties of the substrate, or how deep they "feel" the bottom substrate in different conditions. Section 5.2 presents the solution of the elastostatic equation for a substrate with a

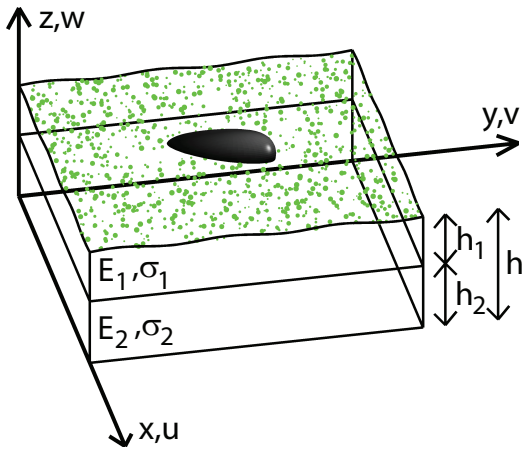

Figure 5.1: Sketch of the analytic assay of a two-layered substrate.

shallow spatial gradient of Young's modulus, which can be used for the analytical and experimental study of durotaxis, or the directed cell movement up or down a rigidity gradient [165, 166].

5.1 Solution of the elastostatic equation for a two-layered substrate

To study how cell traction forces are modified when a secondary substrate is located below the substrate to which the cell is attached, we solved the elastostatic equation for a two-layered substrate (1=upper layer, 2=lower layer) with thicknesses, h_1 and h_2, Young's moduli, E_1 and E_2, and Poisson's ratios, σ_1 and σ_2, respectively (Fig. 5.1). Layer 2 is assumed to be attached to an infinitely rigid substrate, and thus presents zero displacements at $z = 0$. Displacements are measured at $z = h_1 + h_2 = h$ in layer 1. We adopted a Cartesian coordinate system with the x and y axes parallel to the base of the substrate, located at $z = 0$.

The equation of static equilibrium are the ones governing the displacement field

$$\nabla^2 \mathbf{u} + \frac{\nabla (\nabla \cdot \mathbf{u})}{(1 - 2\,\sigma)} = 0. \tag{5.1}$$

which is exactly the same as Eq. 2.17. Boundary conditions for layer 1 are partially imposed using the displacements measured at the substrate free surface

$$\mathbf{u}_1(x, y, h) = \mathbf{u}^h(x, y). \tag{5.2}$$

For layer 2, we imposed zero displacements at the base of the substrate

$$\mathbf{u}_2(x, y, 0) = 0. \tag{5.3}$$

The set of neccessary boundary conditions is completed by imposing that both displacements and stresses are continuous across the interface between layers 1 and 2, located at $z = h_2$

$$\mathbf{u}_1(x, y, h_2) = \mathbf{u}_2(x, y, h_2), \tag{5.4}$$

$$\begin{aligned} \tau_{1,xz}(x, y, h_2) &= \tau_{2,xz}(x, y, h_2), \\ \tau_{1,yz}(x, y, h_2) &= \tau_{2,yz}(x, y, h_2), \\ \tau_{1,zz}(x, y, h_2) &= \tau_{2,zz}(x, y, h_2). \end{aligned} \tag{5.5}$$

The solution to Eq. 5.1 was obtained obtained in Section 2.2 in terms of the Fourier series of the displacements. For convenience, we re-express this solution (see Eq. 2.24) as a function of $z - z_0$ as:

$$\begin{bmatrix} \widehat{\mathbf{u}}_{\alpha\beta} \\ d\widehat{\mathbf{u}}_{\alpha\beta} \end{bmatrix} = P_{\alpha\beta} \, \exp\left(J_{\alpha\beta}\left(z - z_0\right)\right) \, P_{\alpha\beta}^{-1} \begin{bmatrix} \widehat{\mathbf{u}}_{\alpha\beta}^{z_0} \\ d\widehat{\mathbf{u}}_{\alpha\beta}^{z_0} \end{bmatrix} = \begin{bmatrix} L & M \\ N & O \end{bmatrix} \begin{bmatrix} \widehat{\mathbf{u}}_{\alpha\beta}^{z_0} \\ d\widehat{\mathbf{u}}_{\alpha\beta}^{z_0} \end{bmatrix} \tag{5.6}$$

where $\widehat{\mathbf{u}}_{\alpha\beta}^{z_0}$ and $d\widehat{\mathbf{u}}_{\alpha\beta}^{z_0}$ represent the Fourier coefficients of the displacements and their z-derivatives at a certain z-coordinate, z_0, respectively, and the components of the 3×3 matrices L, M, N, and O, expressed as functions of $Z = z - z_0$ are

$$L^{[1,1]} = \cosh(kZ) - 1/2\frac{\alpha^2 Z \sinh(kZ)}{k(-1 + 2\sigma)}, \tag{5.7}$$

$$L^{[1,2]} = -1/2\frac{\alpha\beta Z \sinh(kZ)}{k(-1 + 2\sigma)}, \tag{5.8}$$

$$L^{[1,3]} = 1/4i\alpha\frac{kZ\cosh(kZ) - \sinh(kZ)}{k(-1 + \sigma)}, \tag{5.9}$$

$$L^{[2,1]}(\alpha, \beta) = L^{[1,2]}(\beta, \alpha), \tag{5.10}$$

$$L^{[2,2]}(\alpha, \beta) = L^{[1,1]}(\beta, \alpha), \tag{5.11}$$

$$L^{[2,3]}(\alpha, \beta) = L^{[1,3]}(\beta, \alpha), \tag{5.12}$$

$$L^{[3,1]} = \frac{-1/2i\alpha\left(-kZ\cosh(kZ)+\sinh(kZ)\right)}{k(-1+2\sigma)}, \tag{5.13}$$

$$L^{[3,2]}(\alpha,\beta) = L^{[3,1]}(\beta,\alpha), \tag{5.14}$$

$$L^{[3,3]} = \cosh(kZ) + 1/4\frac{kZ\sinh(kZ)}{-1+\sigma}, \tag{5.15}$$

$$M^{[1,1]} = -1/4\frac{\alpha^2 Z\cosh(kZ)}{(-1+\sigma)k^2} + 1/4\frac{\left(-3k^2+4k^2\sigma-\beta^2\right)\sinh(kZ)}{k^3(-1+\sigma)}, \tag{5.16}$$

$$M^{[1,2]} = 1/4\frac{\alpha\beta\left(-Z\cosh(kZ)k+\sinh(kZ)\right)}{k^3(-1+\sigma)}, \tag{5.17}$$

$$M^{[1,3]} = \frac{1/2i\sinh(kZ)Z\alpha}{k(-1+2\,\sigma)}, \tag{5.18}$$

$$M^{[2,1]}(\alpha,\beta) = M^{[1,2]}(\beta,\alpha), \tag{5.19}$$

$$M^{[2,2]}(\alpha,\beta) = M^{[1,1]}(\beta,\alpha), \tag{5.20}$$

$$M^{[2,3]}(\alpha,\beta) = M^{[1,3]}(\beta,\alpha), \tag{5.21}$$

$$M^{[3,1]} = \frac{1/4i\alpha Z\sinh(kZ)}{k(-1+\sigma)}, \tag{5.22}$$

$$M^{[3,2]}(\alpha,\beta) = M^{[3,1]}(\beta,\alpha), \tag{5.23}$$

$$M^{[3,3]} = 1/2\frac{Z\cosh(kZ)}{-1+2\sigma} + 1/2\frac{(-3+4\sigma)\sinh(kZ)}{k(-1+2\sigma)}, \tag{5.24}$$

$$N^{[1,1]} = -1/2\frac{\alpha^2 Z\cosh(kZ)}{-1+2\sigma} + 1/2\frac{(-2k^2+4k^2\sigma-\alpha^2)\sinh(kZ)}{k(-1+2\sigma)}, \tag{5.25}$$

$$N^{[1,2]} = -1/2\frac{\alpha\beta Z\cosh(kZ)}{-1+2\sigma} - 1/2\frac{\beta\alpha\sinh(kZ)}{k(-1+2\sigma)}, \tag{5.26}$$

$$N^{[1,3]} = \frac{1/4i\sinh(kZ)kZ\alpha}{-1+\sigma}, \tag{5.27}$$

$$N^{[2,1]}(\alpha,\beta) = N^{[1,2]}(\beta,\alpha), \tag{5.28}$$

$$N^{[2,2]}(\alpha,\beta) = N^{[1,1]}(\beta,\alpha), \tag{5.29}$$

$$N^{[2,3]}(\alpha,\beta) = N^{[1,3]}(\beta,\alpha), \tag{5.30}$$

$$N^{[3,1]} = \frac{1/2i\sinh(kZ)kZ\alpha}{-1+2\sigma}, \tag{5.31}$$

$$N^{[3,2]}(\alpha,\beta) = N^{[3,1]}(\beta,\alpha), \tag{5.32}$$

$$N^{[3,3]} = 1/4\frac{k^2Z\cosh(kZ)+k(-3+4\sigma)\sinh(kZ)}{-1+\sigma}, \tag{5.33}$$

$$O^{[1,1]} = \cosh(kZ) - 1/4\frac{\alpha^2Z\sinh(kZ)}{k(-1+\sigma)}, \tag{5.34}$$

$$O^{[1,2]} = -1/4\frac{\beta\alpha\sinh(kZ)Z}{k(-1+\sigma)}, \tag{5.35}$$

$$O^{[1,3]} = \frac{1/2iZ\,\alpha\,\cosh(k\,Z)}{-1+2\,\sigma} + \frac{1/2i\alpha\sinh(kZ)}{k(-1+2\sigma)}, \tag{5.36}$$

$$O^{[2,1]}(\alpha,\beta) = O^{[1,2]}(\beta,\alpha), \tag{5.37}$$

$$O^{[1,1]}(\alpha,\beta) = O^{[2,2]}(\beta,\alpha), \tag{5.38}$$

$$O^{[2,3]}(\alpha,\beta) = O^{[1,3]}(\beta,\alpha), \tag{5.39}$$

$$O^{[3,1]} = \frac{1/4iZ\alpha\cosh(kZ)}{-1+\sigma} + \frac{1/4i\alpha\sinh(kZ)}{k(-1+\sigma)}, \tag{5.40}$$

$$O^{[3,2]}(\alpha,\beta) = O^{[3,1]}(\beta,\alpha), \tag{5.41}$$

$$O^{[3,3]} = \cosh(kZ) + 1/2\frac{kZ\sinh(kZ)}{-1+2\sigma}. \tag{5.42}$$

For layer 1, the solution in Eq. 5.6 can be expressed as

$$\begin{bmatrix} \widehat{\mathbf{u}}_{1,\alpha\beta} \\ d\widehat{\mathbf{u}}_{1,\alpha\beta} \end{bmatrix} = \begin{bmatrix} L_1 & M_1 \\ N_1 & O_1 \end{bmatrix} \begin{bmatrix} \widehat{\mathbf{u}}^h_{\alpha\beta} \\ d\widehat{\mathbf{u}}^h_{\alpha\beta} \end{bmatrix} \tag{5.43}$$

where $\widehat{\mathbf{u}}^h_{\alpha\beta}$ and $d\widehat{\mathbf{u}}^h_{\alpha\beta}$ represent the Fourier coefficients of the measured displacements at $z = h$ and their z-derivatives respectively, and matrices L_1, M_1, N_1, and O_1 are matrices L, M, N, and O evaluated at $z_0 = h$ and $\sigma = \sigma_1$. 3×3 matrices L_1, M_1, N_1, and O_1 are

For layer 2, the solution in Eq. 5.6 can be expressed as

$$\begin{bmatrix} \widehat{\mathbf{u}}_{2,\alpha\beta} \\ d\widehat{\mathbf{u}}_{2,\alpha\beta} \end{bmatrix} = \begin{bmatrix} M_2 \\ O_2 \end{bmatrix} \begin{bmatrix} d\widehat{\mathbf{u}}^0_{\alpha\beta} \end{bmatrix} \tag{5.44}$$

where $d\widehat{\mathbf{u}}^0_{\alpha\beta}$ represents the z-derivatives of the Fourier coefficients of the displacements at $z = 0$, and matrices L_2, M_2, N_2, and O_2 are matrices L, M, N, and O evaluated at $z_0 = 0$ and $\sigma = \sigma_2$. Notice that this expression includes the boundary condition in Eq. 5.3.

The boundary condition on the stresses at $z = h_2$ in Eq. 5.5 can be expressed as

$$\Gamma\,\widehat{\mathbf{u}}^{h_2}_{\alpha\beta} + \Theta\,d\widehat{\mathbf{u}}^{h_2}_{2,\alpha\beta} + \Upsilon\,d\widehat{\mathbf{u}}^{h_2}_{1,\alpha\beta} = 0 \tag{5.45}$$

where $\widehat{\mathbf{u}}^{h_2}_{\alpha\beta}$ are the Fourier coefficients of the displacements at the interface at $z = h_2$, and $d\widehat{\mathbf{u}}^{h_2}_{1,\alpha\beta}$ and $d\widehat{\mathbf{u}}^{h_2}_{2,\alpha\beta}$ are the z-derivatives of the Fourier coefficients of the displacements at $z = h_2$ in layer 1 and 2 respectively, and

$$\Gamma = \begin{bmatrix} 0 & 0 & i\alpha\left(E_r\frac{1+\sigma_1}{1+\sigma_2} - 1\right) \\ 0 & 0 & i\beta\left(E_r\frac{1+\sigma_1}{1+\sigma_2} - 1\right) \\ i\alpha\left(E_r\frac{(1+\sigma_1)(1-2\sigma_1)}{(1+\sigma_2)(1-2\sigma_2)}\sigma_2 - \sigma_1\right) & i\beta\left(E_r\frac{(1+\sigma_1)(1-2\sigma_1)}{(1+\sigma_2)(1-2\sigma_2)}\sigma_2 - \sigma_1\right) & 0 \end{bmatrix}, \tag{5.46}$$

$$\Theta = \begin{bmatrix} E_r\frac{1+\sigma_1}{1+\sigma_2} & 0 & 0 \\ 0 & E_r\frac{1+\sigma_1}{1+\sigma_2} & 0 \\ 0 & 0 & E_r\frac{(1+\sigma_1)(1-2\sigma_1)}{(1+\sigma_2)(1-2\sigma_2)}(1-\sigma_2) \end{bmatrix}, \tag{5.47}$$

and

$$\Upsilon = \begin{bmatrix} -1 & 0 & 0 \\ 0 & -1 & 0 \\ 0 & 0 & -(1-\sigma_1) \end{bmatrix}, \tag{5.48}$$

where E_r represents the ratio of Young's moduli E_2/E_1.

We then solve Eq. 5.43 for $d\widehat{\mathbf{u}}^{h_2}_{1,\alpha\beta}$

$$d\widehat{\mathbf{u}}^{h_2}_{1,\alpha\beta} = \left[N_1 - O_1\, M_1^{-1}\, L_1\right]_{z=h_2} \widehat{\mathbf{u}}^{h}_{\alpha\beta} + \left[O_1\, M_1^{-1}\right]_{z=h_2} \widehat{\mathbf{u}}^{h_2}_{\alpha\beta}, \tag{5.49}$$

and Eq. 5.44 for $d\widehat{\mathbf{u}}^{h_2}_{2,\alpha\beta}$

$$\widehat{d\mathbf{u}}^{h_2}_{2,\alpha\beta} = \left[O_2\, M_2^{-1}\right]_{z=h_2} \widehat{\mathbf{u}}^{h_2}_{\alpha\beta} \tag{5.50}$$

Substitution of Eqs. 5.49 and 5.50 into Eq. 5.45 leads to a system of three equations whose three unknowns are the components of $\widehat{\mathbf{u}}^{h_2}_{\alpha\beta}$. We then can solve for $d\widehat{\mathbf{u}}^{h}_{\alpha\beta}$ from Eq. 5.43 evaluated at $z = h_2$,

$$d\widehat{\mathbf{u}}^{h}_{\alpha\beta} = \left[M_1^{-1}\right]_{z=h_2} \left(\widehat{\mathbf{u}}^{h_2}_{\alpha\beta} - \left[L_1\right]_{z=h_2} \widehat{\mathbf{u}}^{h}_{\alpha\beta}\right), \tag{5.51}$$

and we apply the constitutive equations to calculate the traction stresses at $z = h$,

$$\begin{bmatrix} \widehat{\tau_{xz}}^{h}_{\alpha\beta} \\ \widehat{\tau_{yz}}^{h}_{\alpha\beta} \\ \widehat{\tau_{zz}}^{h}_{\alpha\beta} \end{bmatrix} = \frac{E}{2(1+\sigma_1)} \begin{bmatrix} 0 & 0 & \mathrm{i}\alpha & 1 & 0 & 0 \\ 0 & 0 & \mathrm{i}\beta & 0 & 1 & 0 \\ \frac{2\sigma_1 \mathrm{i}\alpha}{(1-2\sigma_1)} & \frac{2\sigma_1 \mathrm{i}\beta}{(1-2\sigma_1)} & 0 & 0 & 0 & \frac{2(1-\sigma_1)}{(1-2\sigma_1)} \end{bmatrix} \begin{bmatrix} \widehat{\mathbf{u}}^{h}_{\alpha\beta} \\ d\widehat{\mathbf{u}}^{h}_{\alpha\beta} \end{bmatrix} \tag{5.52}$$

The inverse Fourier transform of these coefficients yields the traction field on the substrate free surface,

$$[\tau_{xz}, \tau_{yz}, \tau_{zz}]_{z=h} = \sum_{\alpha=-\infty}^{\infty} \sum_{\beta=-\infty}^{\infty} \left[\widehat{\tau_{xz}}^{h}, \widehat{\tau_{yz}}^{h}, \widehat{\tau_{zz}}^{h}\right]_{\alpha\beta} \exp(i\alpha x) \exp(i\beta y). \tag{5.53}$$

5.1.1 Use of the two-layered substrate assay to study cell mechanosensing

Fig. 5.2 presents the spectral analysis of the solution for a two-layered substrate, and it shows that for wavenumbers $kh \gtrsim 3$ the solution for the two-layered substrate collapses with Boussinesq's solution for an infinitely thick substrate (as expected from the results in Section 2.3). Interestingly, when the bottom layer (layer 2) is less stiff than the top layer (layer 1), that is, when $E_r < 1$ (Fig. 5.2b), the comparison between the Frobenius norm of the transfer matrices for the two-layered substrate (thin solid lines) and Boussinesq's solution (dotted line) indicates that the apparent Young's modulus will be larger or smaller than the Young's modulus of layer 1, E_1, depending on the lengthscale at which the stresses are applied. As the wavenumber decreases below $kh \approx 3$, the norm of the transfer matrix of the two-layered substrate separates from Boussinesq's solution. In particular, for h_2/h_1=1, 10, and 100 (see legend) the norm of the transfer matrix goes below the one for Boussinesq's solution, indicating a lower apparent Young's modulus.

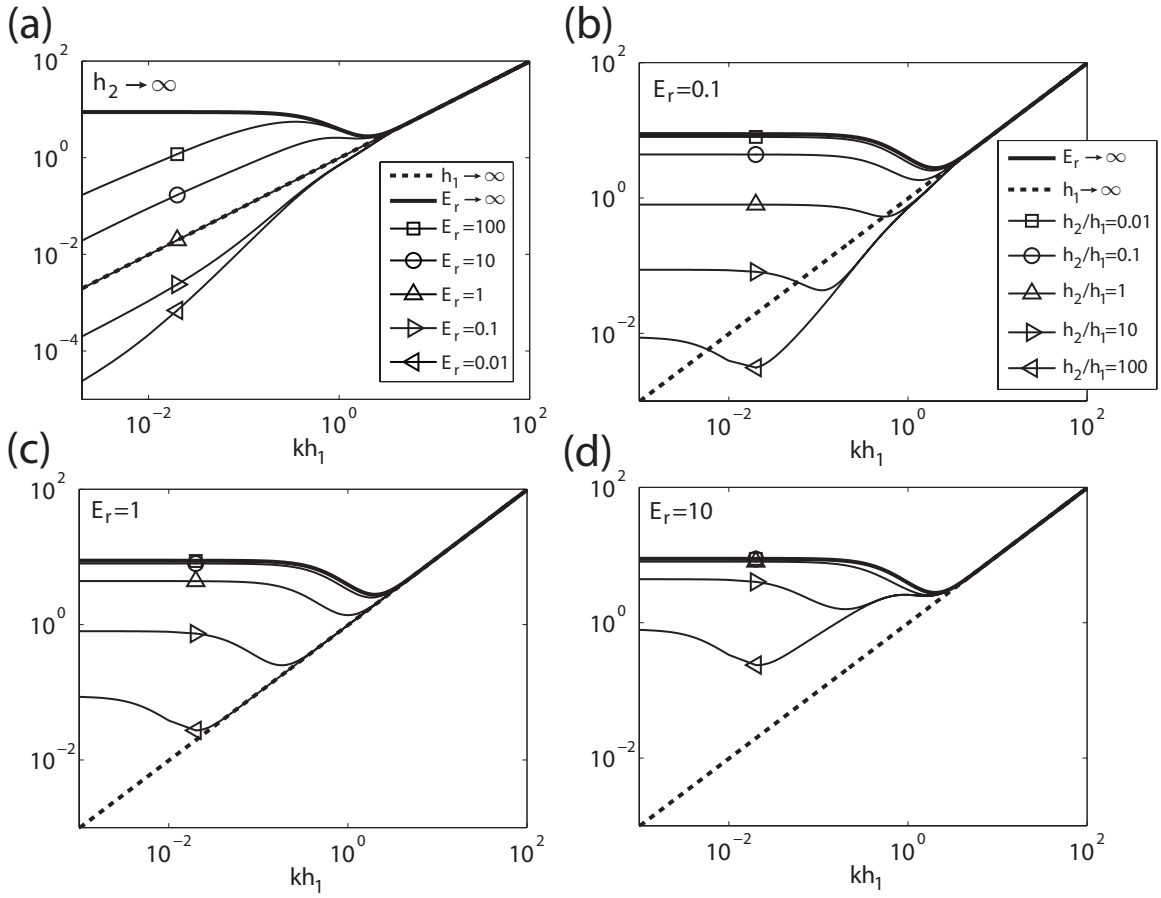

Figure 5.2: Spectral analysis of the solution for a two-layered substrate. The curves represent the Frobenius norm of the transfer matrix (see Eq. 2.72) of the solution: (a) for an infinitely thick bottom substrate ($h_2 \to \infty$), and different ratios of Young's moduli, E_r (see insert legend); (b) for $E_r = 0.1$ and different ratios of thicknesses h_2/h_1 (see insert legend); (c) for $E_r = 1$ and different ratios of thicknesses h_2/h_1 (see insert legend in (b)); (d) for $E_r = 10$ and different ratios of thicknesses h_2/h_1 (see insert legend in (b)). All the curves have been calculated for $\sigma = 0.48$.

As the wavenumber keeps decreasing, the norm of the transfer matrix for the two-layered substrate approaches Boussinesq's solution again, due to the transition to a regime in which the infinitely stiff substrate to which layer 2 is attached at $z = 0$ starts playing a role. For wavenumbers low enough, the apparent Young's modulus increases over E_1.

As of today, it is not clear whether cells sense the mechanical properties of the surrounding environment at the scale of the adhesions [162], or at a larger scale of the size of the cell [167]. The reported differences in apparent Young's modulus depending on the lengthscale of application of the traction stresses (for a two-layered substrate with $E_r < 1$) could be used to identify the lengthscale at which cells sense the mechanical surrounding

environment, taking as well advantage of the well documented increase in the spread area of the cell as the substrate Young's modulus increases [95, 162].

5.2 Solution of the elastostatic equation for a substrate with a shallow gradient of Young's modulus

We obtained the solution of the elastostatic equation for a substrate with a shallow spatial gradient of Young's modulus, a configuration of interest for the study of durotaxis, or cell motion guided by gradients of ECM stiffness. We consider a cell attached to the substrate free surface of a linearly elastic semi-infinite substrate. We adopt a Cartesian coordinate system with the x and y axes parallel to substrate free surface at undisturbed state, located at $z = 0$. The cell adheres and exerts stresses at the substrate free surface, inducing a deformation field which is measured through application of correlation techniques to images of fluorescent beads embedded in the substrate. Fig. 5.3 sketches this experimental configuration. We then solved the elastostatic equation

$$\frac{\partial \tau_{ik}}{\partial x_k} = 0, \tag{5.54}$$

where the components of the stress tensor τ_{ik} can be expressed as a function of the strain tensor u_{ik}, the Young's modulus of the substrate E and its Poisson's ratio σ as

$$\tau_{ik} = \frac{E}{2(1+\sigma)} \left(u_{ik} + \frac{\sigma}{1-2\sigma} u_{ll}\, \delta_{ik} \right). \tag{5.55}$$

Notice that the combination of Eqs. 5.54 and 5.55 leads to Eq. 5.1.

We formulated the solution to Eq. 2.17 in the framework of regular perturbation theory [168], with E as the perturbed quantity

$$E = E_0 \left(1 + \epsilon f(x)\right), \tag{5.56}$$

where E_0 is the leading order of E, ϵ is the perturbation parameter, and $f(x)$ is the perturbation function of E.

We thus decomposed the displacement field u_k into leading order, u_0, and perturbation, u_1, as

$$u_k = u_{0,k} + \epsilon\, u_{1,k} \tag{5.57}$$

which we substituted in Eqs. 5.54 and 5.55, together with the definition of the strain tensor as a function of the displacements:

$$u_{ik} = \frac{1}{2} \left(\frac{\partial u_i}{\partial x_k} + \frac{\partial u_k}{\partial x_i} \right). \tag{5.58}$$

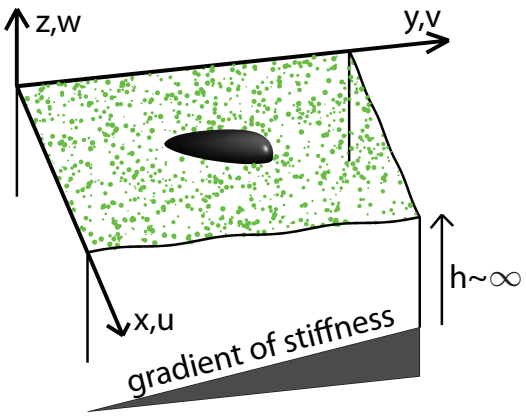

Figure 5.3: Sketch of the analytic assay of a substrate with a spatial gradient of Young's modulus for durotaxis.

We then decomposed the problem into a leading order and a first-order problem.

The leading order problem, expressed in vector notation, is thus

$$\frac{\nabla\left(\nabla\cdot\mathbf{u}_0\right)}{1-2\sigma}+\nabla^2\mathbf{u}_0=0, \tag{5.59}$$

with boundary conditions

$$\begin{aligned}\mathbf{u}_0(x,y,-\infty)&=0,\\ \mathbf{u}_0(x,y,0)&=\mathbf{u}^M(x,y),\end{aligned} \tag{5.60}$$

where $\mathbf{u}^M(x,y)$ are the measured displacements at the free surface of the substrate, $z=0$. The leading order problem is equivalent to solving the elastostatic equation for a substrate of uniform Young's modulus, E_0, and its solution can be obtained in terms of the Fourier series of the displacements (see Section 2.2) as

$$\begin{bmatrix}\widehat{\mathbf{u}}_{0,\alpha\beta}\\ d\widehat{\mathbf{u}}_{0,\alpha\beta}\end{bmatrix}(z)=P_{\alpha\beta}\,\exp(J_{\alpha\beta}z)P_{\alpha\beta}^{-1}\begin{bmatrix}\widehat{\mathbf{u}}^M_{\alpha\beta}\\ d\widehat{\mathbf{u}}^S_{\alpha\beta}\end{bmatrix}=Q_{\alpha\beta}\begin{bmatrix}\widehat{\mathbf{u}}^M_{\alpha\beta}\\ d\widehat{\mathbf{u}}^S_{\alpha\beta}\end{bmatrix}, \tag{5.61}$$

where $\widehat{\mathbf{u}}^M_{\alpha\beta}$ and $\widehat{d\mathbf{u}}^S_{\alpha\beta}$ are the Fourier coefficients of the measured displacements and of the z-derivative of the displacements at the free surface respectively. Obtaining $\widehat{d\mathbf{u}}^S_{\alpha\beta}$ as a function of $\widehat{\mathbf{u}}^M_{\alpha\beta}$ was already derived in Section 2.2 for the more general case of a substrate of finite thickness.

The ϵ-order or first-order problem is

$$\nabla^2\mathbf{u}_1+\frac{\nabla\left(\nabla\cdot\mathbf{u}_1\right)}{1-2\sigma}=-\frac{1+\sigma}{E_0}\nabla\left[f(x)\,\overline{\tau}_0\right]. \tag{5.62}$$

with boundary conditions

$$\begin{aligned} \mathbf{u}_1(x, y, -\infty) &= 0, \\ \mathbf{u}_1(x, y, 0) &= 0. \end{aligned} \tag{5.63}$$

Notice that the ϵ-order problem in Eq. 5.62 differs from the leading order problem in Eq. 5.59 only in the forcing term in its right hand side (RHS). The components of the leading order of the stress tensor, $\overline{\tau}_0$ (or $\tau_{0,ik}$ in Einstein's notation), are given by

$$\tau_{0,ik} = \frac{E_0}{2(1+\sigma)} \left(u_{0,ik} + \frac{\sigma}{1-2\sigma} u_{0,ll} \delta_{ik} \right). \tag{5.64}$$

We expressed the solution to Eq. 5.62 in terms of the Fourier series of the perturbation of the displacements

$$\mathbf{u}_1(x, y, z) = \sum_{\alpha=-\infty}^{\infty} \sum_{\beta=-\infty}^{\infty} \widehat{\mathbf{u}}_{1,\alpha\beta}(z) \, \exp(\mathrm{i}\alpha x) \, \exp(\mathrm{i}\beta x), \tag{5.65}$$

where α and β are the wavenumbers in the x and y directions, and $\widehat{\mathbf{u}}_{1,\alpha\beta}$ are the Fourier coefficients of the perturbation of the displacements. Introducing Eq. 5.65 into Eq. 5.62 we obtain the following first-order non-homogeneous ordinary differential equation

$$\frac{d}{dz} \begin{bmatrix} \widehat{u}_{1,\alpha\beta} \\ \widehat{v}_{1,\alpha\beta} \\ \widehat{w}_{1,\alpha\beta} \\ d\widehat{u}_{1,\alpha\beta}/dz \\ d\widehat{v}_{1,\alpha\beta}/dz \\ d\widehat{w}_{1,\alpha\beta}/dz \end{bmatrix} = \begin{bmatrix} \widehat{\mathbf{u}}_{1,\alpha\beta} \\ d\widehat{\mathbf{u}}_{1,\alpha\beta} \end{bmatrix} = A_{\alpha\beta} \begin{bmatrix} \widehat{\mathbf{u}}_{1,\alpha\beta} \\ d\widehat{\mathbf{u}}_{1,\alpha\beta} \end{bmatrix} + \mathbf{G}_{\alpha\beta}, \tag{5.66}$$

where matrix $A_{\alpha\beta}$ was already defined in Eq. 2.21 and $\mathbf{G}_{\alpha\beta}$ is given by

$$\mathbf{G}_{\alpha\beta} = \begin{bmatrix} 0 \\ 0 \\ 0 \\ -2\,\mathrm{i}\,(1+\sigma) \left(\alpha \widehat{F}_{xx,\alpha\beta} + \beta \widehat{F}_{xy,\alpha\beta} - \mathrm{i} d\widehat{F}_{xz,\alpha\beta}/dz \right) \\ -2\,\mathrm{i}\,(1+\sigma) \left(\alpha \widehat{F}_{yx,\alpha\beta} + \beta \widehat{F}_{yy,\alpha\beta} - \mathrm{i} d\widehat{F}_{yz,\alpha\beta}/dz \right) \\ \left[-\mathrm{i}\,(-1+2\sigma)(1+\sigma)/(-1+\sigma) \right] \left(\alpha \widehat{F}_{zx,\alpha\beta} + \beta \widehat{F}_{zy,\alpha\beta} - \mathrm{i} d\widehat{F}_{zz,\alpha\beta}/dz \right) \end{bmatrix}, \tag{5.67}$$

The different components of the tensor $\widehat{\overline{F}}_{\alpha\beta}$ are related to the forcing term in Eq. 5.62 (its RHS) as

$$\widehat{\overline{F}}_{\alpha\beta} = \frac{1}{E_0} \mathcal{F} \left[f(x) \, \overline{\tau}_0 \right], \tag{5.68}$$

where $\mathcal{F}$ stands for two-dimensional Fourier transform.

The solution to Eq. 5.62 is given by (see [169])

$$\begin{bmatrix} \widehat{\mathbf{u}}_{1,\alpha\beta} \\ d\widehat{\mathbf{u}}_{1,\alpha\beta} \end{bmatrix} = Q_{\alpha\beta} \int_0 Q_{\alpha\beta}^{-1}\, \mathbf{G}_{\alpha\beta}\, dz, \tag{5.69}$$

providing with the first-order of the displacements and their z-derivatives, which can be evaluated at $z = 0$ (substrate free surface) to obtain the exerted traction stresses.

The traction stresses can be decomposed in physical space as leading order and perturbation as

$$\tau_{ik} = \tau_{0,ik} + \epsilon\, \tau_{1,ik} = \tau_{0,ik} + \epsilon\, [\, f(x)\, \tau_{0,ik} + \tau^{\star}_{1,ik}\,], \tag{5.70}$$

where

$$\tau^{\star}_{1,ik} = \frac{E_0}{2(1+\sigma)} \left(u_{1,ik} + \frac{\sigma}{1-2\sigma}\, u_{1,ll}\, \delta_{ik} \right), \tag{5.71}$$

and the Fourier coefficients of the stress tensor in Eq. 5.70 are

$$\widehat{\tau}_{ik,\alpha\beta} = \widehat{\tau}_{0,ik,\alpha\beta} + \epsilon\, [E_0\, \widehat{F}_{ik,\alpha\beta} + \widehat{\tau}^{\star}_{1,ik,\alpha\beta}\,], \tag{5.72}$$

We can ease the computation of the perturbation of the displacements and their z-derivatives, $\widehat{\mathbf{u}}_{1,\alpha\beta}$ and $d\widehat{\mathbf{u}}_{1,\alpha\beta}$ respectively, by choosing the perturbation function as the sinusoidal function $f(x) = \sin(2\pi x/L_x)$, where L_x is the size in the x-direction of the box where we compute stresses. Eq. 5.68 then simplifies to

$$\widehat{\overline{F}}_{\alpha\beta} = \frac{\mathrm{i}}{2E_0} \left(\widehat{\overline{\tau}}_{0,\alpha+\Delta\alpha\,\beta} - \widehat{\overline{\tau}}_{0,\alpha-\Delta\alpha\,\beta} \right) \Delta\alpha\, \Delta\beta \tag{5.73}$$

where $\Delta\alpha = \Delta\beta = \frac{2\pi\Delta}{L_B}$, which in turn greatly simplifies the calculation of Eq. 5.69.

Finally, the inverse Fourier transform of the Fourier coefficients $\widehat{\tau}_{ik,\alpha\beta}$ (Eq. 5.72) at $z = 0$ yield the traction field on the substrate free surface (see Eq. 5.53).

5.2.1 Assay for the study of durotaxis

We present in this section a methodology for the calculation of the cell traction stresses in a substrate with a shallow linear gradient of Young's modulus (Fig. 5.4).

As explained in Section 5.2, the calculation of the traction stresses in a substrate with a shallow spatial gradient of substrate elasticity E is simplified if we assume the perturbation in E is sinusoidal (Eq. 5.73). We can make use of this feature if we substitute the displacement field exerted by a cell, enclosed in a box of size L_B (Fig. 5.4a), in the center

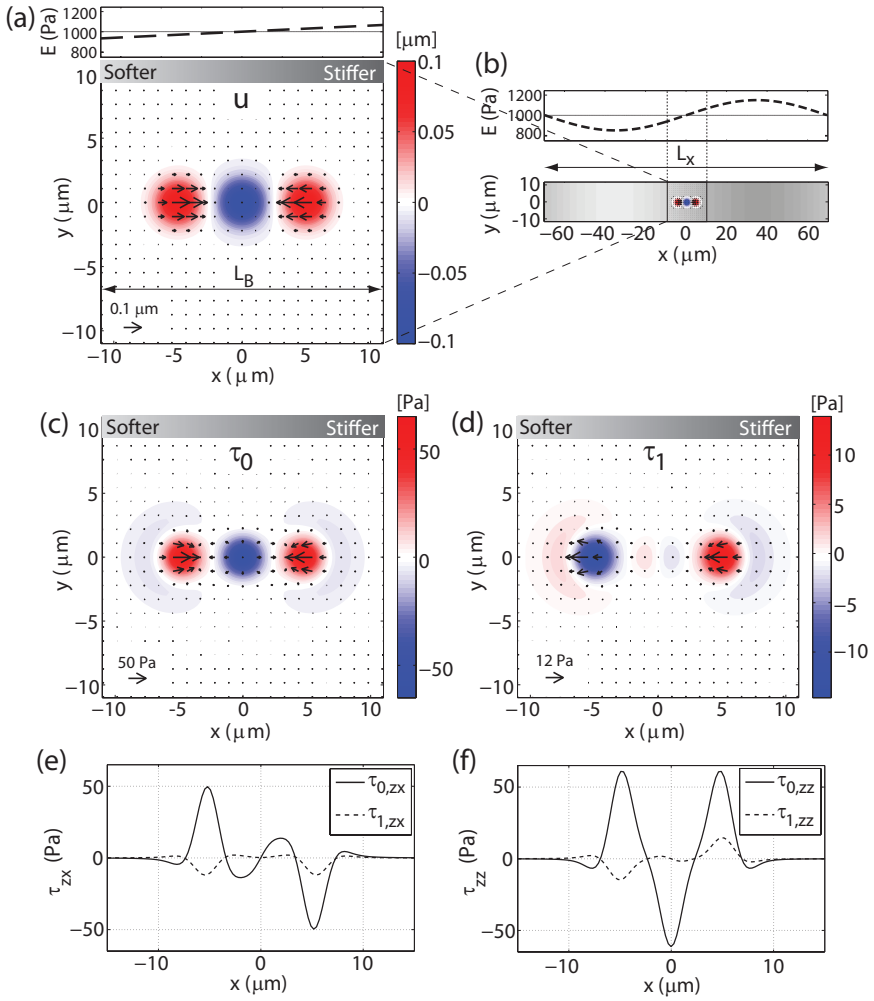

Figure 5.4: Assay for the study of durotaxis. (a) Three-dimensional displacement field, $\mathbf{u}(x, y)$, at the free surface of a substrate with a shallow linear gradient of Young's modulus, E, in the x-direction (leading order of E is $E_0 = 1000\,\mathrm{Pa}$) (see top panel). The synthetic displacement field used is representative of the traction displacements typically exerted by migrating amoeboid cells. The colormap indicates the magnitude of the vertical displacements and the arrows the magnitude and direction of the horizontal displacements. The size of the box enclosing the displacements is L_B. (b) The displacement field in panel (a) is substituted in the center of a larger rectangular box of size $L_x \times L_B$, presenting a shallow sinusoidal perturbation ($\epsilon = 0.15$) on E_0 in the x-direction (see top panel), which matches with the linear Young's modulus field in panel (a) in the region where the box of size L_B is located . (c) Leading order of the traction stresses, $\boldsymbol{\tau}_0(x, y)$, for the displacement field in (a). The colormap indicates the magnitude of the vertical stresses and the arrows the direction and magnitude of tangential stresses. (d) First-order perturbation of the traction stresses, $\boldsymbol{\tau}_1(x, y)$, for the displacement field in (a). The colormap indicates the magnitude of the vertical stresses and the arrows the direction and magnitude of tangential stresses. (e) Leading order (solid line) and first-order perturbation (dashed line) of the tangential stresses in the x-direction along the centerline, $\tau_{zx}(x, y = 0)$. (f) Leading order (solid line) and first-order perturbation (dashed line) of the vertical stresses (in the z-direction) along the centerline, $\tau_{zz}(x, y = 0)$. A Poisson's ratio of $\sigma = 0.49$ has been used for the calculations.

of a larger computational box, of size $L_x \times L_B$, with a shallow sinusoidal perturbation on the leading order of E, $E_0 = 1000\,\mathrm{Pa}$, in the x-direction (Fig. 5.4b), so that the gradient is nearly linear ($f(x) = \sin(2\pi x/L_x) \approx 2\pi x/L_x \sim x$) in the region where the smaller box (L_B) is located. We pad with zero displacements the rest of the field, which will not affect our calculation, provided that L_B is large enough for both displacements and stresses to decay to zero at the boundaries of the smaller box.

This methodology, together with the solution in Section 5.2, enables us to calculate both the leading-order of the traction stresses (Fig. 5.4c) and their first-order perturbation (Fig. 5.4d). Figs. 5.4e shows the leading order and the first-order perturbation of the tangential traction stresses, τ_{zx}, along the centerline of the cell ($y = 0$). Figs. 5.4f is a similar figure but for the vertical traction stresses, τ_{zz}. As expected, they show that in the region where $E > E_0$ ($x > 0$), the magnitude of the stresses required to deform the substrate is larger than in the region of $E < E_0$ ($x < 0$). We'd like to point out that the perturbation in the stresses, $\boldsymbol{\tau}_1$, is not simply proportional to the relative increase in Young's modulus with respect to E_0 , but there is an additional term ($\tau^{\star}_{1,ik}$ in Eq. 5.70) which accounts for the presence of the gradient in E, and which this method allows to calculate.

5.3 Discussion

In the last years there has been a notable increase of interest in the mechanical actions that cells implement in their surroundings, and how cell behavior is affected by the mechanical properties of the extracellular matrix or tissue and by the non-linearities and inhomogeneities in those [27, 144, 162, 170]. One of the key questions is how cells are able to sense the changes in mechanical environment. Numerous models have been proposed as possible cell-substrate transducer mechanisms [164, 171–174], most of them assuming that the deformation of protein complexes located at cell-substrate adhesions leads to certain chemical changes which in turn lead to cell response [163]. Despite all the advances in this direction, it is still not well established what are the mechanisms by which mechanosensing takes place. For instance, it is still unresolved whether cells implement mechanosensing at the scale of cell-substrate adhesions [162], at the scale of the size of the cell [167], or maybe a combination of both of them. The analytic assay presented in this chapter for the calculation of traction forces exerted by cells on top of a substrate composed of two layers could be used to answer that question.

A process clearly ruled by mechanosensing is durotaxis [165, 166]. There have been

recent modelling attempts trying to understand the nature of durotaxis [175]. However valuable these approaches may be, we need to increase our level of understanding of this process. A possible direction would include a better characterization of force organization during durotaxis, trying to identify front-back asymmetries in traction stresses or substrate displacements. The study of durotaxis could be used as a model problem of cell mechanosensing and mechanotransduction. In this respect, the solution of the elastostatic equation developed in this chapter for a substrate presenting a shallow gradient of substrate elasticity and the proposed analytical assay could serve very well this purpose, which we aim to pursue, possibly in combination with the rest of techniques developed in this dissertation.

Chapter 5, in part, is in preparation for submission for publication, "Advanced Fourier traction cytometry techniques for mechanotransduction studies," by B. Alonso-Latorre, J. C. del Álamo, R. Meili, R. A. Firtel, and J. C. Lasheras (2011). The thesis author is the primary investigator in this publication.

Chapter 6

Concluding Remarks and Recommendations

A brief summary of the main conclusions achieved in this dissertion is presented in this chapter, as well as the presentation of possible directions for future investigation. A detailed discussion can be found at the end of Chapters 2 to 5.

In this dissertation, we have analyzed in detail the spatio-temporal coordination between cell shape and traction forces exerted by migrating amoeboid cells, that is, between kinematics and dynamics of amoeboid cell migration. For that purpose, we have developed an improved analytical Fourier method for the calculation of the traction stresses exerted by cells which considers the finite thickness of the substrate, and allows to study long recordings of the migration of single cells.

Throughout all of our experiments we have observed a pattern of traction stresses consisting on the cell attaching at a reduced number of regions (typically two or three) and contracting the substrate inwards, consistent with the cytoskeleton being always subject to internal tension [176]. The developed methodology has allowed us to show that the strength of the traction forces exerted by cells follows a quasi-periodic temporal evolution, which is correlated with the changes in cell shape during the amoeboid motility cycle, consisting of pseudopod protrusion and creation of new attachments at the front of the cell, followed by the contraction of the cell body, leading to the detachment and retraction of the posterior part of the cell [1].

The temporal evolution of cell length, a surrogate indicator of the changes in cell shape, has been used to identify the different stages of the motility cycle: protrusion, con-

traction, retraction, and relaxation. This dissection of the motility cycle has allowed us to compute phase-average statistics, quantifying the main differences in the cell shape changes and generation of traction forces in *WT*, *mlcE*$^{-}$, and *mhcA*$^{-}$ strains. The combination of this approach together with a tailored implementation of PCA has allowed us to identify a reduced set of 5 canonical traction force patterns or components accounting for most of the mechanical work or strain energy that cells exert in the substrate during migration. The prevalent component is responsible for approximately 40% of the mechanical work exerted by both *WT* and contractility mutants, and its temporal modulation is responsible for the observed quasi-periodicity in traction forces and strain energy, and the correlation with cell length. This prevalent canonical component consists for *WT* cells in the attachment to the substrate at two well-defined regions at front and back, contracting the substrate inwards with a strength modulated in time. This dominant force pattern remains similar when MyoII contraction is impaired (in *mlcE*$^{-}$ cells), but it is modified when both actomyosin contractility and crosslinking are abrogated, in *mhcA*$^{-}$ cells), which distribute the traction forces around the cell periphery, suggesting that origin of contractility in the absence of MyoII function is cortical. A candidate motor protein to take over the function of MyoII is protein myosin I, reported to localize at the cell cortex [68, 177], and thus consistent with the results obtained.

We have also shown that the average speed of migration, V, of amoeboid cells, is determined by their ability to implement the motility cycle in a fast and coordinated way, according to a hyperbolic law $VT{=}\lambda$, where T is the period of the motility cycle, and λ is the average displacement per cycle of the cell, or step length. The step length λ is the same for *WT* and contractility mutants (*mlcE*$^{-}$ and *mhcA*$^{-}$ cells), which suggests that the implementation of the motility cycle is not substantially modified due to alterations in F-actin crosslinking or contractility. Understanding what determines the step length λ may as well answer what regulates the cyclic evolution of both cell shape and traction forces, for which F-actin polymerization is a very good candidate. In this direction, a very promising approach would be to alter F-actin polymerization through manipulation of the SCAR/WAVE complex [178–181], an upregulator of the Arp2/3 complex [182].

Our results show that the timing of the motility cycle, its period T, is partially controlled by actomyosin contractility (*mlcE*$^{-}$ and *mhcA*$^{-}$) and crosslinking (*mhcA*$^{-}$). Statistics of the duration of each phase of the cycle show that MyoII contractility is important for an efficient development of all the stages, and not only retraction. Actomyosin crosslinking has an impact in both pseudopod protrusion and uropod retraction, possibly through the

stabilization of the cell cytoskeletal structure along the side of the cell and its rear.

Analysis of the area fluxes exhibited by migrating cells shows that amoeboid locomotion results from the simultaneous combination of the continuous translocation of the cell body (accounting for $\approx 70\%$ of cell movement) and a superimposed periodic cycle of front protrusion and rear retraction (accounting for $\approx 30\%$ of cell movement). These two contributions are very possibly coupled, as indicated by the fact that migration speed due both to translocation and to the deformation of the cell are inversely proportional to the period of T, the same as the average velocity of migration, V. They are possibly driven by similar biochemical processes, regulated at different scales of both space and time. The deformation component presumably modulates cell shape and regulates other processes, such as the level of stress driving the continous translocation of the cell.

All the methods to calculate cell traction stresses exerted have typically assumed that vertical stresses exerted by cells are negligible. Recent evidence shows that vertical stresses are in many instances comparable to tangential stresses [96, 97, 183]. It is then of an important practical interest to quantify the influence that the assumption that vertical stresses are negligible has in the calculation of the cell traction stresses. Our estimations indicate that the tangential stresses calculated with the 2D method do not differ substantially from the 3D method ($\approx 10\%$), which means that studies of the cell traction stresses up to date are indeed meaningful, and that the 2D technique may provide with useful information even if vertical stresses are exerted. However, the presence of significant vertical stresses (typically consisting in the cell pushing down the substrate at its center and pulling it from the sides) indicates the need of a more refined interpretation of the mechanical interaction cell-substrate, which possibly involves signalling processes triggered through the deformation of the cell nucleus [105–107]. Both experimental and modelling efforts will be required to ascertain these questions.

We have also developed two analytic assays for the study of aspects related to cell mechanosensing. There is a certain degree of knowledge about how cells may sense the mechanical properties of the surrounding environment [164]. However, there are more questions than answers. Our assays developed can be used for instance to study the lengthscale at which cells measure the mechanical properties of the surrounding substrate: whether they do it at the scale of the cell-substrate adhesions [162] or at the scale of the whole cell [167]; or in the investigation of traction force organization in durotaxis. One of the benefits of the presented assays is their analytical character, which allows the combination of both

experimental and modelling approaches.

In the same line as the study of the 3D traction stresses exerted on a planar substrate, a natural evolution of the work in this dissertation would be to move from the study of cell migration over flat substrates to cell migration across 3D matrices [153, 184], in an effort to reflect the migration of tumor cells or fibroblasts across surrounding tissue and ECM. Although of a tremendous potential impact and importance, the experiments of cell migration across 3D matrices pose also a list of challenges that need to be addressed (or at least partially avoided), such as the mechanical characterization of a matrix which may be remodeled due to the degrading activity of enzymes segregated by cells [185], non-linear mechanical properties [186], or the breakage of the assumption of a continuous medium, since physiological relevant matrices are fibrous and usually present a relatively large void fraction [153, 184, 185].

Finally, and following the same spirit of trying to move towards more applied scenarios, another possible extension of this work would be to study collective cell migration. Collective cell migration is a very important mechanism in morphogenesis, tissue repair and cancer, and involves the regulation of cell-cell junctions, adding an additional layer of complexity to cell locomotion [187, 188]. Recent works have investigated traction force organization [99, 189] and have identified coherent motions during the migration of cell monolayers. These are just the first steps in understanding in detail the rules of collective cell migration, for which we still need to obtain detailed information about the coupling between the dynamics of cell-cell and cell-substrate interaction.

References

[1] Lauffenburger, D. A., and A. F. Horwitz, 1996. Cell migration: a physically integrated molecular process. *Cell* 84:359–69.

[2] Pollard, T. D., and G. G. Borisy, 2003. Cellular motility driven by assembly and disassembly of actin filaments. *Cell* 112:453–465.

[3] Ridley, A. J., M. A. Schwartz, K. Burridge, R. A. Firtel, M. H. Ginsberg, G. Borisy, J. T. Parsons, and A. R. Horwitz, 2003. Cell migration: integrating signals from front to back. *Science* 302:1704–9.

[4] Li, S., J. L. Guan, and S. Chien, 2005. Biochemistry and biomechanics of cell motility. *Annu. Rev. Biomed. Eng.* 7:105–150.

[5] Palsson, B. O., and S. N. Bhatia, 2004. Tissue Engineering. Pearson Prentice Hall, Upper Saddle River, N.J., first edition.

[6] Bray, D., 2001. Cell movements: from molecules to motility. Garland Pub., New York, second edition.

[7] Condeelis, J., and J. Segall, 2003. Intravital imaging of cell movement in tumours. *Nat. Rev. Cancer* 921–930.

[8] Springer, T. A., 1994. Traffic signals for lymphocyte recirculation and leukocyte emigration: the multistep paradigm. *Cell* 76:301–314.

[9] Luo, L. Q., 2000. Rho GTPases in neuronal morphogenesis. *Nat. Rev. Neurosci.* 1:173–180.

[10] Kumar, S., and V. Weaver, 2009. Mechanics, malignancy, and metastasis: The force journey of a tumor cell. *Cancer Metastasis Rev.* 28:113–127.

[11] Kraemer, R., 2000. Regulation of cell migration in atherosclerosis. *Curr. Atheroscler. Rep.* 2:445–52.

[12] Fauchereau, F., U. Herbrand, P. Chafey, A. Eberth, A. Koulakoff, M. C. Vinet, M. R. Ahmadian, J. Chelly, and P. Billuart, 2003. The RhoGAP activity of OPHN1, a new F-actin-binding protein, is negatively controlled by its amino-terminal domain. *Mol. Cell. Neurosci.* 23:574–586.

[13] Soll, D. R., 1999. Computer-assisted three-dimensional reconstruction and motion analysis of living, crawling cells. *Comput. Med. Imag. Grap.* 23:3–14.

[14] Stites, J., D. Wessels, A. Uhl, T. Egelhoff, D. Shutt, and D. R. Soll, 1998. Phosphorylation of the *Dictyostelium* myosin II heavy chain is necessary for maintaining cellular polarity and suppressing turning during chemotaxis. *Cell Motil. Cytoskel.* 39:31–51.

[15] Wessels, D., H. Vawter-Hugart, J. Murray, and D. R. Soll, 1994. Three-dimensional dynamics of pseudopod formation and the regulation of turning during the motility cycle of *Dictyostelium*. *Cell Motil. Cytoskel.* 27:1–12.

[16] Murray, J., H. Vawter-Hugart, E. Voss, and D. R. Soll, 1992. Three-dimensional motility cycle in leukocytes. *Cell Motil. Cytoskel.* 22:211–223.

[17] Shutt, D. C., K. J. Daniels, E. J. Carolan, A. C. Hill, and D. R. Soll, 2000. Changes in the motility, morphology, and F-actin architecture of human dendritic cells in an in vitro model of dendritic cell development. *Cell Motil. Cytoskel.* 46:200–221.

[18] Soll, D. R., D. Wessels, S. Kuhl, and D. F. Lusche, 2009. How a cell crawls and the role of cortical myosin II. *Eukaryot. Cell* 8:1381–1396.

[19] Wessels, D., J. Murray, and D. R. Soll, 1992. Behaviorof *Dictyosteliumamoebae*isregulated primarily by the temporal dynamic of the naturalcAMP wave. *Cell Motil. Cytoskel.* 23:145–156.

[20] Stepanovic, V., D. Wessels, K. Daniels, W. F. Loomis, and D. R. Soll, 2005. Intracellular role of adenylyl cyclase in regulation of lateral pseudopod formation during *Dictyostelium* chemotaxis. *Eukaryot. Cell* 4:775–786.

[21] Volk, A. P. D., C. K. Heise, J. L. Hougen, C. M. Artman, K. A. Volk, D. Wessels, D. R. Soll, W. M. Nauseef, F. S. Lamb, and J. G. Moreland, 2008. ClC-3 and IClswell

are required for normal neutrophil chemotaxis and shape change. *J. Biol. Chem.* 283:34315–34326.

[22] Keren, K., Z. Pincus, G. Allen, E. Barnhart, G. Marriott, A. Mogilner, and J. Theriot, 2008. Mechanism of shape determination in motile cells. *Nature* 453:475–U1.

[23] Machacek, M., and G. Danuser, 2006. Morphodynamic profiling of protrusion phenotypes. *Biophys. J.* 90:1439–1452.

[24] Killich, T., P. Plath, E. Hass, W. Xiang, H. Bultmann, L. Rensing, and M. Vicker, 1994. Cell-movement and shape are nonrandom and determined by intracellular, oscillatory rotating waves in *Dictyostelium* amoebae. *Biosystems* 33:75–87.

[25] Harris, A. K., P. Wild, and D. Stopak, 1980. Silicone rubber substrata: a new wrinkle in the study of cell locomotion. *Science* 208:177.

[26] du Roure, O., A. Saez, A. Buguin, R. H. Austin, P. Chavrier, P. Silberzan, and B. Ladoux, 2005. Force mapping in epithelial cell migration. *Proc. Natl. Acad. Sci. USA* 102:2390–2395.

[27] Balaban, N. Q., U. S. Schwarz, D. Riveline, P. Goichberg, G. Tzur, I. Sabanay, D. Mahalu, S. Safran, A. Bershadsky, L. Addadi, and B. Geiger, 2001. Force and focal adhesion assembly: a close relationship studied using elastic micropatterned substrates. *Nat. Cell Biol.* 3:466–472.

[28] Dembo, M., T. Oliver, A. Ishihara, and K. Jacobson, 1996. Imaging the traction stresses exerted by locomoting cells with the elastic substratum method. *Biophys. J.* 70:2008–22.

[29] Peterson, M. A., 1996. Theory of deformable substrates dor cell motility studies. *Biophys. J.* 71:657–669.

[30] Landau, L. D., E. M. Lifshitz, A. M. Kosevich, and L. P. Pitaevskii, 1986. Theory of Elasticity. Pergamon Press, Oxford, third edition.

[31] Schwarz, U. S., N. Q. Balaban, D. Riveline, A. Bershadsky, B. Geiger, and S. A. Safran, 2002. Calculation of forces at focal adhesions from elastic substrate data: the effect of localized force and the need for regularization. *Biophys. J.* 83:1380–94.

[32] Cesa, C. M., N. Kirchgessner, D. Mayer, U. S. Schwarz, B. Hoffmann, and R. Merkel, 2007. Micropatterned silicone elastomer substrates for high resolution analysis of cellular force patterns. *Rev. Sci. Instrum.* 78:1–10.

[33] Butler, J. P., I. M. Tolic-Norrelykke, B. Fabry, and J. J. Fredberg, 2002. Traction fields, moments, and strain energy that cells exert on their surroundings. *Am. J. Physiol. Cell Physiol.* 282:C595–605.

[34] Lombardi, M. L., D. A. Knecht, M. Dembo, and J. Lee, 2007. Traction force microscopy in *Dictyostelium* reveals distinct roles for myosin II motor and actin-crosslinking activity in polarized cell movement. *J. Cell. Sci.* 120:1624–34.

[35] del Alamo, J. C., R. Meili, B. Alonso-Latorre, J. Rodriguez-Rodriguez, A. Aliseda, R. A. Firtel, and J. C. Lasheras, 2007. Spatio-temporal analysis of eukaryotic cell motility by improved force cytometry. *Proc. Natl. Acad. Sci. USA* 104:13343–13348.

[36] Meili, R., B. Alonso-Latorre, J. C. del Alamo, R. A. Firtel, and J. C. Lasheras, 2010. Myosin II is essential for the spatiotemporal organization of traction forces during cell motility. *Mol. Biol. Cell* 21:405–417.

[37] Zigmond, S. H., and J. G. Hirsch, 1973. Leukocyte locomotion and chemotaxis: new methods for evaluation and demontstration of a cell-derived chemotactic factor. *J. Exp. Med.* 137:387–410.

[38] Miller, M. J., S. H. Wei, I. Parker, and M. D. Cahalan, 2002. Two-photon imaging of lymphocyte motility and antigen response in intact lymph node. *Science* 296:1869–1873.

[39] Varnum, B., and D. R. Soll, 1984. Effects of cAMP on single cell motility in *Dictyostelium*. *J. Cell Biol.* 99:1151–1155.

[40] Yumura, S., H. Mori, and Y. Fukui, 1984. Localization of actin and myosin for the study of ameboid movement in Dictyostelium using improved immunofluorescence. *J. Cell Biol.* 99:894–9.

[41] Segall, J. E., P. R. Fisher, and G. Gerisch, 1987. Selection of chemotaxis mutants for *Dictyostelium discoideum*. *J. Cell Biol.* 104:151–161.

[42] Soll, D. R., E. Voss, B. Varnum-Finney, and D. Wessels, 1988. "Dynamics morphology sytem": a method for quantitating chnages in shape, pseudopod formation, and motion in normal and mutant amoebae of *Dictyostelium discoideum*. *J. Cell. Biochem.* 37:177–192.

[43] Fisher, P. R., R. Merkl, and G. Gerisch, 1989. Quantitative analysis of cell motility and chemotaxis in *Dictyostelium discoideum* by using an image processing system and a novel chemotaxis chamber providing stationary chemical gradients. *J. Cell Biol.* 108:973–84.

[44] Charest, P. G., and R. A. Firtel, 2006. Feedback signaling controls leading-edge formation during chemotaxis. *Curr. Opin. Genet. Dev.* 16:339–47.

[45] Condeelis, J., A. Hall, A. Bresnick, V. Warren, R. Hock, H. Bennett, and S. Ogihara, 1988. Actin polymerization and pseudopod extension during amoeboid chemotaxis. *Cell Motil. Cytoskel.* 77–90.

[46] Fukui, Y., J. Murray, K. S. Riddelle, and D. R. Soll, 1991. Cell behavior and actomyosin organization in *Dictyostelium* during substrate exploration. *Cell Struct. Funct.* 16:289–301.

[47] Iwadate, Y., and S. Yumura, 2008. Actin-based propulsive forces and myosin-II-based contractile forces in migrating *Dictyostelium* cells. *J. Cell Sci.* 121:1314–1324.

[48] O'connor, T. P., and D. Bentley, 1993. Accumulation of actin in subsets of pioneer growth cone filopodia in response to neural and epithelial guidance cues in-situ. *J. Cell Biol.* 123:935–948.

[49] Fisher, G. W., P. A. Conrad, R. L. Debiasio, and D. L. Taylor, 1988. Centripetal transport of cytoplasm, actin, and the cell-surface in lamellipodia of fibroblasts. *Cell Motil. Cytoskel.* 11:235–247.

[50] Watanabe, N., and T. J. Mitchison, 2002. Single-molecule speckle analysis of Aactin filament turnover in lamellipodia. *Science* 295:1083–1086.

[51] Svitkina, T. M., and G. G. Borisy, 1999. Arp2/3 complex and actin depolymerizing factor cofilin in dendritic organization and treadmilling of actin filament array in lamellipodia. *J. Cell Biol.* 145:1009–1026.

[52] Machesky, L. M., and R. H. Insall, 1998. Scar1 and the related Wiskott-Aldrich syndrome protein, WASP, regulate the actin cytoskeleton through the Arp2/3 complex. *Curr. Biol.* 8:1347–56.

[53] Takenawa, T., and H. Miki, 2001. WASP and WAVE family proteins: key molecules for rapid rearrangement of cortical actin filaments and cell movement. *J. Cell Sci.* 114:1801–1809.

[54] Wear, M. A., D. A. Schafer, and J. A. Cooper, 2000. Actin dynamics: Assembly and disassembly of actin networks. *Curr. Biol.* R891–R895.

[55] Iwasa, J. H., and R. D. Mullins, 2007. Spatial and temporal relationships between actin-filament nucleation, capping, and disassembly. *Curr. Biol.* 395–406.

[56] Ruoslahti, E., and M. D. Pierschbacher, 1987. New perspectives in cell-adhesion: RGD and integrins. *Science* 238:491–497.

[57] Gumbiner, B. M., 1996. Cell adhesion: The molecular basis of tissue architecture and morphogenesis. *Cell* 84:345–357.

[58] Cornillon, S., L. Gebbie, M. Benghezal, P. Nair, S. Keller, B. Wehrle-Haller, S. J. Charette, F. Bruckert, F. Letourneur, and P. Cosson, 2006. An adhesion molecule in free-living Dictyostelium amoebae with integrin beta features. *EMBO Rep.* 7:617–621.

[59] Pasapera, A. M., I. C. Schneider, E. Rericha, D. D. Schlaepfer, and C. M. Waterman, 2010. Myosin II activity regulates vinculin recruitment to focal adhesions through FAK-mediated paxillin phosphorylation. *J. Cell Biol.* 188:877–890.

[60] Michael, K. E., D. W. Dumbauld, K. L. Burns, S. K. Hanks, and A. J. Garcia, 2009. Focal adhesion kinase modulates cell adhesion strengthening via integrin activation. *Mol. Biol. Cell* 20:2508–2519.

[61] Gebbie, L., M. Benghezal, S. Cornillon, R. Froquet, N. Cherix, M. Malbouyres, Y. Lefkir, C. Grangeasse, S. Fache, J. Dalous, F. Bruckert, F. Letourneur, and P. Cosson, 2004. Phg2, a kinase involved in adhesion and focal site modeling in Dictyostelium. *Mol. Biol. Cell* 15:3915–25.

[62] De, R., A. Zemel, and S. A. Safran, 2010. Theoretical concepts and models of cellular mechanosensing. *Methods Cell. Biol.* 98:143–75.

[63] Pramanik, M. K., M. Iijima, Y. Iwadate, and S. Yumura, 2009. PTEN is a mechanosensing signal transducer for myosin II localization in *Dictyostelium* cells. *Genes Cells* 14:821–834.

[64] Wei, W. C., H. H. Lin, M. R. Shen, and M. J. Tang, 2008. Mechanosensing machinery for cells under low substratum rigidity. *Am. J. Physiol. Cell Physiol.* 295:C1579–C1589.

[65] Delozanne, A., and J. A. Spudich, 1987. Disruption of the *Dyctyostelium* myosin heavy-chain gene by homologous recombination. *Science* 1086–1091.

[66] Chen, P., B. D. Ostrow, S. R. Tafuri, and R. L. Chisholm, 1994. Targeted disruption of the *Dictyostelium* RMLC gene produces cells defective in cytokinesis and development. *J. Cell Biol.* 127:1933–44.

[67] Chen, T. L., P. A. Kowalczyk, G. Ho, and R. L. Chisholm, 1995. Targeted disruption of the *Dictyostelium* myosin essential light chain gene produces cells defective in cytokinesis and morphogenesis. *J. Cell. Sci.* 108 (Pt 10):3207–18.

[68] de la Roche, M. A., and G. P. Cote, 2001. Regulation of *Dictyostelium* myosin I and II. *Biochim. Biophys. Acta* 1525:245–61.

[69] Bosgraaf, L., and P. J. van Haastert, 2006. The regulation of myosin II in *Dictyostelium*. *Eur. J. Cell Biol.* 85:969–79.

[70] Griffith, L. M., S. M. Downs, and J. A. Spudich, 1987. Myosin light chain kinase and myosin light chain phosphatase from *Dictysotelium*: effects of reversible phosphorylation on myosin structure and function. *J. Cell Biol.* 1309–1323.

[71] Pollenz, R. S., T. L. L. Chen, L. Trivinoslagos, and R. L. Chisholm, 1992. The *Dyctyostelium* essential light chain is required for myosin function. *Cell* 951–962.

[72] Liu, X., K. Ito, S. Morimoto, A. Hikkoshi-Iwane, T. Yanagida, and T. Q. P. Uyeda, 1998. Filament structure as an essential factor for regulation of *Dictyostelium* myosin by regulatory light chain phosphorylation. *Proc. Natl. Acad. Sci. USA* 14124–14129.

[73] Fukui, Y., and S. Yumura, 1986. Actomyosin dynamics in chemotactic amoeboid movement of *Dictyostelium*. *Cell Motil. Cytoskel.* 662–673.

[74] Laevsky, G., and D. A. Knecht, 2003. Cross-linking of actin filaments by myosin II is a major contributor to cortical integrity and cell motility in restrictive environments. *J. Cell. Sci.* 116:3761–70.

[75] Jay, P. Y., P. A. Pham, S. A. Wong, and E. L. Elson, 1995. A mechanical function of myosin II in cell motility. *J. Cell. Sci.* 108 (Pt 1):387–93.

[76] Huttenlocher, A., R. R. Sandborg, and A. F. Horwitz, 1995. Adhesion in cell-migration. *Curr. Opin. Cell Biol.* 697–706.

[77] Zaidel-Bar, R., M. Cohen, L. Addadi, and B. Geiger, 2004. Hierarchical assembly of cell-matrix adhesion complexes. *Biochem. Soc. T.* 416–420.

[78] Weber, I., E. Wallraff, R. Albrecht, and G. Gerisch, 1995. Motility and substratum adhesion of *Dictyostelium* wild-type and cytoskeletal mutant cells: a study by RICM/bright-field double-view image analysis. *J. Cell Sci.* 108 (Pt 4):1519–30.

[79] Uchida, K. S., T. Kitanishi-Yumura, and S. Yumura, 2003. Myosin II contributes to the posterior contraction and the anterior extension during the retraction phase in migrating *Dictyostelium* cells. *J. Cell Biol.* 116:51–60.

[80] Ladam, G., L. Vonna, and E. Sackmann, 2005. Protrusion force transmission of amoeboid cells crawling on soft biological tissue. *Act. Biomat.* 1:485–97.

[81] Smith, L. A., H. Aranda-Espinoza, J. B. Haun, M. Dembo, and D. A. Hammer, 2007. Neutrophil traction stresses are concentrated in the uropod during migration. *Biophys. J.* 92:L58–L60.

[82] Robinson, D. N., and J. A. Spudich, 2000. Dynacortin, a genetic link between equatorial contractility and global shape control discovered by library complementation of a *Dictyostelium discoideum* cytokinesis mutant. *J. Cell Biol.* 150:823–838.

[83] Dietrich, S., 2003. Introduction to percolation theory. Methods in Cell Biology. Elsevier, San Diego, first edition.

[84] Dimitriadis, E., F. Horkay, J. Maresca, B. Kachar, and R. Chadwick, 2002. Determination of elastic moduli of thin layers of soft material using the atomic force microscope. *Biophys. J.* 2798–2810.

[85] Li, Y., Z. Hu, and C. Li, 1993. New method for measuring Poisson's ratio in polymer gels. *J. Appl. Polymer Sci.* 1107–1111.

[86] Sluder, G., and D. E. Wolf, 2003. Video microscopy. Methods in Cell Biology. Elsevier, San Diego, first edition.

[87] Gibson, S. F., and F. Lanni, 1991. Experimental test of an analytical model of aberration in an oil-immersion objective lens used in 3-dimensional light-microscopy. *J. Opt. Soc. Am. A* 8:1601–1613.

[88] McNally, J. G., C. Preza, J. A. Conchello, and L. J. Thomas, 1994. Artifacts in computational optical-sectioning microscopy. *J. Opt. Soc. Am. A* 11:1056–1067.

[89] Canuto, C., M. Y. Hussaini, A. Quarteroni, and T. A. Zang, 2006. Spectral methods: Fundamentals in single domains. Scientific computation. Springer-Verlag, Berlin, first edition.

[90] Press, W. H., B. P. Flannery, S. A. Teukolsky, and W. T. Vetterling, 1992. Numerical recipes in FORTRAN: the art of scientific computing. Cambridge University Press, New York, second edition.

[91] Dembo, M., and Y. L. Wang, 1999. Stresses at the cell-to-substrate interface during locomotion of fibroblasts. *Biophys. J.* 76:2307–16.

[92] Rieu, J. P., C. Barentin, Y. Maeda, and Y. Sawada, 2005. Direct mechanical force measurements during the migration of *Dictyostelium* slugs using flexible substrata. *Biophys. J.* 89:3563–76.

[93] Barentin, C., Y. Sawada, and J. P. Rieu, 2006. An iterative method to calculate forces exerted by single cells and multicellular assemblies from the detection of deformations of flexible substrates. *Eur. Biophys. J.* 35:328–39.

[94] Solon, J., I. Levental, K. Sengupta, P. C. Georges, and P. A. Janmey, 2007. Fibroblast adaptation and stiffness matching to soft elastic substrates. *Biophys. J.* 93:4453–4461.

[95] Maloney, J. M., E. B. Walton, C. M. Bruce, and K. J. Van Vliet, 2008. Influence of finite thickness and stiffness on cellular adhesion-induced deformation of compliant substrata. *Physical Review E* 78.

[96] Hur, S. S., Y. H. Zhao, Y. S. Li, E. Botvinick, and S. Chien, 2009. Live cells exert 3-dimensional traction forces on their substrata. *Cell. Mol. Bioeng.* 2:425–436.

[97] Maskarinec, S., C. Franck, D. Tirrell, and G. Ravichandran, 2009. Quantifying cellular traction forces in three dimensions. *Proc. Natl. Acad. Sci. USA* 106:22108–22113.

[98] del Álamo, J. C., R. Meili, B. Alonso-Latorre, E. Bastounis, R. A. Firtel, and J. C. Lasheras, 2009. Three-dimensional forces exerted by migrating amoeboid cells. Oral presentation at the 52th Annual Meeting of the Biophysical Society, San Francisco, CA, USA.

[99] Trepat, X., M. R. Wasserman, T. E. Angelini, E. Millet, D. A. Weitz, J. P. Butler, and J. J. Fredberg, 2009. Physical forces during collective cell migration. *Nat. Phys.* 5:426–430.

[100] Khatau, S. B., C. M. Hale, P. J. Stewart-Hutchinson, M. S. Patel, C. L. Stewart, P. C. Searson, D. Hodzic, and D. Wirtz, 2009. A perinuclear actin cap regulates nuclear shape. *Proc. Natl. Acad. Sci. USA* 106:19017–19022.

[101] Mathur, A. B., G. A. Truskey, and W. M. Reichert, 2000. Atomic force and total internal reflection fluorescence microscopy for the study of force transmission in endothelial cells. *Biophys. J.* 78:1725–1735.

[102] Guilak, F., 1995. Compression-induced changes in the shape and volume of the chondrocyte nucleus. *J. Biomech.* 28:1529–1541.

[103] Caille, N., O. Thoumine, Y. Tardy, and J. J. Meister, 2002. Contribution of the nucleus to the mechanical properties of endothelial cells. *J. Biomech.* 35:177–187.

[104] Guilak, F., J. R. Tedrow, and R. Burgkart, 2000. Viscoelastic properties of the cell nucleus. *Biochem. Biophys. Res. Commun.* 269:781–786.

[105] Hale, C. M., A. L. Shrestha, S. B. Khatau, P. J. Stewart-Hutchinson, L. Hernandez, C. L. Stewart, D. Hodzic, and D. Wirtz, 2008. Dysfunctional connections between the nucleus and the actin and microtubule networks in laminopathic models. *Biophys. J.* 95:5462–5475.

[106] Lammerding, J., P. C. Schulze, T. Takahashi, S. Kozlov, T. Sullivan, R. D. Kamm, C. L. Stewart, and R. T. Lee, 2004. Lamin A/C deficiency causes defective nuclear mechanics and mechanotransduction. *J. Clin. Invest.* 113:370–378.

[107] Lammerding, J., J. Hsiao, P. C. Schulze, S. Kozlov, C. L. Stewart, and R. T. Lee, 2005. Abnormal nuclear shape and impaired mechanotransduction in emerin-deficient cells. *J. Cell Biol.* 170:781–791.

[108] Uchida, K. S., and S. Yumura, 2004. Dynamics of novel feet of *Dictyostelium* cells during migration. *J. Cell Sci.* 117:1443–55.

[109] Heid, P. J., J. Geiger, D. Wessels, E. Voss, and D. R. Soll, 2005. Computer-assisted analysis of filopod formation and the role of myosin II heavy chain phosphorylation in *Dictyostelium*. *J. Cell Sci.* 118:2225–2237. Cited References Count:59.

[110] Wessels, D., D. F. Lusche, S. Kuhl, P. Heid, and D. R. Soll, 2007. PTEN plays a role in the suppression of lateral pseudopod formation during *Dictyostelium* motility and chemotaxis. *J. Cell Sci.* 120:2517–2531.

[111] Wessels, D., D. R. Soll, D. Knecht, W. F. Loomis, A. Delozanne, and J. Spudich, 1988. Cell motility and chemotaxis in *Dictyostelium* amebae lacking myosin heavy-chain. *Dev. Biol.* 128:164–177. Cited References Count:25.

[112] Shelden, E., and D. A. Knecht, 1995. Mutants lacking myosin II cannot resist forces generated during multicellular morphogenesis. *J. Cell. Sci.* 108 (Pt 3):1105–15.

[113] Xu, X. S., A. Kuspa, D. Fuller, W. F. Loomis, and D. A. Knecht, 1996. Cell-cell adhesion prevents mutant cells lacking myosin II from penetrating aggregation streams of *Dictyostelium*. *Dev. Biol.* 218–226.

[114] Wessels, D., E. Voss, N. Von Bergen, R. Burns, J. Stites, and D. R. Soll, 1998. A computer-assisted system for reconstructing and interpreting the dynamic three-dimensional relationships of the outer surface, nucleus and pseudopods of crawling cells. *Cell Motil. Cytoskel.* 41:225–246.

[115] Abercrombie, M., J. E. Heaysman, and S. M. Pegrum, 1970. The locomotion of fibroblasts in culture. I. Movements of the leading edge. *Exp. Cell Res.* 59:393–8.

[116] Zhu, C., and R. Skalak, 1988. A continuum model of protrusion of pseudopod in leukocytes. *Biophys. J.* 1115–1137.

[117] Yoshida, K., and T. Soldati, 2006. Dissection of amoeboid movement into two mechanically distinct modes. *J. Cell Sci.* 119:3833–44.

[118] Fukui, Y., T. Q. Uyeda, C. Kitayama, and S. Inoué, 2000. How well can an amoeba climb? *Proc. Natl. Acad. Sci. U.S.A.* 97:10020–5.

[119] Langridge, P. D., and R. R. Kay, 2006. Blebbing of *Dictyostelium* cells in response to chemoattractant. *Exp. Cell Res.* 312:2009–2017.

[120] Grinstead, C. M., and J. L. Snell, 1997. Introduction to probability. American Mathematical Society, Providence, second edition.

[121] Xu, X. S., E. Lee, T. Chen, E. Kuczmarski, R. L. Chisholm, and D. A. Knecht, 2001. During multicellular migration, myosin ii serves a structural role independent of its motor function. *Dev. Biol.* 232:255–64.

[122] Effler, J. C., Y. S. Kee, J. M. Berk, M. N. Tran, P. A. Iglesias, and D. N. Robinson, 2006. Mitosis-specific mechanosensing and contractile-protein redistribution control cell shape. *Curr. Biol.* 1962–1967.

[123] Niewöhner, J., I. Weber, M. Maniak, A. Müller-Taubenberger, and G. Gerisch, 1997. Talin-null cells of *Dictyostelium* are strongly defective in adhesion to particle and substrate surfaces and slightly impaired in cytokinesis. *J. Cell Biol.* 138:349–61.

[124] Tolic-Norrelykke, I. M., J. P. Butler, J. X. Chen, and N. Wang, 2002. Spatial and temporal traction response in human airway smooth muscle cells. *Am. J. Physiol. Cell Physiol.* C1254–C1266.

[125] Zhu, C., R. Skalak, and G. W. Schmidschonbein, 1989. One-dimensional steady continuum model of retraction of pseudopod in leukocytes. *J. Biomech. Eng.* 111:69–77.

[126] Evans, E., 1993. New physical concepts for cell amoeboid motion. *Biophys. J.* 1306–1322.

[127] Tsujioka, M., K. Yoshida, and K. Inouye, 2004. Talin B is required for force transmission in morphogenesis of *Dictyostelium*. *EMBO J.* 23:2216.

[128] Decave, E., D. Garrivier, Y. Brechet, B. Fourcade, and F. Bruckert, 2002. Shear flow-induced detachment kinetics of *Dictyostelium discoideum* cells from solid substrate. *Biophys. J.* 82:2383–2395.

[129] Bruckert, F., E. Decave, D. Garrivier, P. Cosson, Y. Brechet, B. Fourcade, and M. Satre, 2002. *Dictyostelium discoideum* adhesion and motility under shear flow: experimental and theoretical approaches. *J. Muscle Res. Cell M.* 23:651–658.

[130] Devreotes, P. N., and S. H. Zigmond, 1988. Chemotaxis in eukaryotic cells: a focus on leukocytes and *Dictyostelium*. *Annu. Rev. Cell Biol.* 4:649–86.

[131] Ren, Y. X., J. C. Effler, M. Norstrom, T. Z. Luo, R. A. Firtel, P. A. Iglesias, R. S. Rock, and D. N. Robinson, 2009. Mechanosensing through Cooperative Interactions between Myosin II and the Actin Crosslinker Cortexillin I. *Curr. Biol.* 1421–1428.

[132] Pasternak, C., J. A. Spudich, and E. L. Elson, 1989. Capping of surface receptors and concomitant cortical tension are generated by conventional myosin. *Nature* 341:549–51.

[133] Witke, W., M. Schleicher, and A. A. Noegel, 1992. Redundancy in the microfilament system: abnormal development of *Dictyostelium* cells lacking two F-actin cross-linking proteins. *Cell* 53–62.

[134] Faix, J., M. Steinmetz, H. Boves, R. A. Kammerer, F. Lottspeich, U. Mintert, J. Murphy, A. Stock, U. Aebi, and G. Gerisch, 1996. Cortexillins, major determinants of cell shape and size, are actin-bundling proteins with a parallel coiled-coil tail. *Cell* 631–642.

[135] Reichl, E. M., Y. X. Ren, M. K. Morphew, M. Delannoy, J. C. Effler, K. D. Girard, S. Divi, P. A. Iglesias, S. C. Kuo, and D. N. Robinson, 2008. Interactions between myosin and actin crosslinkers control cytokinesis contractility dynamics and mechanics. *Curr. Biol.* 471–480.

[136] Charras, G. T., C. K. Hu, M. Coughlin, and T. J. Mitchison, 2006. Reassembly of contractile actin cortex in cell blebs. *J. Cell Biol.* 175:477–90.

[137] Charras, G. T., 2008. A short history of blebbing. *J. Microsc.-Oxford* 466–478.

[138] Jacobelli, J., F. C. Bennett, P. Pandurangi, A. J. Tooley, and M. F. Krummel, 2009. Myosin-IIA and ICAM-1 Regulate the interchange between two distinct modes of T cell migration. *J. Immunol.* 2041–2050.

[139] Shelden, E., and D. A. Knecht, 1996. *Dictyostelium* cell shape generation requires myosin II. *Cell Motil. Cytoskel.* 35:59–67.

[140] Wessels, D., and D. R. Soll, 1990. Myosin-II heavy-chain null mutant of *Dictyostelium* exhibits defective intracellular particle movement. *J. Cell Biol.* 111:1137–1148.

[141] Feneberg, W., M. Westphal, and E. Sackmann, 2001. *Dictyostelium* cells' cytoplasm as an active viscoplastic body. *Eur. Biophys. J.* 30:284–94.

[142] Girard, K. D., S. C. Kuo, and D. N. Robinson, 2006. *Dictyostelium* myosin II mechanochemistry promotes active behavior of the cortex on long time scales. *Proc. Natl. Acad. Sci. USA* 103:2103–8.

[143] Gardel, M. L., B. Sabass, L. Ji, G. Danuser, U. S. Schwarz, and C. M. Waterman, 2008. Traction stress in focal adhesions correlates biphasically with actin retrograde flow speed. *J. Cell Biol.* 183:999–1005.

[144] Sheetz, M. P., D. P. Felsenfeld, and C. G. Galbraith, 1998. Cell migration: Regulation of force on extracellular-matrix-integrin complexes. *Trends Cell Biol.* 8:51–54.

[145] Chen, C. S., J. L. Alonso, E. Ostuni, G. M. Whitesides, and D. E. Ingber, 2003. Cell shape provides global control of focal adhesion assembly. *Biochem. Bioph. Res. Co.* 307:355–361.

[146] Wang, N., and D. E. Ingber, 1994. Control of cytoskeletal mechanics by extracellular-matrix, cell-shape, and mechanical tension. *Biophys. J.* 66:2181–2189.

[147] Rubinstein, B., K. Jacobson, and A. Mogilner, 2005. Multiscale two-dimensional modeling of a motile simple-shaped cell. *Multiscale Model. Sim.* 3:413–439.

[148] Satulovsky, J., R. Lui, and Y. L. Wang, 2008. Exploring the control circuit of cell migration by mathematical modeling. *Biophys. J.* 94:3671–3683.

[149] Buenemann, M., H. Levine, W. J. Rappel, and L. M. Sander, 2010. The role of cell contraction and adhesion in *Dictyostelium* motility. *Biophys. J.* 99:50–58.

[150] Mogilner, A., and B. Rubinstein, 2010. Actin disassembly 'clock' and membrane tension determine cell shape and turning: a mathematical model. *J. Phys.-Condens. Mat.* 22.

[151] Friedl, P., S. Borgmann, and E. Brocker, 2001. Amoeboid leukocyte crawling through extracellular matrix: lessons from the Dictyostelium paradigm of cell movement. *J. Leukoc. Biol.* 70:491–509.

[152] Niggemann, B., T. L. Drell, J. Joseph, C. Weidt, K. Lang, K. S. Zaenker, and F. Entschladen, 2004. Tumor cell locomotion: differential dynamics of spontaneous and induced migration in a 3D collagen matrix. *Exp. Cell Res.* 298:178–187.

[153] Zaman, M. H., L. M. Trapani, A. Siemeski, D. MacKellar, H. Y. Gong, R. D. Kamm, A. Wells, D. A. Lauffenburger, and P. Matsudaira, 2006. Migration of tumor cells in 3D matrices is governed by matrix stiffness along with cell-matrix adhesion and proteolysis. *Proc. Natl. Acad. Sci. USA* 103:10889–10894.

[154] Bloom, R. J., J. P. George, A. Celedon, S. X. Sun, and D. Wirtz, 2008. Mapping local matrix remodeling induced by a migrating tumor cell using three-dimensional multiple-particle tracking. *Biophys. J.* 95:4077–4088.

[155] Laukaitis, C. M., D. J. Webb, K. Donais, and A. F. Horwitz, 2001. Differential dynamics of alpha 5 integrin, paxillin, and alpha-actinin during formation and disassembly of adhesions in migrating cells. *J. Cell Biol.* 153:1427–1440.

[156] Levi, S., M. V. Polyakov, and T. T. Egelhoff, 2002. Myosin II dynamics in *Dictyostelium*: Determinants for filament assembly and translocation to the cell cortex during chemoattractant responses. *Cell Motil. Cytoskel.* 53:177–188.

[157] Bryce, N. S., E. S. Clark, J. L. Leysath, J. D. Currie, D. J. Webb, and A. M. Weaver, 2005. Cortactin promotes cell motility by enhancing lamellipodial persistence. *Curr. Biol.* 15:1276–1285.

[158] Estecha, A., L. Sanchez-Martin, A. Puig-Kroger, R. A. Bartolome, J. Teixido, R. Samaniego, and P. Sanchez-Mateos, 2009. Moesin orchestrates cortical polarity of melanoma tumour cells to initiate 3D invasion. *J. Cell Sci.* 122:3492–3501.

[159] Berkooz, G., P. Holmes, and J. Lumley, 1993. The proper orthogonal decomposition in the analysis of turbulent flows. *Ann. Rev. Fluid Mech.* 25:539–575.

[160] Holmes, P., J. L. Lumley, and G. Berkooz, 1996. Turbulence, coherent structures, dynamical systems and symmetry. Cambridge monographs on mechanics. Cambrige University Press, Cambridge, first edition.

[161] Ferreras, I., A. Pasquali, R. R. de Carvalho, I. G. de la Rosa, and O. Lahav, 2006. A principal component analysis approach to the star formation history of elliptical galaxies in compact groups. *Mon. Not. R. Astron. Soc.* 370:828–836.

[162] Engler, A. J., S. Sen, H. L. Sweeney, and D. E. Discher, 2006. Matrix elasticity directs stem cell lineage specification. *Cell* 126:677–689.

[163] Vogel, V., 2006. Mechanotransduction involving multimodular proteins: converting force into biochemical signals. *Annu. Rev. Biophys. Biomol. Struct.* 35:459–88.

[164] Vogel, V., and M. Sheetz, 2006. Local force and geometry sensing regulate cell functions. *Nat. Rev. Mol. Cell Biol.* 7:265–275.

[165] Lo, C. M., H. B. Wang, M. Dembo, and Y. L. Wang, 2000. Cell movement is guided by the rigidity of the substrate. *Biophys. J.* 79:144–52.

[166] Wong, J. Y., A. Velasco, P. Rajagopalan, and Q. Pham, 2003. Directed movement of vascular smooth muscle cells on gradient-compliant hydrogels. *Langmuir* 1908–1913.

[167] Schwarz, U., 2007. Soft matters in cell adhesion: rigidity sensing on soft elastic substrates. *Soft Matter* 263–266.

[168] Van Dyke, M., 1975. Perturbation methods in fluid mechanics. The Parabolic Press, Standford, first edition.

[169] Weintraub, S. H., 2008. Jordan canonical form: application to differential equations. Synthesis lecutres on mathematics and statistics. Morgan & Claypool, first edition.

[170] Winer, J. P., S. Oake, and P. A. Janmey, 2009. Non-Linear elasticity of extracellular matrices enables contractile cells to communicate local position and orientation. *Plos One* 4.

[171] Janmey, P. A., and D. A. Weitz, 2004. Dealing with mechanics: mechanisms of force transduction in cells. *Trends Biochem. Sci.* 29:364–370.

[172] Nicolas, A., B. Geiger, and S. A. Safran, 2004. Cell mechanosensitivity controls the anisotropy of focal adhesions. *Proc. Natl. Acad. Sci. USA* 101:12520–12525.

[173] Moreo, P., J. M. Garcia-Aznar, and M. Doblare, 2008. Modeling mechanosensing and its effect on the migration and proliferation of adherent cells. *Acta Biomater.* 4:613–621.

[174] Schwarz, U. S., T. Erdmann, and I. B. Bischofs, 2006. Focal adhesions as mechanosensors: The two-spring model. *Biosystems* 83:225–232.

[175] Lazopoulos, K. A., and D. Stamenovic, 2008. Durotaxis as an elastic stability phenomenon. *J. Biomech.* 41:1289–1294.

[176] Kumar, S., I. Z. Maxwell, A. Heisterkamp, T. R. Polte, T. P. Lele, M. Salanga, E. Mazur, and D. E. Ingber, 2006. Viscoelastic retraction of single living stress fibers and its impact on cell shape, cytoskeletal organization, and extracellular matrix mechanics. *Biophys. J.* 90:3762–3773.

[177] Ostap, E. M., P. Maupin, S. K. Doberstein, I. C. Baines, E. D. Korn, and T. D. Pollard, 2003. Dynamic localization of myosin-I to endocytic structures in *Acanthamoeba*. *Cell Motil. Cytoskel.* 29–40.

[178] Blagg, S. L., and R. H. Insall, 2004. Control of SCAR activity in Dictyostelium discoideum. *Biochem. Soc. Trans.* 32:1113–4.

[179] Ibarra, N., A. Pollitt, and R. H. Insall, 2005. Regulation of actin assembly by SCAR/WAVE proteins. *Biochem. Soc. Trans.* 33:1243–6.

[180] Ibarra, N., S. L. Blagg, F. Vazquez, and R. H. Insall, 2006. Nap1 regulates *Dictyostelium* cell motility and adhesion through SCAR-dependent and -independent pathways. *Curr. Biol.* 16:717–22.

[181] Blagg, S. L., M. Stewart, C. Sambles, and R. H. Insall, 2003. PIR121 regulates pseudopod dynamics and SCAR activity in *Dictyostelium*. *Curr. Biol.* 13:1480–7.

[182] Bastounis, E., B. Alonso-Latorre, R. Meili, J. C. del Álamo, R. A. Firtel, and J. C. Lasheras, 2009. Scar/Wave as a regulator of cell shape and traction forces during amoeboid migration. Poster presentation at the 49th Annual Meeting of the American Society of Cell Biology, San Diego, CA, USA.

[183] del Álamo, J. C., R. Meili, B. Alonso-Latorre, B. Álvarez, R. A. Firtel, and J. C. Lasheras, 2011. Three-dimensional traction cytometry in amoeboid cells. In Preparation.

[184] Wolf, K., I. Mazo, H. Leung, K. Engelke, U. H. von Andrian, E. I. Deryugina, A. Y. Strongin, E. B. Brocker, and P. Friedl, 2003. Compensation mechanism in tumor cell migration: mesenchymal-amoeboid transition after blocking of pericellular proteolysis. *J. Cell Biol.* 160:267–277.

[185] Wolf, K., Y. I. Wu, Y. Liu, J. Geiger, E. Tam, C. Overall, M. S. Stack, and P. Friedl, 2007. Multi-step pericellular proteolysis controls the transition from individual to collective cancer cell invasion. *Nat. Cell Biol.* 9:893–U39.

[186] Storm, C., J. J. Pastore, F. C. MacKintosh, T. C. Lubensky, and P. A. Janmey, 2005. Nonlinear elasticity in biological gels. *Nature* 191–194.

[187] Friedl, P., Y. Hegerfeldt, and M. Tilisch, 2004. Collective cell migration in morphogenesis and cancer. *Int. J. Dev. Biol.* 441–449.

[188] Friedl, P., and D. Gilmour, 2009. Collective cell migration in morphogenesis, regeneration and cancer. *Nat. Rev. Mol. Cell Biol.* 445–457.

[189] Petitjean, L., M. Reffay, E. Grasland-Mongrain, M. Poujade, B. Ladoux, A. Buguin, and P. Silberzan, 2010. Velocity fields in a collectively migrating epithelium. *Biophys. J.* 98:1790–1800.